Towards an Improved Understanding of Strength and Damage in Cold Compacted Powders

A Thesis

Submitted to the Faculty

of

Drexel University

by

Sean Garner

in partial fulfillment of

the requirements for the degree

of

Doctor of Philosophy

June 2016

Dedications

I would like to dedicate this thesis to my parents, sister, and to my niece, who have supported me and encouraged me to shoot for the stars and achieve success.

Acknowledgements

I would like to express my deepest appreciation and gratitude to my advisor, Dr. Antonios Zavaliangos. His support during my PhD studies and research has allowed me to achieve a level of success I never thought possible. His excellent supervision, patience, and immense knowledge allowed me to grow not only as a researcher, but also as an individual. His valuable advice and thoughtful criticisms throughout my PhD studies has encouraged me to always take pride in my work and to believe in my abilities. I could not have imagined a better advisor, friend, and colleague.

I would like to thank my committee members, Dr. Steven May, Dr. Richard Knight, Dr. Wei-Heng Shih, and Dr. John Strong for their excellent supervision and guidance during my PhD studies. I would also like to express my appreciation to Yenneeka West, Keiko Nakazawa, Sarit Kunz, and Dorilona Rose for the assistance provided to me during my days in the Materials Science and Engineering Department. I am grateful to my fellow present and past group members, Dr. Chrysovalantis Tsigginos, Jovana Radojevic, Henrietta Tsosie, Dr. Jerry Klinzing, Elaine Ruiz, and Matthew West for providing valuable discussions and lasting friendships. Special thanks to Andrew Marx, Matthew Hartshorne, Dr. Darrin Tallman, and Dr. Kristy Jost for assisting me in many different ways during my stay at Drexel.

I would like to thank all of the faculty, staff, and graduate students for making my studies at Drexel University a remarkable and unforgettable experience. My warm thanks are due to Dr. John Strong, who has helped in providing me the potential for a wonderful future.

Finally, I would like to thank the Department of Education for the GAANN fellowship and AbbVie, Incorporated for financial support of this work.

Table of Contents

List of Tables

List of Figures

List of Symbols

Roman characters

a	Contact area
a_c	Crack length
C	Dimensionless separation deformation
D	Diameter
E_i	Particle elastic modulus
E^*	Equivalent elastic modulus
f_{0c}	Cohesive contact force at zero deformation
f_{max}	Maximum force at end of loading
f_{min}	Minimum force corresponding to pull-off force
f_n	Normal force
f_t	Tangential force
F	Interaction parameter
g	Gravitational acceleration
G	Energy release rate
G_{IC}	Mode I plane strain critical energy release rate
H	Material hardness
I	Moment of inertia
k	Stiffness
$\hat{k}_2$	Asymptotic stiffness
k_c	Cohesive stiffness
k_i	Contact spring stiffness, i = 1, 2, 3, 4
k_n	Normal contact stiffness
k_t	Tangential contact stiffness
K	Stress intensity factor
K_{IC}	Mode I plane strain fracture toughness
m	Work hardening exponent
m_i	Particle mass
m^*	Equivalent mass
M	Torque
r	Distance between particle-particle centers
R^*	Reduced particle radius
R_i	Particle radius
RD	Relative density
RD_0	Initial relative density
p	Hydrostatic pressure
p_0	Constant pressure distribution at the end of loading
P_f	Failure force
Δt_c	Critical time step
U	Strain energy
q	Effective von Mises stress
v_i	Particle velocity

W	Work of adhesion
Z	Coordination number

Greek characters

α	Constraint factor
β	Unloading stiffness ratio
γ	Viscous damping coefficient/or surface energy
γ_B	Bulk viscous damping coefficient
γ_s	Surface energy
δ	Contact deformation
δ_b	Full contact separation deformation
δ_0	Plastic contact deformation
δ_{max}	Maximum contact deformation at the end of loading
δ_{min}	Minimum contact deformation at maximum tensile strength
δ_n	Normal contact deformation
δ_t	Tangential contact deformation
δ^*	Limiting contact deformation
ε	Strain
η	triaxiality
θ	Dimensionless critical deformation limit
λ	Cohesive parameter
μ	Coefficient of friction
μ_r	Coefficient of rolling friction
ρ	Density of solid
σ	Stress
σ_A	Axial compressive strength
σ_R	Residual wall stress
σ_T	Tensile strength
σ_y	Yield strength
ν_i	Poisson's ratio of particle
φ	Local non-viscous damping coefficient
χ	Mesarovic and Johnson cohesive parameter
ω	Rotational velocity

Abstract

Towards an Improved Understanding of Strength and Damage in Cold Compacted Powders

Sean Garner

The compaction of fine powders offers an attractive means of creating engineered materials; however, there are often difficulties associated with producing compacts with acceptable properties. For example, failures including lamination or capping may occur during compaction and post-compaction processes if a certain level of mechanical strength is not met. Often times, a clear understanding of the cause of the issues leading to inadequate strength is lacking, thus making it difficult to mitigate the potential for failures. There is a strong interest in the availability of tools capable of providing a deeper understanding of the mechanisms responsible for the creation of compacts with adequate strength, as well as tools that can address the criticality of potential defects, and the effect these defects have on final compact properties.

The current work focuses on the following: investigating and analyzing crack formation, the development of strength in the powder compaction process, and the generation of relevant predictive models *via* computational modeling that will allow for process optimization. In an effort to identify the origin and the evolution of damage during the compaction/ejection cycle of powder compacts, an experimental study that compares compacts in straight and tapered dies was performed. Analysis of the presence and growth of microcracks was carried out using x-ray tomography and environmental scanning electron microscopy. The results show the presence of internal microcracks at high relative densities, and microcracks on the surface of the compacts. Parts compacted in tapered dies exhibited microcracks with smaller crack tip

openings and had a higher axial strength than those made in a straight die. These experimental observations, together with the ideas of damage generation under compressive stresses, as well as finite element analysis of the stress field in the compact as it exits from the die, confirmed the hypothesis that a two-step mechanism was responsible for damage generation in powder compacts. First, microcracking occurs during unloading within the die at high pressures and subsequently surface cracks grow under the localized stresses as the compact emerges from the die.

To further elucidate the behavior of powders in the powder compaction process and the effects that the discrete nature of damage had on strength, this work considered the discrete element method (DEM). For powders compacted to high density, it is crucial that the force-displacement behavior of contacting particles is adequately captured in order to make proper predictions related to damage and strength in compacted components. A new adhesive, elastoplastic contact model, which describes the force-displacement behavior of contacting particles compacted to high density, was introduced and implemented in the DEM. A methodology was developed for the calibration of the model parameters of the proposed model from macroscopic experimental results. This was achieved by the use of statistical design-of-experiments (DOE) and parameter optimization techniques.

The proposed DEM contact model was used to assess the ability of the DEM to predict damage and the effect that damage has on strength. A validation study was conducted to assess the ability of the proposed model to adequately predict behavior of powders compacted to high density. DEM simulations of powder compacted in straight and tapered dies were performed. The validation study performed showed excellent agreement with experimental finding for the unloading and ejection of straight and tapered die compacts.

Chapter 1: Introduction and Background

The compaction of powder materials is of critical importance to a wide range of industrial applications. Examples of where the compaction process proves to be instrumental are in the powder metallurgy [1] and ceramics industries [2, 3] where powders are typically compacted to high relative densities before being sintered to produce high strength engineering components where relative density RD is defined as the ratio of the apparent or envelope density of a sample to the theoretical density of the material. Other industries include the food [4] and pharmaceutical [5, 6] industries where powders are pressed to high densities without sintering to create green[1] compacts as final products. While the compaction of powders offers an attractive means of producing engineered materials, there are often difficulties associated with achieving compacts with acceptable properties. The degree to which the properties of compressed powders are affected is dictated by the properties making up the powder assembly and the physics of interactions between particle surfaces taking place before, during, and after compaction. For example, frictional effects between the powder and powder tooling can produce inhomogeneous distributions of density and residual stress. Consequently, these inhomogeneities in density may result in regions of low density that are associated with lower mechanical strength than higher density regions. An example of strength degradation is the formation of microcracks and the coalescence of these microcracks to form macrocracks. In post-compaction processes, environmental influences can also have an effect on compact integrity. An example of environmental influences is the splitting of pharmaceutical bilayer tablets due to the differential expansion of the two layers from ambient moisture uptake [7].

[1] Green compact: powder mechanically pressed into a solid in which powder particles are held together by cohesive forces from compaction alone.

The strength of compacted powder materials has been examined extensively throughout the fields of soil science, powder science, and pharmaceutical science [7]. The connection between the physics of the interactions between particle surfaces and the associated generation of bonding surface areas during compaction of powders has been recognized as the primary prerequisites of compact strength [6, 8].

The formation of a solid compact from powder materials can be subdivided into several mechanisms. Examples of mechanisms that in some way influence particle-particle bonding include: particle rearrangement, elastic deformation, plastic deformation, and possibly fragmentation. In the context of particle-particle bonding in the compaction process, the word "bond" refers to the formation of interfacial (contact) areas as a result of the well-known van der Waals interactions [6]. The van der Waals interactions (vdW) are strongly dependent on the separation and area of contact between surfaces. The magnitude of these interactions decreases rapidly with increasing distance according to $vdW \mu r^{-6}$.

For compressed powders that have undergone sufficient loading, the bonding between particle surfaces results in the creation of a solid compact with a certain degree of mechanical strength. During the compression stage of the compaction process, particle-particle bonding contact areas reach a maximum at the end of the compression where the compaction pressure is highest; however, these contact areas may be reduced once the pressure is removed. It has been suggested that if there is a sufficient degree of stored elastic energy capable of overcoming the work of adhesion at the contact interfaces, the result will be an increase in volume, a decrease in relative density, and the formation of defects [9]. Consequently, the formation of these defects results in a reduction of the material stiffness and degradation of cohesion in the compact. This material degradation refers to damage; a process characterized by the development, growth and

coalescence of microdefects. In powder compacted materials, microdefects show as microviods or microcracks. There is the possibility for these microdefects to coalesce to form macrocracks. When macrocracks are produced, the full separation of layers may follow, giving rise to the familiar capping and lamination failures (Figure 1.1 (a & b)) or tablet image problems such as chipping (Figure 1.1 (c)) often encountered in the compaction process.

Defects in powder compacts can arise from a variety of factors including any of the unit operations in the compaction process, and the quality of the raw materials in terms of their flow, compressibility, and ejection properties. The cost of defects and compact failures for manufacturers of pressed powder parts results in lost revenue, lost time, and decreased productivity. While a technician with considerable experience and training can often identify and resolve issues related to defects in the pressing of compacts, the intrinsic complexity that exists between multiple parameters and interactions requires a better understanding of the physics that underlies the process to avoid the possibility of being confronted with issues from the start. As such, this thesis is focused on the understanding defects and the corresponding damage in powder compacts and the effect this damage has on final compact strength.

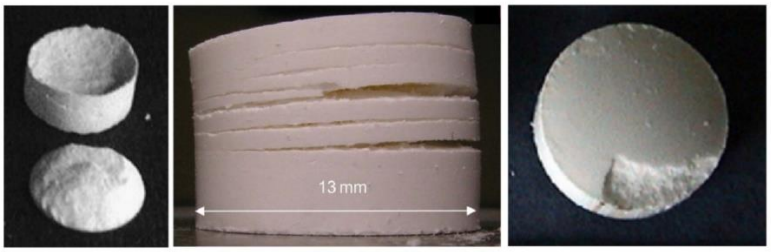

Figure 1.1 Examples of failures encountered during the compaction process: (a) capping (image adapted from [10]), (b) lamination (image adapted from [11]), and (c) chipping (image adapted from [12]).

1.1 Review of Prior Work

Research has proposed several possible explanations for the observed failures in powder compacted materials. Train (1956) [13] suggested that the development of a laminar crack through a material was the "spontaneous expansion" in both the axial and radial directions of the material exiting the die during the ejection stage (see Fig. 2(a)). While Train was able to recognize that lamination failures were in some way related to the expansion of the material from the die exit, the idea that expansion alone is responsible for damage and lamination failure is not entirely correct. Capping and lamination failures of compacted cylindrical tablets were also examined by Long (1960) [14] who proposed that this type of failure was the result of a "combination of axial expansion of the tablet exiting the die and residual die-wall pressure" (see Fig. 2(b)), another concept that is not entirely correct but it did highlight the importance of the residual die wall pressure and the die exit as a potential source for compact failures.

Although the work the Train and Long gave important initial insights into the possible mechanisms of capping and lamination, there has been very little attempt to predict these types of failures using modeling approaches. In addition, there have been very few experimental efforts put forth to substantiate their claims. In an attempt to understand the fundamental mechanisms for capping failures, a combined experimental and numerical investigation of cylindrical flat-faced and concave tablets comprised of lactose powder, a typically low tensile strength compacted material, was conducted by Wu et al. [9]. In this work, x-ray tomographic images of lactose tablets produced with flat and concave punches were compared for the purpose of visualizing the cracking upon unloading and ejection of the tablets. It was shown that the occurrence of cracking existed for all specimens tested with only a difference in the obliquity of observed cracking. The use of concave tooling was shown to result in less oblique cracking and

failures more consistent with lamination; whereas, flat tooling resulted in "cone" capping (Figure 1.1(a)). A numerical study using the finite element method (FEM) was conducted to analyze the stresses throughout the compacts during unloading. Their finite element analysis showed intense shear stresses that developed from top edge of the tablets towards the central axis of the flat-faced and concave tablets. From their experimental and numerical results, they claimed that one of the primary mechanisms for the occurrence of capping failures could be attributed to the formation of "shear bands" during unloading. While they were able to point out the importance of unloading as a potential source for the generation of cracking in powder compacts, their suggestion of shear banding as a mechanism driving crack propagation was not quite correct. Shear banding is a narrow zone of intense shearing, which develops during severe plastic deformation of the material [15]. It is unlikely that severe plastic deformation consistent with shear banding behavior would occur during unloading. In general, the mechanical properties of compressed powders exhibits a predominantly elastic behavior during unloading, as is evident from typical unloading curves observed in practice.

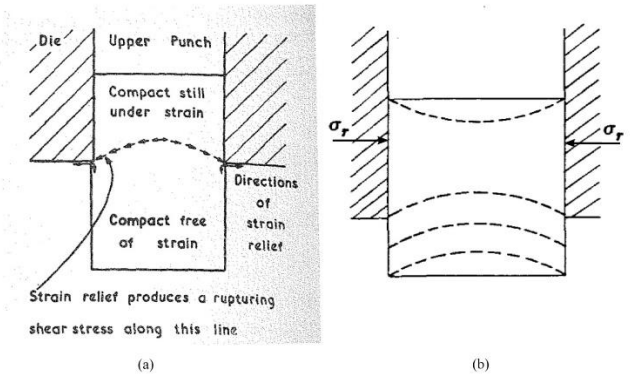

Figure 1.2 Schematic representations of lamination in (a) powder compacts suggested by Train (image adapted from [13]) and (b) capping and lamination failures as suggested by Long (image adapted from [14]). Radial stress is given by σ_r.

Since the seventies, path dependence and strength anisotropy have remained topics of interest in the fields of soil science and powder compaction [16-19]. More recently, Galen and Zavaliangos [20] have shown that mechanical strength of powder compacts depends not only on the powder properties and particle morphologies, but also on the path of loading. In this work, diametral compression tests of compacts were conducted to obtain the tensile strength of green compacts oriented in two different directions: perpendicular and parallel to direction of compaction. Both ductile and brittle powders were tested. It was shown that ductile materials showed an increase in strength anisotropy with an increase in density, whereas brittle materials became increasingly isotropic as density was increased. For the ductile powder materials, the tensile strength was shown to be lower in the direction normal to the prior compaction direction than in the transverse direction. In addition, it was also shown that particle shape influenced the degree of strength anisotropy. Elongated particles exhibited more strength anisotropy than the same material with particles in an equiaxed form (i.e. approximately spherical). They attributed the increased strength anisotropy for compacts composed of elongated particles to the increased morphological anisotropy of the preferential packing of the particles. The path dependence of compact strength was also examined. They were able to show that isostatically compacted powders either exhibited no strength anisotropy or very little strength anisotropy than die compacted powders depending on the particle shape. Equiaxed powder particles showed no strength anisotropy, whereas elongated particles show little strength anisotropy when compacted isostatically.

While the work of Galen and Zavaliangos was not specifically aimed at describing the mechanisms of defect formation (e.g. microcrack formation) in powder compacts, they did

address the importance of defects in the microstructure of compacts and the influence theses defects may have on strength anisotropy. They suggested that the value of strength in the different directions reflects not only the material properties but also the connection between defects and particle morphologies as a result of loading path. For example, they argued that despite the fact that the axial stress is larger than the radial stress in die compaction, larger cracks should be present normal to the axial direction due to the morphology of the compressed particles. They suggested that cracks could propagate more easily in the direction normal to the compaction direction without significant deflection and "path tortuosity" due to the compressed particle morphologies. Furthermore, they suggested that the removal of the compaction load in die compaction may promote opening of cracks in the normal direction while inhibiting crack propagation in the direction parallel to the prior compaction direction due to the presence of residual wall stresses. They argued that the possible presence of the larger cracks normal to the prior compaction direction was what attributed to the observed lower tensile strength in the prior compaction direction than in the transverse direction for ductile powders. In their work, they did not confirm the presence of these possible larger cracks in the prior compaction direction *via* experimental evaluation. Nevertheless, their hypothesis for the observed lower strength in the prior compaction direction of die compacted ductile powders represented an intriguing possibility for the mechanism of microcrack formation.

Other suggested causes for capping have been attributed to air entrapment in the interstices of the powder bed during the compaction process. The theory suggests that air that is trapped in the powder compact under pressure tries to escape once the upper punch starts receding during unloading, thereby causing the tablet to cap [21]. A study conducted by Mann et al. [22] suggested that the incidence of capping was related to the amount of air trapped in

powder prior to compaction. By steadily decreasing the speed of compaction, thereby allowing for the gradual release of as much air as possible prior to compacting the powder material, Mann et al. was able to show that the incidence of capping was reduced. However, this same study showed that the incidence of lamination was not influenced. Entrapped air has often been discussed as a potential source for the initiation of capping failures, but the role that entrapped air plays in promoting capping failures is not well understood. For example, it has been shown that capping and lamination can occur even in the case of partial vacuum [23].

To understand the complex behavior of powders during the compaction process, considerable research has been conducted using experimental approaches. However, due to the inherent complexity of the problem, computational modeling has emerged as a complimentary tool used to acquire a deeper level of understanding of the physics that drive the various mechanisms, such as the development of interparticle cohesion during compaction, and the generation of microcracks during unloading and ejection. Understanding of these physical mechanisms using computational modeling approaches allows for the prediction and optimization of the process without the need for considerable experimentation.

There has been a range of established and developing numerical methods that have been used to simulate the densification of powders subjected to compressive loads. Of the various techniques that have been implemented, continuum modeling used in conjunction with the finite element method (FEM) has remained the most common route for elucidating the behavior of powder materials in the compaction process. The most prevalent constitutive model used in continuum modeling of powder compaction is the Drucker-Prager cap (DPC) plasticity model [24-29], which uses a single state variable, typically relative density, to describe the evolution of the powder material during compaction where relative density (RD) is defined by the ratio of the

measured density to the theoretical density of the material (see Appendix A). The DPC model has shown great success in the prediction of density distributions of compacts subjected to various loading conditions for simple and complex shapes [26, 30-34]. This model incorporates the Drucker-Prager failure line [35], which describes the failure of powder material as a result of dilation (i.e. increase in porosity) due to shear, and the addition of a cap surface [36], which describes the densification of the powder material.

The use of the DPC model in the continuum model framework attempts to phenomenologically describe the kinematics and mechanical behavior of powder materials modelled as a continuum rather than as discrete particles. As such, the relative movements, orientation of contacting particles, and evolution of coordination number *Z*, the number of nearest neighbors in contact with the particle of interest, were not considered in this framework. Such considerations have been shown to affect the mechanical behavior of compacting powders [37-40] in the micromechanical analysis of contacting particles during compaction. Furthermore, the realization that the strength of compacted powder materials is related to not only the level of interparticle cohesion but also the discrete nature of damage or fracture at the contacts means that some fundamental aspects of strength as it relates to the formation of defects are missed using continuum modeling [41]. As an example, Koerner et al. [42] was able to show that samples of compacted powders produced under low stress triaxiality conditions exhibited higher transverse strengths for equally dense samples. *Stress triaxiality* is a term used to describe the stress state of the material in terms of the ratio of hydrostatic stress to deviatoric stress and is given by

$$\eta = \frac{-p}{q} \tag{1.1}$$

The terms p and q in equation (1.1) are hydrostatic stress and von Mises effective stress respectively. Thus, a stress state with a high stress triaxiality approaches more hydrostatic conditions responsible for volume changes in materials; with lower stress triaxiality, deviatoric stresses become more significant, which results in changes in shape of materials. In this work, samples compacted to identical densities by three different compaction methods, isostatic, die, and triaxial compression, all produced different strengths that varied by a factor of 2 to 3. Therefore, the assumption that the strength of compacted powders is only a function of dilation (i.e. increase in porosity), as assumed in the DPC model, shows a weakness in the continuum modeling approaches to properly predict the properties of cold compacted powders, especially as it pertains to strength predictions.

Due to the inability of continuum approaches to capture the complexity of the particulate nature of powder materials, discrete models have emerged as a way to assess the mechanical response of contacting particles. One of the most notable discrete modeling techniques that has been used is the distinct or discrete element method (DEM) [43-46]. The DEM, which treats a large collection of particles as discrete bodies that deform only at the contact, originated in the field of soil mechanics and granular flow [43, 47]. The DEM is closely related to molecular dynamics, though the DEM is generally distinguished by the inclusion of rotational degrees-of-freedom as well as interactions defined by particle-particle contact rather than by energy potentials.

The DEM offers a much-improved method for understanding the physical phenomena of the compaction of powders at the microscale over continuum modeling approaches. However,

current DEM implementations are lacking in their predictions when it comes to modeling the compaction of powders to high density. The reason for the inadequate predictions for high density compactions is due the choice of the implemented force-displacement contact model used. For example, many DEM model implementations describing compaction of powder materials typically incorporate constitutive contact models that ignore the effect of neighboring contacts that arise under high stress triaxiality conditions [44, 45, 48-50]. The consequence of these model implementations limits the validity of these results to low densities. Since the evolution of strength at contacts that exists in the unloading and ejection stages of the compaction process is coupled and history dependent on what happened during the compression stage, constitutive contact laws that address the interaction of neighboring contacts for high density compactions are necessary for the proper prediction of strength behavior.

Another discrete modeling technique developed for the purpose of addressing some of issues related to the DEM is the Multi-Particle Finite Element Method (MPFEM) [51-53]. This method is based on the finite element discretization of particles and offers several advantages over typical DEM model implementations. One advantage of this method is the freedom to model the compaction of particles with any geometric shape. In the DEM, the shapes of particles are limited to spheres or non-spherical shapes such as ellipsoids and arbitrary shapes by the clumping of particles together (multi-sphere method), which makes the development of constitutive contact laws for high density compactions incredibly difficult. Another key advantage of this method is the issue of neighboring contacts, which is naturally addressed in the MPFEM. Therefore, compactions to high density are not restricted. Furthermore, interfacial interactions such as cohesion and friction at contact interfaces are not compromised by geometric assumptions related to the way in which the potential change in contacting areas may evolve

with compaction. In the DEM, assumptions pertaining to the evolution of contact area during loading, unloading, and relative lateral motions are made, rather than capturing this phenomenon naturally as in the case of the MPFEM. While the MPFEM has several advantages over the DEM, these advantages come with a large computational cost. The computational complexity either restricts the use of the MPFEM to 2-D problems [52-54] or 3-D problems for a small number of particles [55]. As an example of the computational cost associated with implementing the MPFEM for 3-D problems, the closed-die compaction of 33 mono-sized spheres was simulated by Harthong et al. [56] using four CPUs with 2.93 Ghz processing power. The time per CPU required to complete the simulation was 18 days, which can be considered by many as being computationally prohibitive.

1.2 Particle-Particle Contact

With respect to the previous discussion of the available numerical methods used to describe the behavior of compacted powders, it is believed that the DEM provides the best combination of understanding of the particle level physics and computational efficiency. The DEM appears to be capable of capturing fundamental aspects of the compaction of powders to high densities and the corresponding strength and damage, albeit, with some further improvements to the constitutive contact laws. In simulations based on the DEM, numerous normal force and tangential force-displacement contact models have been implemented and used to describe the contact interactions between particles for various displacement and loading conditions (i.e. shear, flow, and compaction simulations). For particle interactions that arise in the DEM, Duran [57] and Zhu [58] divided the numerical techniques used into two broad categories called *soft sphere* models and *hard sphere* models. The difference between the two

categories of models is whether or not particles are approximated to be *soft*, where deformation is represented by penetration of the discrete elements or *hard* where penetration is forbidden. For the models used to simulate the compaction of powders, *soft* spheres are typically used**.** Figure 1.3 shows a schematic representation of the mutual approach of two soft spheres with radii R_i and R_j moving with velocities v_i and v_j indenting each other. The indentation of the two spheres is represented by the normal deformation δ_n and the tangential deformation δ_t, which give rise to the normal and tangential forces f_n and f_t respectively.

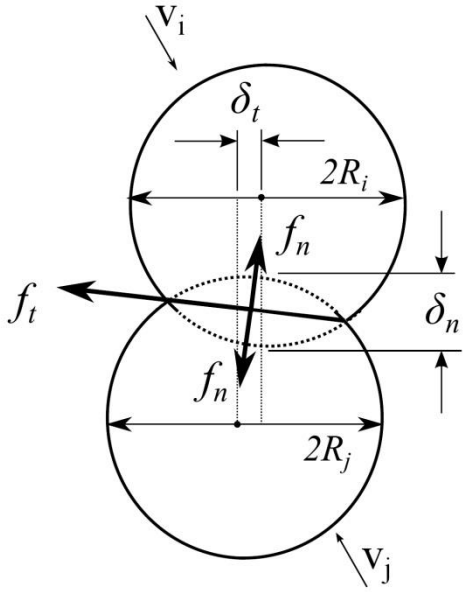

Figure 1.3 Mutual approach of two *soft* spheres indenting each other.

Contact interactions between surfaces of deforming particles under load originated in the field of contact mechanics and dates back to the work of Hertz [58]. In this classic paper, contact between two smooth elastic bodies was investigated and it was demonstrated that both the size

and shape of the zone of contact followed from the elastic deformation of bodies. The Hertzian normal contact force between two spheres or a sphere and flat surface is given by

$$f_n = \frac{4}{3} E^* \sqrt{R^*} \delta_n^{3/2} \tag{1.2}$$

where the equivalent elastic modulus E^* is given by

$$E^* = \left[\frac{1-\nu_i^2}{E_i} + \frac{1-\nu_j^2}{E_j} \right]^{-1} \tag{1.3}$$

The moduli E_i and E_j are the Young's moduli of the particles i and j, δ_n the normal indentation depth, and ν_i and ν_j the Poisson's ratios of the two materials. The reduced radius R^* is given by

$$R^* = \frac{R_1 R_2}{R_1 + R_2} \tag{1.4}$$

Further work to expand the theories of contact modeling was introduced by Sneddon [59], in which he was able to provide an analytical solution for the total load for an elastic material that must be applied to a punch to achieve a depth of penetration for a punch with an arbitrary profile. Another work included the extension to plastic deformation in the contact theories put forth by Storåkers et al. [60]. In their work, an analytical contact law based on the assumption of small deformations was developed and was termed the "similarity solution". This law was based on a Von Mises-type material, which strain hardened according to the power law relation

$\sigma = k\varepsilon^{1/m}$. The terms σ and ε were the uniaxial Von Mises equivalent stress and strain respectively and *k* and *m* were the strength index and strain-hardening exponent respectively [55]. For the monotonic, perfectly plastic (i.e. $m \rightarrow \infty$) mutual indentation of two spheres or a sphere and a flat surface, the normal contact force law is given by

$$f_n = k_n \delta_n = 6\pi c^2 \sigma_y R^* \delta_n \tag{1.5}$$

where the normal stiffness $k_n = 6\pi c^2 \sigma_y R^*$, σ_y the lower of the two yield strengths between the two contacting bodies, δ_n the indentation depth or deformation at the contact, and the parameter *c* an indentation invariant parameter that depends only on the hardening exponent *m*. The invariant parameter *c* prescribes that the velocities and strain rates of the deforming surfaces are independent of the size of the contact area; hence, this force law was deemed a "similarity solution" [61]. For the perfectly plastic contact between two bodies, $c^2 = 1.45$ and relates the contact radius, *a*, to the indentation depth, δ_n, by

$$a^2 = 2c^2 R^* \delta_n \tag{1.6}.$$

The similarity solution was implemented by several authors in DEM simulations of granular media [50, 55, 61]. Although the similarity solution has found use in simulations of powder compaction, it has been shown that this solution has limited applicability for accurately predicting the contact force-displacement behavior of spherical particles. The work of Mesarovic and Fleck [55] showed that the similarity solution is only valid during the initial stages of compaction where the influence from neighboring contacts is negligible. Tsigginos et al. [62] showed that significant de*via*tions from the similarity solution occurred for diametrically

loaded contacts (coordination number $Z = 2$) possessing ratios $E/\sigma_y < 1000$. Furthermore, it was shown that for ratios of $E/\sigma_y > 1000$, the solution is only applicable for a narrow range of contact radii. By adopting a yield strength not equal to the actual yield strength of the particles in contact, the solution can be brought into closer agreement with the actual contact force-displacement behavior, but only for the very early stages of compaction where particles are subjected to very low stress triaxialities.

The deficiency of Storåkers's similarity solution to predict proper stresses at the contact for particles subjected to high stress triaxiality stress conditions and for relative densities approaching one (fully dense) was addressed in the work performed by Procopio and Zavaliangos [53], in which 2-D MPFEM simulations were conducted. It was determined that the force-displacement law at the contacts of circular disks was not unique and depended on the coordination number, Z, of the particle. Furthermore, it was shown that the force-displacement curve asymptotically approached large forces with a corresponding large stiffness at the contact related to the elastic properties of the fully dense material as a relative density of one was approached. It was found that particles with higher coordination numbers approached this asymptotic limit sooner than particles with lower coordination numbers, which indicated that the interaction from neighboring contacts was highly dependent on the current Z.

A DEM normal contact model that accounts for the increase in stresses at the contact for particles subjected to high stress triaxiality stress conditions was introduced by Harthong et al. [55]. This contact model took a heuristic approach by incorporating the effect of local relative density changes on forces generated at the contact. In their approach, a two term contact model was developed where the first term represented the contact force generation as a result of contact deformation and the second term represented the forces developed at the contact as a result of the

increasing incompressibility of the particles as a relative density of one was approached. In the DEM framework used in their work, the changes in local relative density were calculated using a Voronoi tessellation. The unfortunate consequence of this proposed contact model in the DEM is the computational cost associated with calculating the Voronoi tessellation at each time step.

Another approach to account for the increase in forces generated at contacts as a result of closing of pores was introduced by Frenning [63, 64]. The normal contact model developed in this work utilized an approach put forth by Artz (1982) [37], in which the deformation of a particle was approximated by using an equivalent particle radius larger than the original radius during loading of the contacts. By use of this larger equivalent particle radius, deformation was taken into account by truncating spheres. Forces at contacts were defined in terms of a constant hardness, *H*. The use of the constant hardness in the calculation resulted in a unique contact force for a given deformation. This unique force was in contrast to the findings of Procopio and Zavaliangos in their work using the MPFEM. Similar to the contact model introduced by Harthong et al., this model requires an additional calculation for the equivalent particle radius, which would tend to increase computational cost.

A more recent work on the force-displacement law of contacts between spheres compressed to high relative densities was conducted by Tsigginos, Strong, and Zavaliangos [62]. In this work they were able to demonstrate by performing FEM studies on regular arrays of monosized particles that interactions between contacts begin when the plastic zones of neighboring contacts merged causing the force-displacement curve to deviate significantly from the case of Z=2 and to tends to infinity as deformation increased. Figure 1.5(a) shows the FEM simulation results for the force displacement behavior of particles isostatically compressed to high density for different coordination numbers. It was also determined that an increase in

contact force and the average contact pressure was associated with an increase in elastic energy as porosity was driven to zero. Figure 1.5(b) shows the normalized deformation as a function of coordination number for the isostatic compaction of regular arrays. In this figure, it is shown that there is a point at with deformations at the contact transitions from being easily compressible to becoming more difficult to compress. This transition was defined as the onset of the low compressibility regime. They were also able to show that the force-displacement law not only depended on coordination number, but also on deformation modes (isostatic versus non-isostatic deformation). In this work, a proposed deformation fabric tensor was developed to describe these different deformation modes where this fabric tensor was used to define a volumetric u_p and dev*ia*toric u_q particle deformation.

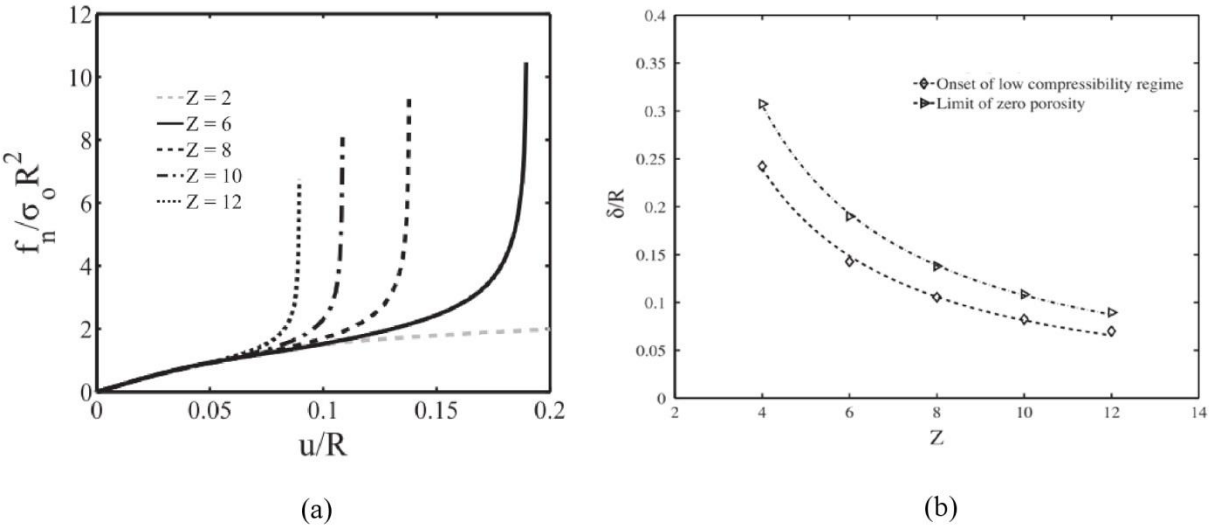

Figure 1.4 (a) Normalized force-displacement for different coordination numbers and (b) normalized deformation as a function of coordination number showing transitions to the low compressibility regime and the limit to zero porosity (images adapted from [62]).

1.3 Particle-Particle Contact Strength

Solutions to the problem of strength of adhesion between particle-particle contacts for two elastic spheres have been developed widely over the past decades. Of particular importance were the DMT (Dejaguin, Muller, and Toporov) [65] and JKR (Johnson, Kendall, and Roberts) [66] theories. These descriptions of contacts involving adhesion differed in only the size and compliance of the contacting bodies and the zone of influence of adhesion within the contact region. An analysis put forth by Tabor [67] was able to unite the two theories by the relationship of the Tabor parameter and showed that both the JKR and DMT models are limiting cases for elastically deforming spheres. An analytical model proposed by Maugis [68] incorporated both theories into a single solution and is currently considered the most accurate approach for the description of elastic adhesive solids. While the JKR, DMT, and Maugis theories are limited to bodies that deform reversibly, they gave the first insight into the strength of bonds between particles that have sizes on the order of a typical powder granule, which generally range from tens of μm to hundreds of μm.

Since particle contacts during the compaction of powders are loaded well beyond the elastic limit, a more relevant model than the JKR, DMT, or Maugis models for the cohesive behavior between contacting spheres has been developed by Mesarovic and Johnson [68]. This model considered cohesion between two spherical particles that had been initially plastically deformed and incorporated the superposition of two solutions: (i) unloading from the initially plastically deformed state under zero cohesion, and (ii) an adhesive solution in which a singularity at the outer radius of the contact existed. In this model, the pressure distribution in the zone of contact at the end of contact loading was assumed approximately constant and equal to

$$p_0 = H = \alpha\sigma_y \tag{1.7}$$

where p_0 the constant pressure distribution at the end of loading under the contact, H is the hardness of the material, and $\alpha \leq 3$ is a constraint factor that relates the hardness to the yield strength σ_y of the material. The net pressure in the region of contact and the net load as a function of the changing contact area are given by the sum of the cohesionless and cohesive solutions:

$$p(r,a) = \frac{2p_0}{\pi}\sin^{-1}\left(\sqrt{\frac{a^2 - r^2}{a_0^2 - r^2}}\right) - \sqrt{\frac{a}{\pi}}\frac{K}{\sqrt{a^2 - r^2}} \tag{1.8}$$

$$f_n = 2p_0 a_0^2\left[\sin^{-1}\left(\frac{a}{a_0}\right) - \frac{a}{a_0}\sqrt{1 - \left(\frac{a}{a_0}\right)^2}\right] - 2\sqrt{\pi}Ka^{3/2} \tag{1.9}$$

where a is the contact radius, r any point along the contact radius, a_0 the contact radius of the initially deformed particle, and K the stress intensity factor, a factor used in fracture mechanics to characterize the stress state near the tip of a crack. This stress intensity factor is given by $\mathrm{K} = \sqrt{2\mathrm{W_{ij}E^*}}$, where W_{ij} is the work of adhesion between surfaces of particles i and j. If equation (1.9) is divided through by the product of the area of initial contact and the initial pressure at the end of loading, the force in non-dimensional terms is given by

$$\bar{f} = \frac{f_n}{f_{\max}} = \frac{2}{\pi}\left[\sin^{-1}(\zeta) - \zeta\sqrt{1 - \zeta^2}\right] - 4\left[\frac{1}{\pi}\left(1 - \frac{2}{\pi}\right)\chi\right]^{1/2}\zeta^{3/2} \tag{1.10}$$

where f_{max} is the maximum force at the end of loading, ζ the normalized residual contact a/a_0, and χ the cohesive parameter given by

$$\chi = \frac{\pi}{2\pi - 4} \frac{W_{ij} E^*}{p_0^2 a_0} \tag{1.11}$$

The cohesive parameter χ represents the ratio of the cohesive energy to the elastic energy stored in the solid, and is a measure of cohesion at the contact. In equation (1.8), the first term represents the unloading with no cohesion and the second term is unloading with the addition of adhesion. In this model, when the cohesive parameter $\chi \neq 0$, unloading at the contact beyond full unloading ($fn = 0$) gives rise to tensile stresses ($f_n < 0$). As the load at the contact is further reduced, a maximum tensile force, denoted by f_{min}, is reached. The two surfaces in contact begin to loose load carrying capacity upon further unloading. For values of $\chi \leq$ approximately 0.1, the critical force (pull-off force) required to separate the two particle surfaces is given by

$$f_{min} \approx 1.09 \chi f_{max} \tag{1.12}$$

The critical pull-off force given by equation (1.12) represents a simplistic definition of the critical cohesive forces at the contact. Figure 1.5 shows the normalized load versus normalized contact area during unloading for different values of the cohesive parameter χ. The grey dots in Figure 1.5 represent the critical pull-off forces at which the tensile forces at the contact lose their load carrying capacity. Unloading of the contact area beyond the critical area a_c at which the critical pull-off force is reached represents the point where the particles snap apart.

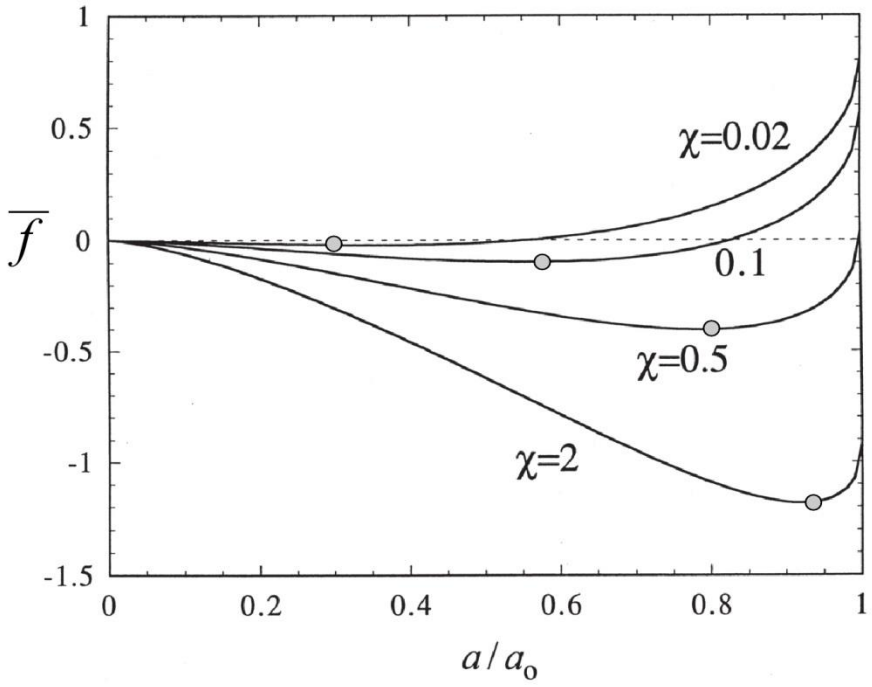

Figure 1.5 Normalized load during unloading as a function of normalized residual contact area for different levels of the cohesive parameter χ (image adapted from [69]). The added grey dots symbolize the maximum tensile load that can be supported for the different levels of the cohesive parameter.

The work presented by Mesarovic and Johnson [69] represents the first rigorous analysis for the unloading of cohesive contacts for which an analytical solution to the problem was developed. Like any model, there are limitations due to the many assumptions made. In the case of the MJ model, unloading was considered to occur under purely linear elastic conditions without the consideration of plasticity or any other dissipative energy mechanisms that may be present. Also, this model considered the evolution of the forces generated as a result of the unloading contact area for two particles only. The unloading of a contact for a particle that has

been initially subjected to high stress triaxiality conditions from multiple contacts may result in a completely different picture. A result of the aforementioned assumptions, this model would predict a linear increase in strength with an increase in compaction pressure for a particle assembly, which would result in an incorrect prediction. Another assumption of this model was that cohesion and elasticity during unloading were inseparable in that the level of elastic unloading at the contact is completely determined by the level of cohesion at the contact. While this assumption may be correct for purely linear elastic unloading, it is not clear whether or not this assumption holds when energy dissipation mechanisms such as plasticity, friction, or other mechanisms are present.

While many of the DEM-based simulations appearing in the literature have been concentrated towards granular flow [43, 70-74] and rheological behavior related to shearing of dense packings [47, 75-77], compaction of particle assemblies have also been considered. Thornton and Antony (1998) [46] implemented the model of Cundall and Strack (1979) to simulate the quasi-static deformation of dense packings for axisymmetric compressions of elastic spheres to low compacting mean pressures of 100 kPa. For the compaction of particles subjected to plastic deformation, 2-D DEM simulations of both frictionless and sticking contacts of circular cylinders were performed by Redanz and Fleck (2001) [45]. In their work, predictions from their DEM model revealed that frictionless particles resulted in low macroscopic stresses both for hydrostatic compaction and die compaction due to the substantial rearrangement that took place in the early stages of compaction. In contrast, their results showed that a stiffer compaction response and an overall larger yield surface was obtained when interparticle friction μ was increased. They were able to show that for fully sticking contacts ($\mu = \infty$), the size and shape of the yield surfaces generated approached that of yield surfaces generated when particles move in

an affine motion manner, a motion that preserves parallelism between paths, and were approximately twice the size of yield surfaces for frictionless particle compactions. It has been shown that the size and shape of the yield surfaces when using the affine motion assumption produces only a very minor dependence on the level of interparticle friction [38, 78]. The significance of Redanz and Fleck's work highlighted the importance of particle rearrangement and its effect on the compaction response.

A study by Heyliger and McMeeking (2001) [44] was published for isostatic and closed die compaction of a 3-D assembly of perfectly plastic particles for both cohesionless and fully cohesive cases. Similar to the published work of Redanz and Fleck, the affine motion assumption was not considered, which produced similar conclusions with regard to the size and shape of predicted yield surfaces. The yield surfaces generated were significantly smaller than predictions using the affine motion assumption. Similar to Redanz and Fleck's model when using an interparticle friction $\mu = \infty$ (i.e. fully sticking contacts), fully cohesive contacts in Heyliger and McMeeking's work also resulted in a closer agreement to yield surfaces obtained when using the affine motion assumption. These results are no surprise since infinite cohesion or infinite friction should result in little local rearrangement of particles and a response that is closer to the affine motion assumption.

For the works performed by Redanz and Fleck, and Heyliger and McMeeking, mechanical independence of contacts was considered. Therefore, results obtained from these works can be considered to be only valid where contact impingement between contacts does not occur. Moreover, these works did not consider the discrete nature of contact loss during unloading and ejection cycles. Nevertheless, these works provided a marked improvement over the micromechanical model introduced by Fleck [79], which derived the macroscopic response from

local plasticity at interparticle contacts based on the assumption of affine motion of the particle kinematics. As a result of this affine motion assumption, the macroscopic stress and yield surface predictions are seen as upper bounds. The work of Redanz, Fleck, Heyliger, and McMeeking when using the DEM addressed the effect of particle rearrangement on the macroscopic response, which showed a significant softened response of yield loci when compared to yield loci obtained from using the affine motion assumption. The effort of their work in the DEM was able to provide a significant step forward in the understanding of particle motion, contact forces and contact orientations, as well as pertinent macroscopic quantities for an assembly of particles subjected to external loads and displacements.

Of particular interest to the work presented in this thesis, were the DEM simulations presented by Martin et al. [48, 49, 80, 81]. In the work by Martin on the unloading of powder compacts and the resulting strength [80], compaction was modeled by employing the unit problem description for the elastoplastic deformation of two spheres defined by Storåkers et al. termed the "similarity solution" [60]. Unlike the assumptions of Redanz and Fleck, and Heyliger and McMeeking of either cohesionless or fully cohesive contacts, unloading was modelled using an analytical model for the cohesive contact of two spheres given by Mesarovic and Johnson's (MJ) singular solution [69]. By the utilization of the two models for loading and unloading, Martin was able to provide a more realistic depiction of the behavior of pressed powders under loading and unloading conditions in which failure at the contacts was allowed to occur. Isostatic compaction and unloading of an assembly of particles in 3-D DEM simulations were analyzed for varying relative densities ranging from 0.7 to 0.95. Equal strains applied to particles representing the outer boundary of cubic samples facilitated the compaction and unloading of particle assemblies. Periodic boundary conditions were imposed for these outer boundaries.

The work by Martin gave promising results for the predictive capabilities of DEM as a tool to understand the behavior of compacted powders for conditions where cohesion and the loss of cohesion at contacts were allowed to occur. Figure 1.6(a) shows compaction pressure, P, normalized by yield strength, Σ, versus relative density [80]. An important observation from this result was the apparent nonlinearity that exited at the end of each unloading curve. This nonlinearity is often observed experimentally for the compaction of powders and can be attributed to the opening of contacts [41, 82]. Another important result from Martin's work can be seen in Figure 1.6(b), which shows the change in the coordination number during unloading as a function of average value of the cohesive parameter from the MJ model, $\bar{\chi}$ for varying relative density compactions. The cohesive parameter χ characterizes the level of adhesion and signifies the ratio of adhesive energy to the elastic energy at the contact. The result in Figure 1.6(b) shows that particles with higher initial coordination numbers (Z_0) loose the most contacts, but more importantly, compacts that have been compacted to higher relative densities are those that experience the largest change in coordination number. This result indicated, to some extent, that damage may be more severe for higher relative density compactions. Figure 1.6(b) also shows that the change in coordination number (loss of contacts) for lower average values of cohesion at the contact χ was more severe, while for higher cohesion at the contact the change in Z dropped off significantly. This observation indicated the ability of the DEM to properly predict the expected behavior for cohesive materials.

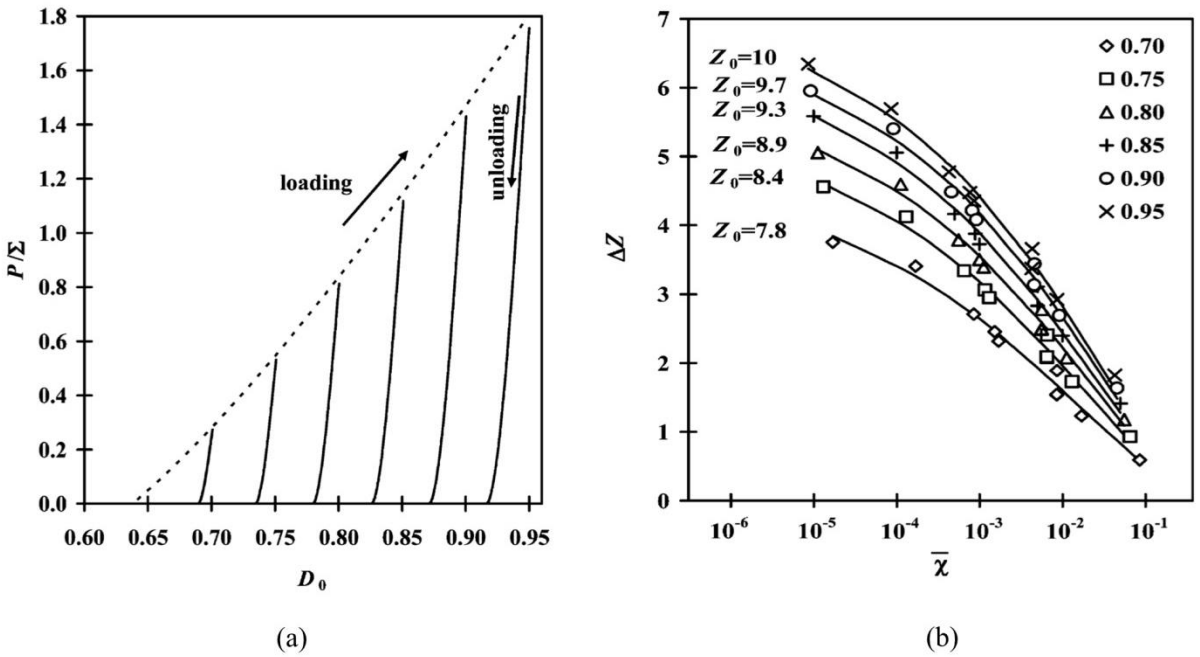

Figure 1.6 Results from Martin's work showing (a) normalized pressure versus density prediction, and (b) change in coordination number ΔZ at the completion of unloading versus $\bar{\chi}$.

While the work of Martin et al. represents an important step forward in the understanding of the behavior of compacted powders, there are aspects of this work for which the predicted behavior of compacted powders using Martin's implementation are lacking. The use of Storåkers's similarity solution precluded the use of this model for compactions to high density. Figure 1.6(a) shows the effect of using Storåkers's similarity solution where an unrealistic loading pressure-density curve was observed for relative densities approaching 95%. The pressure-density curve in Figure 1.5(a) increases linearly over the entire relative density range from the initial relative density, $RD_0 \approx 0.64$, to approximately 0.95. Both theory and experimental work demonstrated that as a relative density of one was approached, the pressure-density relationship exhibited an exponential or power law increase in pressure [29, 83-85]. As a

result of the use of the similarity solution in this work, Martin's implementation also predicted a linear dependence of strength on compaction pressure, which was not realistic. Similar to exponential or power law increases in compaction pressure with increasing density, strength also has been shown to increase exponentially with increasing compaction pressure.

Other aspects of Martin's implementation that deserve further consideration were the predictions of strength from only isostatic tensile conditions and the use of periodic boundaries. *Periodic boundaries* are a set of boundary conditions that are used for approximating a large (infinite) system by using a unit cell. The unit cell, typically a hexahedron, is replicated throughout space to form an infinite lattice. In DEM simulations, any particle leaving the periodic unit cell boundary at one end will re-enter the unit cell boundary at the other end. While periodic boundaries have been used extensively in DEM simulations involving flow, shearing, and compaction of powders, predictions of damage (see Figure 1.6(b)) and the effect this damage has on strength using periodic boundaries will produces a *global* or isotropic prediction of damage. In general, the microstructural evolution of powder particles during the compaction process produces a heterogeneous solid compact at the end of loading. Failure mechanisms in powder compacts, and other heterogeneous solids such as concrete or cemented granules, are characterized by complex failure modes under various local loading conditions and typically result in anisotropic damage due to their heterogeneous microstructure [86, 87]. Since Martin's work was primarily concerned with predictions of strength from isostatically compacted samples using isostatic tensile testing, the use of boundary conditions would be less problematic. It is expected that isotropically compacted samples would possess a more isotropic microstructure. However, it is more reasonable to consider damage generation and the effect this

damage has on strength from closed die compaction simulation results, since closed die compaction is the most common and practical means of producing components from powders.

1.4 The Discrete Element Method for the Compaction of Powders

The discrete element method has been widely covered in the literature by many researchers since its inception by Cundall and Strack in 1979. As such, this section is intended to only introduce some of the key concepts of the method and to provide a basic overview of the governing equations used to compute motions and forces in the DEM, as well as introduce general normal contact models that have been used to simulate the compaction of powders. A comprehensive review in terms of the general understanding of the DEM method has been established by O'Sullivan [88]. Another review on the theoretical developments, major applications, and findings in the DEM was produced by Zhu et al. [58, 89].

Particles in the DEM can have both translational and rotational motion. As the particles undergo movement in the DEM, interactions with neighbor particles and walls may occur where energy and momentum transfer of contacting bodies will occur. The changes in positions and velocities due to the interactions with neighboring particles, walls, and gravitational forces are calculated using Newton's second law of motion. The equations that govern the translational and rotational motion of particles are given by:

$$m_i \frac{d^2\mathbf{x_i}}{dt^2} = \sum\nolimits_c \mathbf{f_i}^c + m_i\mathbf{g} \tag{1.13}$$

$$I_i \frac{d\boldsymbol{\omega}_\mathbf{i}}{dt} = \sum_c \mathbf{M}_{ij} \tag{1.14}$$

where m_i, t, $\mathbf{f}_\mathbf{i}^\mathbf{c}$, $\mathbf{g}$, I_i, $\boldsymbol{\omega}_\mathbf{i}$, and M_{ij} are the mass, time, contact force, gravitational constant, moment of inertia, rotational velocity, and torque respectively. The subscripts *i* and *j* in equations (1.13) and (1.14) represent particle *i* in contact with particle *j*. From the use of the equations (1.13) and (1.14) the positions at each time step are computed using the central-difference Verlet integration method in which the newly updated positions produce a neighbor list from a contact detection algorithm. In the DEM, two spherical particles with radii R_i and R_j interact if they are in contact, where contact is defined such that the normal overlap or deformation of the *soft* spheres,

$$\delta_n = R_i + R_j - (\mathbf{r}_i - \mathbf{r}_j) \cdot n \tag{1.15},$$

is greater than zero ($\delta_n > 0$). In equation (1.15), *n* is the unit vector directed from the centers of particle *i* and *j*, and $\mathbf{r_i}$ and $\mathbf{r_j}$ are particle centers of particles *i* and *j*. Based on the updated positions and the corresponding contact deformations that arise, forces are computed at each contact from constitutive contact laws that are functions of both the normal and tangential deformations.

Once positions and velocities have been updated and contact for each individual particle has been established at each increment in DEM simulations, forces are calculated based on the deformations of the overlapping particles. These forces are calculated from constitutive contact models that incorporate the use of springs, dashpots, and sliders as a mean of describing the force as a function of deformation. These springs, dashpots, and sliders represent the stiffness

generated at the contact in which the generalized force is typically given in the form of Hooke's law:

$$f = k\delta \tag{1.16}$$

where k is the stiffness of the spring connecting two contacting particles from their respective centers of mass. The spring stiffness can be defined as a function of several parameters (e.g. temperature, porosity, degree of hardening, etc…), and can be defined as linear or nonlinear. In general, imposed contact models in the DEM tend to be relatively simplistic in their definition of describing the generation of forces at the contact. Perhaps the two most important reasons for simplicity are: (1) decreased computational cost in the DEM and (2) fewer parameters for parameter extraction from experimental results.

1.4.1 Time Integration in the DEM

In general, the DEM's computational requirement is large due to the necessity of numerical stability in the explicit integration scheme that the DEM uses. The integration scheme most often used in current DEM implementations is the central-difference Verlet time integration method [90] or some variation of this method. In this integration scheme, the state of the system is calculated at a later time $t + \Delta t$ from the state of the system at the current time t. The accuracy of the solution at each time step is dependent on the square of the time increment imposed in simulations. Thus, the smaller the imposed time increment per iteration in the DEM, the more accurate and stable the solution at each time step will be. Likewise, an imposed time step that is

too large may lead to numerical instability in the system. It has been suggested by Cundall and Strack (1979) that the critical time step chosen should be less than a time step that would allow for disturbances from an individual particle to propagate further than its nearest neighbors in a single time step.

The imposed time step used in DEM simulations is the time increment over which positions and forces are computed for a single iteration. This imposed time step must be sufficiently small to ensure both accuracy and numerical stability of the solution at calculation iteration. Proposed methods have been conducted to determine the largest possible time step, termed "the critical time step" Δt_c, to be used in DEM simulation based on several factors, such as particle density, particle size, maximum stiffness generated at contacts, and speed of simulations in terms of moving boundaries [43, 91, 92]. For quasi-static simulations, an upper limit for the critical time step is related to the time required for a Rayleigh wave to propagate through the minimum size particle in the particle assembly [93]. The critical Rayleigh time step is proportional to $\sqrt{\rho / G}$ where ρ is equal to the particle density and G is the shear modulus of the particle assembly. A study performed by O'Sullivan and Bray [91] for regular array of particle assemblies showed that the critical time step for quasi-static 3-D simulations should be less than $0.17\sqrt{m/k}$, where m is the mass of the smallest particle, and k is the largest expected stiffness generated at a contact. In O'Sullivan and Bray's work, the use of regular arrays allowed for complete force transmission between individual particles to percolate throughout the assembly. In this case, the critical time step given by O'Sullivan and Bray can be thought of as a conservative critical time step. Another suggested critical time step was presented by Itasca (2003) (Particle Flow Code PFC manual) [94]:

$$\Delta t_c = \sqrt{\frac{m}{k}} \tag{1.17}$$

For typical powder granules with sizes ranging from tens of μm to hundreds of μm used in the compaction of powders, the mass of a single particle is on the order approximately 10^{-9} – 10^{-8} kg. The critical time step given by equation (1.17) for typical stiffness on the order of approximately 10^6 N/m would yield $\Delta t_c \sim 10^{-8}$ s, which represents a critical time step that may result in a prohibitively slow simulation run, especially for large particle systems. A common method to "speed-up" DEM simulations is to artificially increase the particle density, which is known as *mass scaling*. Mass scaling is typically only suggested for quasi-static simulations where dynamic effects from inertia do not pose a significant effect. For powder compaction simulations, quasi-static conditions are typically considered.

For powder compaction simulation using the DEM, not only is it important to consider the critical time step in terms of the contacting pairs, be it neighboring particles or walls, but also the potential for excessive overlap that may result from too high of a velocity imposed from moving boundaries. The maximum possible velocity of a moving wall in contact with a particle within an increment when using explicit integration schemes can be related to the critical time step given by Kremmer and Favier [95]:

$$\Delta t_c = \frac{\alpha R_{\min}}{|v_k|_{\max}} \tag{1.18}$$

where α is a fraction of the smallest particle having a radius equal to R_{min}, and $|v_k|_{\max}$ is the magnitude of the largest velocity of a moving boundary such as a rigid wall in contact with a particle. Typical values, as reported by Kremmer and Favier, range between 0.0025 and 0.005 for α. Another suggested critical time step for minimizing the influence of the dynamic and inertial effects from an imposed strain rate $\dot{\varepsilon}$ applied to the powder assembly was proposed by Tardos et al. [96]. A dimensionless shear strain rate $\dot{\gamma}^*$ was used to asses inertial and dynamic effects in which they found that a $\dot{\gamma}^* < 0.15$ corresponds to quasi-static conditions. Thus, for a particle assembly subjected to a moving boundary having a strain rate equal to $\dot{\varepsilon}$, the critical time step is given by

$$\dot{\gamma}^* = \dot{\gamma}\left(\frac{d_p}{g}\right)^2 \tag{1.19}$$

where d_p is the particle diameter, g the acceleration (for example, gravitational acceleration), and $\dot{\gamma}$ the shear strain rate, which was assumed to be on the order of $\dot{\varepsilon}$ for a moving boundary of the particle system.

1.4.2 Energy Minimization in the DEM

A common approach taken in the DEM for the purpose of minimizing the inertial and dynamic effects is the application of damping. Damping can be applied in numerous ways, which include both local and global damping. For local damping in the DEM, a velocity

dependent force at the contact level is imposed such that the relative velocity of the particles in contact acts to reduce the force by introducing a so-called viscous damping force. This type of contact model is better known as the spring-dashpot model. For a normal contact, this force is given by

$$f_n = k\delta_n - \gamma v_n \tag{1.20}$$

where γ is the viscous damping coefficient having units of force/velocity and the other variables have their usual meaning. As the name suggests, this viscous damping coefficient, when incorporated into the contact model, has the effect of perhaps introducing viscoelastic/plastic behavior artificially. From equation (1.20), it is realized that particles with relatively low velocities will have negligible effect on the overall force; whereas, particles with high velocities will be greatly affected by the damping. For the beginning stages of compaction, this type of contact will be highly active. As densification continues, damping will have negligible effect on the overall response of the system as most of the particles will be in contact resulting in the interference of large rotational or translational motion.

Similar to the local damping, a global damping of the system can also be implemented. This type of damping is tantamount to the system of particle existing within a viscous medium where the total force on a particle is given by

$$f_i = \sum_{c}^{Nc} \left(f_c^N \boldsymbol{n} + f_c^T \boldsymbol{t} \right) - \gamma_B \boldsymbol{v}_i \tag{1.21}$$

The sum of all normal and tangential contact forces on a particle *i* is reduced by the product of a "bulk" viscous damping coefficient γ_B and the velocity of particle *i*. Unlike local damping where it is possible that only a small number of particles will be affected during compaction, global damping affects the entire system as a whole and can be used to rapidly drain the kinetic energy from the system. Therefore, a global damping procedure can be useful where dynamic effects are great; however, this type of damping can radically affect the overall response of the system by artificial over-damping.

Another damping procedure proposed by Cundall [97] is an alternative damping in which forces generated at each of the contacts is proportional to the magnitude of the accelerating forces (i.e. resultant forces from all forces on an individual particle). This procedure of damping involves damping of vibrational modes rather than steady motion and is referred to as *local non-viscous damping*. The local non-viscous damping force proposed by Cundall was given by

$$f_d = -\varphi \left| \mathbf{f}_p \right| \text{sign}\left(\mathbf{v_p} \right) \tag{1.22},$$

where f_d is the damping force, φ a damping constant (typically 0.7), $\mathbf{f_p}$ the resultant force on particle *p*, and sign($\mathbf{v_p}$) the velocity acting in the opposite direction of the resultant force.

1.4.3 General Normal Contact Models Implemented in the DEM

Several normal contact models for elastoplastic adhesive contact have been introduced to describe the interaction between particles in granular materials. Examples normal contact models that incorporate both plastic and cohesive contact have been introduced by Schubert et al.

(1976)[98], Maugis and Pollock (1984) [99], Johnson [100], Thornton and Ning (1991) [101], and Tomas (2000) [102] just to name a few. Two general normal, adhesive elastoplastic contact models developed by Luding [92, 103-105] and Walton and Johnson [106] will be explored further as these contact models consist of some key elements that have importance to the proposed normal contact model introduced in Chapter 3.

1.4.3.1 Luding Model

Luding has introduced a model for the purpose of obtaining the relevant macroscopic mechanical behavior of granular assemblies under various loading conditions [105]. This model is a four parameter model (k_1, $k_2^{\max}$, k_c, and δ^*) that is defined by three distinct linear springs stiffness for contacting pairs, where a spring stiffness k_1 is the stiffness representing the loading phase of the contact, k_2 is the stiffness representing the unloading of the contact pairs, and k_c is the stiffness representing the cohesive stiffness. From these stiffness, the piece-wise defined force as a function of overlap is given by

$$f_n = \begin{cases} k_1\delta_n & \text{if } k_2\left(\delta_n - \delta_0\right) \geq k_1\delta_n \\ k_2\left(\delta_n - \delta_0\right) & \text{if } k_1\delta_n > k_2\left(\delta_n - \delta_0\right) > -k_c\delta_n \\ -k_c\delta_n & \text{if } -k_c\delta_n \geq k_2\left(\delta_n - \delta_0\right) \end{cases} \tag{1.23}$$

where, δ_0 is defined as the plastic contact deformation. Figure 1.7 shows a schematic representation of the Luding model for normal contact between two spheres.

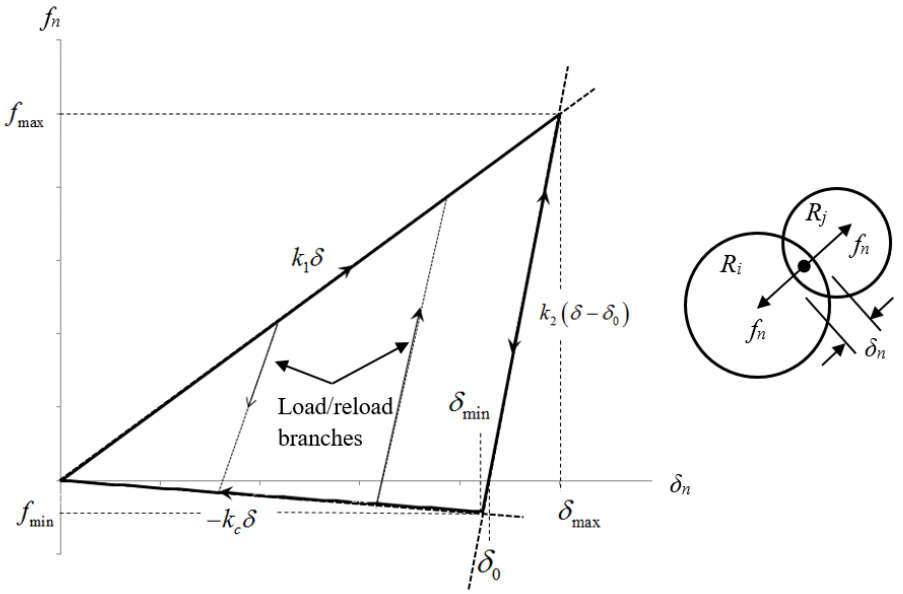

Figure 1.7 Schematic of the force-displacement contact model developed by Luding for two particles in contact.

From schematically illustrated force-displacement contact law shown Figure 1.7, when two particles come into contact and are compressively loaded, the contact force increases linearly with a slope equal to the loading stiffness k_1. The linear increase in force with deformation is consistent with Storåkers's similarity solution for elastic-perfectly plastic contact deformation discussed in section 1.2. Upon unloading, the contact force follows the unloading/reloading branches with a slope given by the unloading stiffness k_2. The unloading/reloading stiffness is defined by a linear interpolation between the loading stiffness k_1 and an imposed maximum stiffness $\hat{k}_2$:

$$k_2 = \begin{cases} \hat{k}_2 & \text{if } \delta_{\max} > \delta^* \\ k_1 + \left(\hat{k}_2 - k_1\right)\dfrac{\delta_{\max}}{\delta^*} & \text{if } \delta_{\max} \le \delta^* \end{cases} \quad (1.24).$$

where the δ^* is a limiting overlap that accounts for the increase in unloading stiffness with contact deformation up to this limiting overlap, and is given by

$$\delta^* = 2\frac{\hat{k}_2}{\hat{k}_2 - k_1}\theta_f R^* \quad (1.25).$$

The parameter θ_f is a unitless parameter used to define the limiting overlap at which a maximum unloading stiffness is reached. If the two particles are loaded beyond this limiting overlap any unloading will result in an unloading along $\hat{k}_2$, which can be thought of as the asymptotic limit of unloading related to the elastic properties of the fully dense material. Unloading beyond the plastic overlap δ_0 results in tensile forces at the contact until the maximum adhesive force is reached. The maximum adhesive force, given by $-k_c\delta_{min}$, is determined by the intersection of the unloading and cohesive branches of the model. Further unloading leads to a decrease in the strength at the contact described by the curve having a constant cohesive stiffness k_c.

1.4.3.2 Walton and Johnson Model

The model by Walton and Johnson [106] is shown schematically in Figure 1.8. The primary differences with this contact model and the model proposed by Luding are related to the separation of contacts and reloading at the contact. In this five parameter model (k_1, k_2, k_3, k_4,

and f_{0c}), if contacts are unloaded such that deformation drops below zero, separation of the contact does not occur and is subjected to tensile forces until the separation between the contacting surfaces is equal to δ_{b0}. This type of behavior is similar to the JKR theory of elastic adhesion, in which the required tensile force required to break a contact is larger than the maximum force at the end of loading of the contact. Unlike the Luding Model, further unloading beyond the minimum force f_{min} required to initiate contact separation results in complete contact separation at the *breaking deformation* δ_b. The deformation, δ_b, is defined by the intersection of cohesive branch with a slope equal to k_3 and δ_n – axis. Although the decrease in strength at the contact does not follow the same cohesive branch given by the Luding model, the minimum force required to initiate contact separation f_{min} is defined by an adhesion limit, which is indistinguishable from the behavior for maximum adhesive forces described by the Luding model. The adhesion limit in this model is given by the line $f_{min} = -k_4\delta_n - f_{0c}$, where f_{0c} is the cohesive strength of the contact at zero overlap.

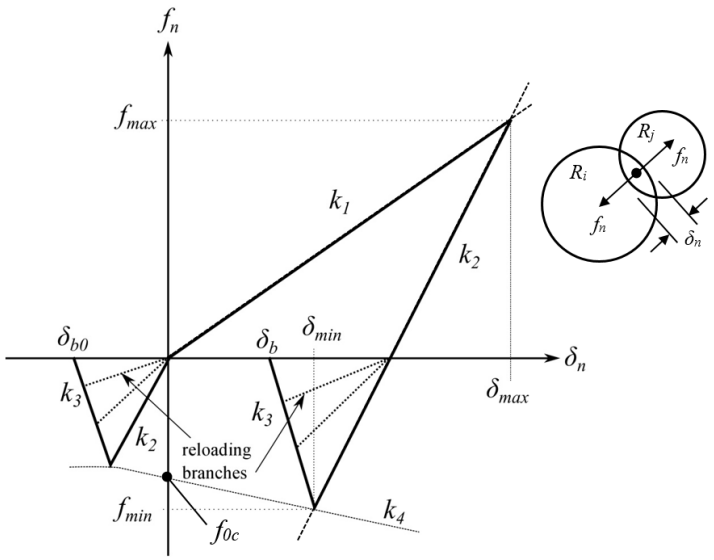

Figure 1.8 Schematic of the force-displacement contact model developed by Walton and Johnson for two particles in contact.

1.4.4 Tangential Forces at a Contact

An important contribution to the overall force at the contact includes the tangential contact response. In comparison to the normal contact force at the contact, the tangential contact response is arguably a more difficult subject in terms of understanding. The work by Mindlin and Deresiewicz (1953) [107] forms the basis for many of the tangential force laws that have developed over the past decades. The most notable of tangential force laws incorporates the use of the Coulomb criterion (tangential force = $T = \mu f_n$), which represents the simplest relationship between shear stresses acting parallel to the plane of contact and normal forces acting perpendicular to the plane of contact. Other more complicated models have been introduced by Thornton and Yin [108] and Vu-Quoc et al. [109]. In the model introduced by Thornton and Yin, a nonlinear cohesive, tangential force law for elastic particles was developed, in which the tangential stiffness at the contact depends on the current normal force, the current tangential force, and the load history. The Vu-Quoc et al. model is a tangential force-displacement law that accounts for the effect of plastic deformation at the contact while neglecting cohesion at the contact. In terms of implementation into the DEM, the simple Coulomb criterion is most often used. Using the Coulomb criterion, the tangential force is modeled as either being in a state of gross sliding as defined by the Coulomb criterion, or in a state of sticking with a tangential force proportional to the product of the tangential stiffness and current tangential displacement:

$$T = \begin{cases} -k_t \delta_t & k_t \|\delta_t\| \le \mu f_n \\ -\mu f_n & k_t \|\delta_t\| > \mu f_n \end{cases} \tag{1.26}$$

where k_t is the tangential stiffness, μ the interparticle friction, and δ_t the tangential displacement as shown in Figure 1.3. Work on properly identifying the value k_t by experimental means has been rather understate in the literature. However, numerical simulations have suggested that value of k_t should range from 0.5-5 times the normal stiffness [110].

1.5 Goals of This Work

The objectives of this research were: investigating and analyzing crack formation in powder-die compacted materials, the description of damage and the associated effects damage has on the strength in powder-die compacts, and the generation of relevant predictive models *via* computational modeling that will allow for process optimization. To unravel the complex behavior of powders during the die compaction process, considerable research has been conducted using experimental approaches. Results obtained *via* experimental evaluation have provided exceptional insight into the mechanical behavior of compacted powders in terms of describing the correlations between the multiple parameters and interactions that take place during the process. While qualitative descriptions of the causes of failures in compacts give insight into the degradation of strength in the compaction process, there is still a need to understand the mechanisms that give rise to these failures, such as capping and lamination. Furthermore, the question of when defects form—in die or as a result of ejection from the die—also needs further investigation.

Due to the inherent complexity of the problem, computational modeling has emerged as a complementary tool used to acquire a deeper level of understanding in terms of the physics that drive the various mechanisms, such as the development of interparticle cohesion during compaction, and the generation of microcracks during unloading and ejection. Understanding of

these physical mechanisms using computational modeling approaches will allow for prediction and optimization of the process without the need for considerable experimentation. As previously discussed, many researches have used the DPC model to describe density variations in compacted components of varying shapes with great success. However, in terms of modeling strength development during the compaction process, the DPC and other phenomenological models fail in their prediction because fundamental aspects of failure at the contact level (i.e. microcracking) are not taken into account. While the MPFEM offers the highest fidelity in terms of providing the greatest insight into the problem of compaction, the computational complexity of this method restricts its use to non-representative descriptions of the behavior of powder compacted materials. Therefore, this research considers another computational modeling technique that inherently incorporates phenomena at the contact level as well as computational efficiency, specifically, the discrete element method (DEM).

Chapter 2: Mechanisms of Microcrack Formation during Unloading and Ejection

2.1 Introduction

The manufacture of solid or partially porous compacts by applying pressure to powders within a die typically has the result of producing compacts with low strength immediately after release from the die, and often defects in the form of cracks are present [13, 14, 111, 112]. When the compacts are used without further processing (e.g., sintering), they may not meet strength specifications due to the presence of the cracks. Even if their functionality is not affected, the presence of visible surface cracks may be an aesthetic issue that can compromise customer satisfaction, or might be considered an indication of a process which is not properly controlled. In either case, it is essential to minimize them if not eliminate them.

The understanding of the development of such cracks is at best incomplete. Early work provided intuitive suggestions that the origin of these cracks is related to the density variation of the compacts (Train, 1956) and the interaction of the radial wall stress with friction and the shape of the tooling during unloading and ejection (Long, 1960). Many authors have searched for correlations between process conditions and capping or lamination failures [23, 113-118]. The role of entrapped air has often been discussed, but it is clear that these defects are present even in the case of partial vacuum [23]. Practice has shown that the propensity for cracking in powder compacts becomes higher with increased pressure. A detailed physical mechanism consistent with the modern principles of fracture mechanics, which could lead to predictive capabilities, is not yet available.

The work presented in this thesis aims to propose such a mechanism. A motivation is offered by the work of Ashby et al. [119, 120] that describes the concept of wing cracks and the possibility for their extension under compressive fields. Results presented here show that

microcracking occurs in the die during unloading before ejection. Of these cracks, those that are on or close to the surface interact with the stress field that develops during the exit of the compact from the die and may lead to extension of the preexisting microcracks, or even to lamination. For reasons of simplicity, this work focuses on flat face compacts, effects related to entrapped gases or friction were not considered.

Powder compacts exhibiting predominantly brittle mechanical behavior are properly described by fracture mechanics [20, 121]. Much of the current understanding of fracture of these materials comes from the work on the mechanics of brittle fracture explained by Griffith [122] and Irwin [123]. For brittle solids, cracks are known to nucleate and propagate from defects, inherent to the material and associated with its composition and microstructure as it evolves during processing. When an external load is applied, cracks of favorable orientation may propagate and eventually lead to fracture. The crack propagation is driven by sufficient stored elastic strain energy in the vicinity of the crack tip that provides for the required dissipation energy for the creation of new surfaces, plastic dissipation around the crack tip, and other dissipation mechanisms:

$$G_{IC} = \frac{K_{IC}^2}{E} = \Delta\gamma_s + \gamma_p + \gamma_{other} \tag{2.1}$$

where G_{IC} is termed the critical energy release rate, E Young's modulus, $\Delta\gamma_s$ the work of adhesion, γ_p and γ_{other} the energy terms describing plastic dissipation and other energy dissipation mechanisms respectively, and K_{IC} the critical stress intensity factor or *fracture toughness* of the material. For brittle solids with limited plasticity ahead of an advancing crack tip, the fracture toughness of the material can be described by

$$K_{IC} = F\sigma\sqrt{\pi a_c} \tag{2.2}$$

where F is a geometric factor, σ the stress applied to the solid far from crack, and a_c the crack length. Therefore, understanding the fracture of any materials requires understanding of the nature of the cracks and the stress field that interacts with them. The overall stress conditions during the three stages of die compaction (compaction, unloading, and ejection) are shown schematically in Figure 2.1. During compaction (Figure 2.1(a)), the stress state is strongly triaxial and compressive with the radial stress lower than the axial stress. Retraction of one of the punches after the end of compaction transitions the stress state into biaxial compression radially, Figure 2.1(b). Assuming that (1) the stress is uniform at the end of compaction, (2) the material is linearly elastic during unloading, and (3) that the Young's modulus of the die is much larger than the one of the compact, then the residual wall stress can be calculated from the condition of no strain in the radial direction, $\Delta\varepsilon_{rr} = 0,$ as

$$\sigma_R = \sigma_{rr}^{\max} - \frac{\nu}{1-\nu}\sigma_{zz}^{\max} \tag{2.3}$$

where the *r* and *z* subscripts indicate the radial and axial directions and ν is Poisson's ratio of the material. The superscript max indicates values at maximum load. Typically this equation over-predicts the residual wall stresses in compacts after unloading. This over-prediction is associated with a clear and strong nonlinearity in the load-displacement curve [124]. This nonlinearity indicates that there may be inelastic phenomena that occurring during unloading, an idea that is

in line with some of the findings of this work. Finally, as the compact is ejected from the die, it expands radially by

$$\Delta\varepsilon_{rr} = \ln\left(\frac{D_{out}}{D_{die}}\right) = \frac{\sigma_{rr}^{R}\left(1-\nu\right)}{E} \tag{2.4}$$

This equation shows that the expansion from the die is inversely proportional to the Young's modulus and decreases with Poisson's ratio. When the compact is partially out of the die, the local stress field in the vicinity of the die exit is complex but can be analyzed numerically (Figure 2.1(c)). Local tensile stresses are expected on the surface of the compact that is out of the die with high shear stresses occurring at the exit. Biaxial compression stresses still exist in the part of the compact that is within the die. The combination of local tensile and shear stresses are expected to potentially cause fracture when the compact emerges from the die. Another mode of fracture can occur inside the die during unloading (Figure 2.1(b)) despite the compressive nature of the stresses.

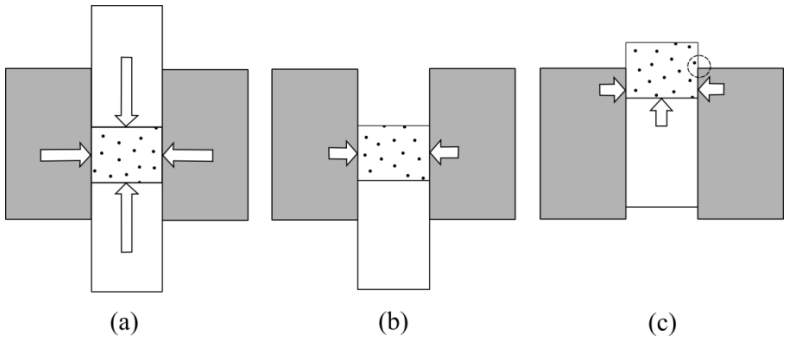

Figure 2.1 Overall stress states during the three stages of compaction: (a) compaction, (b) unloading and (c) ejection

Crack growth in brittle materials due to compressive stresses has been analyzed by Ashby et al. (e.g., [119]). In that work Ashby and co-workers considered the potential of fracture in brittle solids under compressive stresses using the theoretical concept of "wing cracks", which is schematically presented in Figure 2.2. While Ashby's work was primarily focused on ceramics and geological materials, the concept is also applicable to powder compacts. Of particular interest is the compact behavior under biaxial compression, which is the stress state after unloading in the die (Figure 2.2(b)). Using the idea from Ashby's work, it can be postulated that for the "right" combination of stresses and material properties, local microcracking in the compact may be possible upon unloading within the die. Although Ashby et al. predicted a lamination mode of failure (Figure 2.2(d)), their work considered the behavior of the material under a monotonically increasing load. In contrast, the formation of any cracks during unloading will relieve the stress that caused them rather than result in full lamination. Nevertheless, the formation of such microcracks may be the precursor to the onset of lamination and capping during ejection.

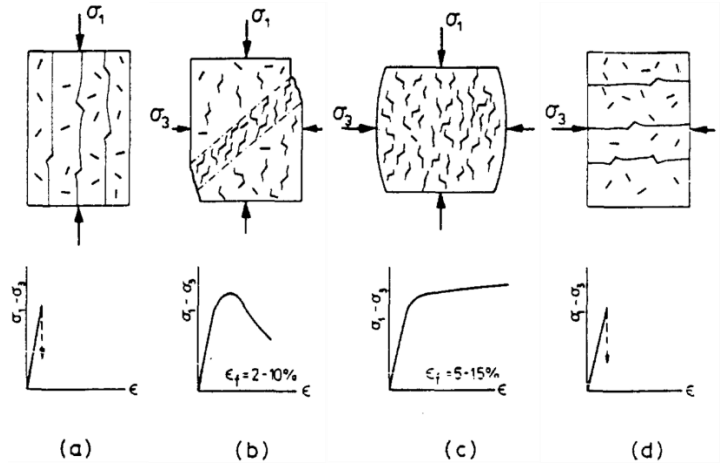

Figure 2.2 Crack growth in brittle solids under compressive stresses. Adapted from [119], where the presence of porosity was not considered.

2.2 Materials and Methods

In order to probe these ideas and delineate the mechanisms that lead to lamination and capping, a series of experiments was performed using straight and tapered dies, as explained below. The choice of the contrast between these two types of dies allowed the decoupling of ejection from compaction.

2.2.1 Materials

In order to study the differences in surface topography, internal structure, and mechanical properties between compacts produced in straight and tapered dies, the model material used was microcrystalline cellulose (MCC) (pharmaceutical grade Avicel PH102 from FMC Corporation, Newark DE). Microcrystalline cellulose was chosen as the model material because of the well-documented behavior of the material already present in the literature. Also, although this material does not cap or laminate, it develops cracking on its surface at high pressure. The MCC powder particles had a nominal size of 100 μm in diameter. In general, MCC powder has been reported as having an image-based particle size distribution of $D_{10} \approx 40$ μm, $D_{50} \approx 100$ μm, and $D_{90} \approx 200$ μm [125]. MCC can be described as a ductile material, which densifies primarily by plastic deformation at the interparticle contacts. This type of behavior is in contrast to other powders, which can be described as brittle and where densification occurs by fragmentation of the particles.

2.2.2 Die Compaction Experiments

Cylindrical compacts were produced using standard flat tooling and experimental data were obtained from compaction experiments using an Instron Universal model 5800R IUTM

(Norwood, MA). Die compaction experiments were performed using a Natoli (Saint Charles, MO) standard straight and standard tapered die with a nominal diameter of 9.525 mm for the straight die (Figure 2.3(a)), and a single-ended standard tapered die with a 10 mm nominal diameter in the cylindrical region and a taper angle of 0.56^{o} in the tapered region for the tapered die (Figure 2.3(b)). The tapered die, due to its geometry, was expected to allow for radial expansion of the compact within the tapered region. In this manner, the stresses in the vicinity of the die exit were minimized.

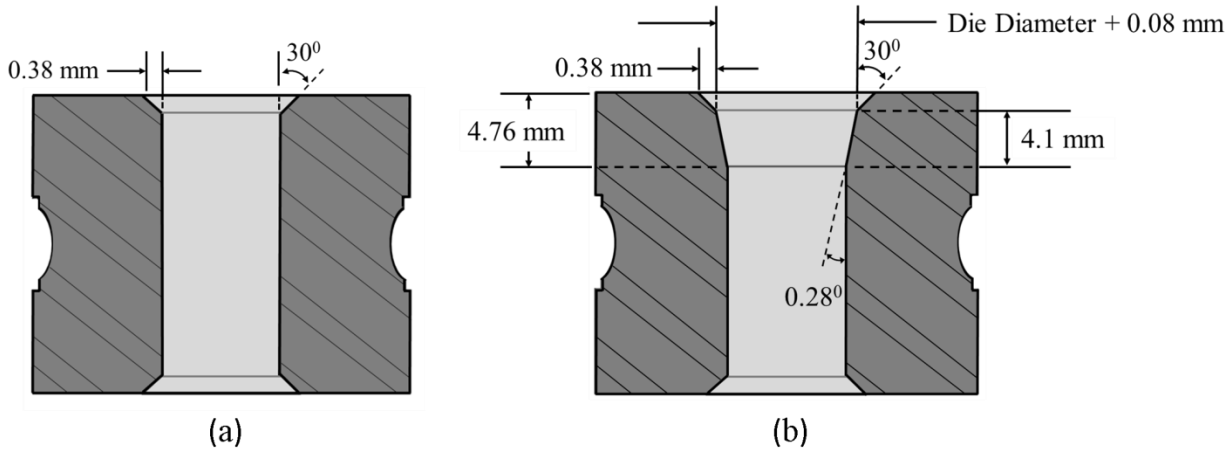

Figure 2.3 Geometries for (a) straight die and (b) tapered die with a taper angle of 0.56°. Geometries shown are not to scale.

Pressures in the range of 115—500 MPa were used to produce compacts with relative densities (RD) in the range of 85—95%, where RD is defined as the ratio of the measured density to theoretical density of the material. The theoretical density of MCC is 1.54 g/cm^3. The average bulk density at filling was 0.3 g/cm^3 for both straight and tapered dies. The die fill height in both types of compaction was 12.8 mm. The powder was compacted without internal or external lubrication using single action compaction, which involved only the motion of the top

punch during compaction. In tapered die compaction, the end of compaction took place in the cylindrical region and the final compact is ejected towards the tapered region. For the tapered die used here, the compact is allowed to expand in the tapered region of the die by as much as 0.8% before it reached the die/table surface in ejection. If the radial elastic recovery during ejection for a given material was smaller than this allowed expansion, the compact would unload fully within the tapered region. The expansion from die size for MCC compacts ranges from approximately 0.1—0.3%, which implied full unloading before the compact reaches the table/die surface [124]. In general, for small taper angles (tan $\theta \approx \theta$), the unloading strain in the tapered die region is given by

$$\Delta\varepsilon = \theta_{taper} \frac{H_{taper} - H_{compact}}{D} \tag{2.5}$$

for the top of the compact that ejects first, and

$$\Delta\varepsilon = \theta_{taper} \frac{H_{taper}}{D} \tag{2.6}$$

for the bottom of the compact, where θ_{taper} was the angle of the taper in radians, H_{taper} the depth of the tapered region (4.1 mm for standard tapered die), $H_{compact}$ the final height of the compact, and D the die diameter of the cylindrical region.

To avoid any possible effect from air entrapment, a slow compression/decompression rate of 0.2 mm/s with a dwell time of 3 seconds was selected. The rate of

compression/decompression is known to affect the mechanical strength of compacts [126-128] in which it has been found that generally an increase in compression/decompression rate may results in a decrease in strength [115]. While several factors may contribute to such rate dependence (friction, temperature, air entrapment), it is commonly suggested that increasing compression rate does not allow for air trapped from the interstices of compacted powder to escape, and results in higher incidences of capping failures [129]. Reugger and Celik [115] have shown that there is virtually no influence of compression/decompression rates on the mechanical strength of MCC for rates ranging from 50—300 mm/s and compaction pressures up 400 MPa, where above 400 MPa and rates of 300 mm/s, capping and lamination failures were observed for a fill depth of 15.6 mm and an estimated final height of 3.2 mm. For the results presented here, the compaction speed of 0.2 mm/s was several orders of magnitude below this threshold.

2.2.3 Micro-Computed Tomography

X-ray microtomography measurements were carried out using a Bruker MicroCT Skyscan 1172 (Kontich, Belgium) microcomputed tomography instrument (Figure 2.4). Microcomputed tomography (μCT) is an imaging technique in which x-ray projections recorded at different viewing angles are used to reconstruct the internal structure of all materials for non-destructive viewing [130-133].

Figure 2.4 Skyscan 1172 micro-CT

Microcomputed tomography scans were performed with a camera setting of 4000 X 2000 pixels and a resolution of ~2 µm per pixel. Scans of both straight and tapered die compacted MCC were performed on compacts having relative densities of 85 and 95%. For all scans performed, more than 1800 x-ray projections were collected. Post processing of the x-ray projections into 2- dimensional cross sections of the compacts was performed using the NRecon (Bruker-MicroCT) software package. To reduce the noise in the projections acquired during data acquisition, 4 frames were averaged together for each data acquisition step

2.2.4 Environmental Scanning Electron Microscopy

Environmental scanning electron microscopy (ESEM) was used to observe the surfaces of compacts produced in the straight and tapered dies. An environmental scanning electron microscope ESEM FEI, model XL30 (FEI, Hillsboro, Oregon), was used to compare the differences in the degree of diffuse surface microcracking between MCC compacts produced in the straight and tapered dies. The ESEM is a scanning electron microscope that allows the

acquisition of electron micrographs of samples that contain moisture by allowing a gaseous environment in the specimen chamber. The ESEM was chosen over traditional high-vacuum scanning electron microscopy to eliminate the effect of drying. For MCC under high vacuum, moisture is driven out of the sample, which may result in existing cracks propagating or initiating new ones [133]. All samples were imaged with an accelerating voltage of 20 kV in a gaseous environment (H_2O) and temperature of 20°C. At this temperature and pressure of ~400 Pa, the resulting relative humidity (RH) in the specimen chamber was ~55% RH, where relative humidity is defined as the ratio of the partial pressure of water vapor in air to the saturated vapor pressure of water at given temperature. While the exact RH above the specimen is not precisely known, it is definitely higher than those encountered in a traditional SEM where vacuum imposes practically 0% RH. To demonstrate whether or not the local RH in ESEM has an effect on crack size, the surface of a 95% RD compact was imaged over the period of two hours. Figure 2.5 shows ESEM micrographs of the region of the compact with the highest concentration of surface cracks acquired at the beginning and end of the experiment. Results of this experiment show that there is no effect of conditions used in the ESEM on crack opening size.

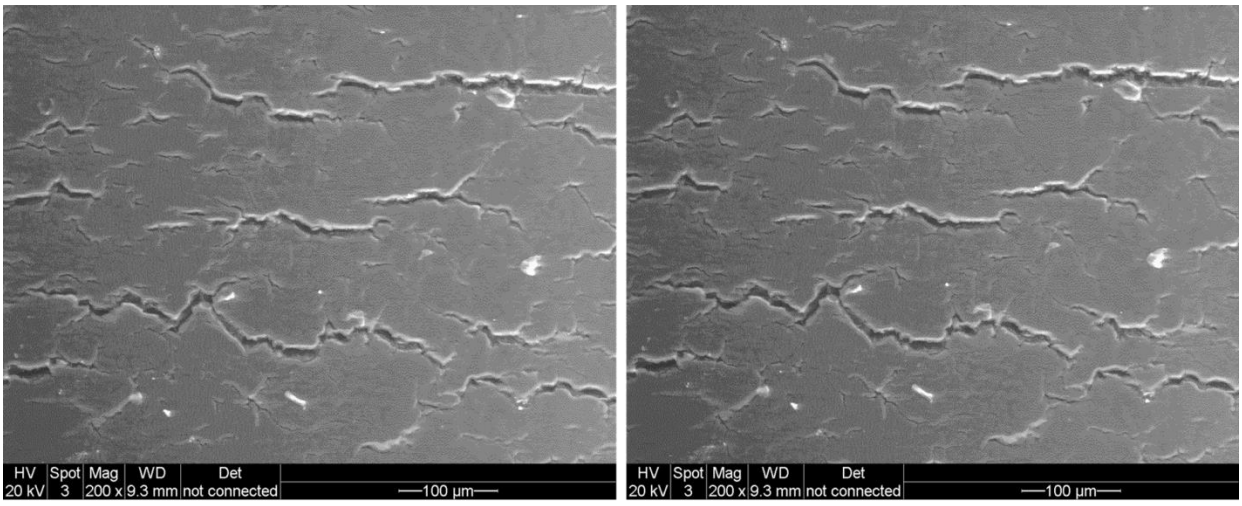

(a) (b)

Figure 2.5 ESEM micrograph images of a region of a 95% RD MCC compact containing high concentration of surface cracks acquired (a) at the beginning of experiment and (b) after two hours

2.2.5 Mechanical Testing

Diametral compression and uniaxial tension tests were conducted on compacts produced in straight and tapered dies. Both diametral compression and uniaxial tension tests were performed using a CT5 Engineering Systems mechanical testing machine (Nottingham, England). The diametral compression test is typical for pharmaceutical compacts and relies on the generation of a lateral tensile stress at the center of the sample to probe the tensile strength of the material [134, 135]. Compact breaking forces were measured for each relative density compact at a test speed of 0.02 mm/s and the diametral tensile strengths were calculated by

$$\sigma_T = \frac{2P_f}{\pi Dt} \tag{2.7}$$

where P_f is the load at failure, D is the diameter of the specimens, and t is the measured compact thickness.

In addition to diametral compression, axial tension tests were employed in a similar fashion to the testing procedure employed by Nystrom et al. 1977 [136] and more recently for bilayer compacts by Akseli et al. [137]. The purpose is to probe the effect of hoop cracks which would not affect the results of diametral tests. Compacts were attached to two removable metal stubs using a cyanoacrylate adhesive as shown in Figure 2.6. The compacts were placed on to the stubs so that the top of the compact (next to the movable punch in compaction) is placed on the top movable platen of the testing device. While the adhesive was still uncured the removable metal stubs were fastened to upper and lower platens by tightening set-screws against the insertable pins of the stubs. The presence of uncured adhesive at this stage allowed for realignment of the compact with the stubs without the creation of additional stress. The compacts were kept under a small compressive stress of approximately 65 kPa during curing of the adhesive to establish good adhesion between the compact and metal stub surfaces. To keep the stubs firmly attached to the upper and lower platens during loading, it was necessary to machine a groove in the stub pins for the insertion of the set-screws to give additional support. A constant displacement between the top and bottom metal stubs was employed at a rate of 0.4 mm/s until failure. All samples were observed to have failed by catastrophic brittle fracture. The majority of compacts were observed to have fractured close to the top or bottom metal stub resulting in a layer thickness of approximately 0.3—0.75 mm of the thinner layer. For compacts with RD equal to 95%, the majority of compacts were observed to have fractured towards the top

stub; whereas, compacts with RD equal to 85% showed no preference towards fracturing towards the top or bottom stub. The apparent axial strengths of compacts were calculated as

$$\sigma_A = \frac{P_f}{A} \tag{2.8}$$

where P_f is the peak load at failure and A is the cross sectional area of the specimens. It is important to note that this test is not particularly suited for obtaining absolute values of axial strength because the constraint from the stubs and the difference of their elastic properties from those of the compact affects the stress state in the sample. Here, the results of this test are used on a comparative basis for specimens of the same material with identical internal structure (see discussion below) and will reflect in an objective manner the difference of the samples surfaces.

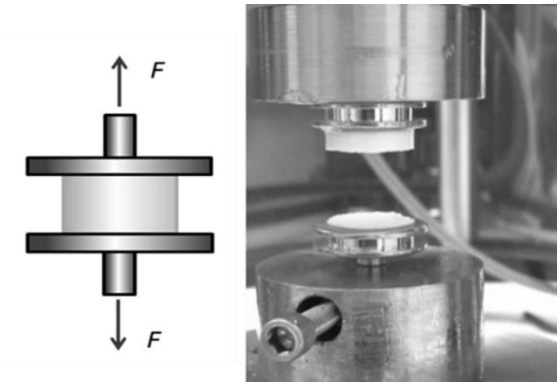

Figure 2.6 Modified axial tensile test

2.3 Numerical Modeling

The finite element method was used to simulate the differences in the compaction behavior between straight and tapered die compaction. Simulations performed in this study primarily focused on the ejection stage of the compaction process. To model the differences between straight and tapered die compaction, simulations were performed using the commercial finite element package ABAQUS [138] in which the Drucker- Prager Cap (DPC) [36] model was employed.

The DPC model parameters (cohesion, internal friction angle, evolution parameter, cap eccentricity, and hydrostatic yield stress), as well as Young's modulus, Poisson's ratio, and die-wall coefficient of friction were identified for microcrystalline cellulose (Avicel PH102) using a series of experiments based on the procedure explained in [27]. The geometries of the powder and punches were modeled after flat-faced cylindrical shaped compacts. The geometries of the straight and tapered die walls used in FEM simulation are shown in Figure 2.3. Axisymmetric conditions effectively reduce the problem to 2-D. Figure 2.7 shows a typical discretized geometry used in the compaction simulation at the beginning and end of compaction for the straight die compaction simulation. This geometry and mesh configuration is identical for simulations involving tapered die compaction with the exception of the die wall. The punches and die walls were modeled as analytical rigid surfaces. To simulate the compaction stage, the rigid surface representing the lower punch was held stationary while the upper punch was displaced downward by a specified distance. Since the numerical simulations were primarily focused on the comparison of the local stresses between straight and tapered compacts at the radial edge during the ejection stage, a high density mesh with a concentration of elements towards the radial edge was used. The mesh defining the compact consists of 24,000

axisymmetric 4-node bilinear elements with 200 elements along the radial edge and 120 elements along the top and bottom biased towards the edge of the compact.

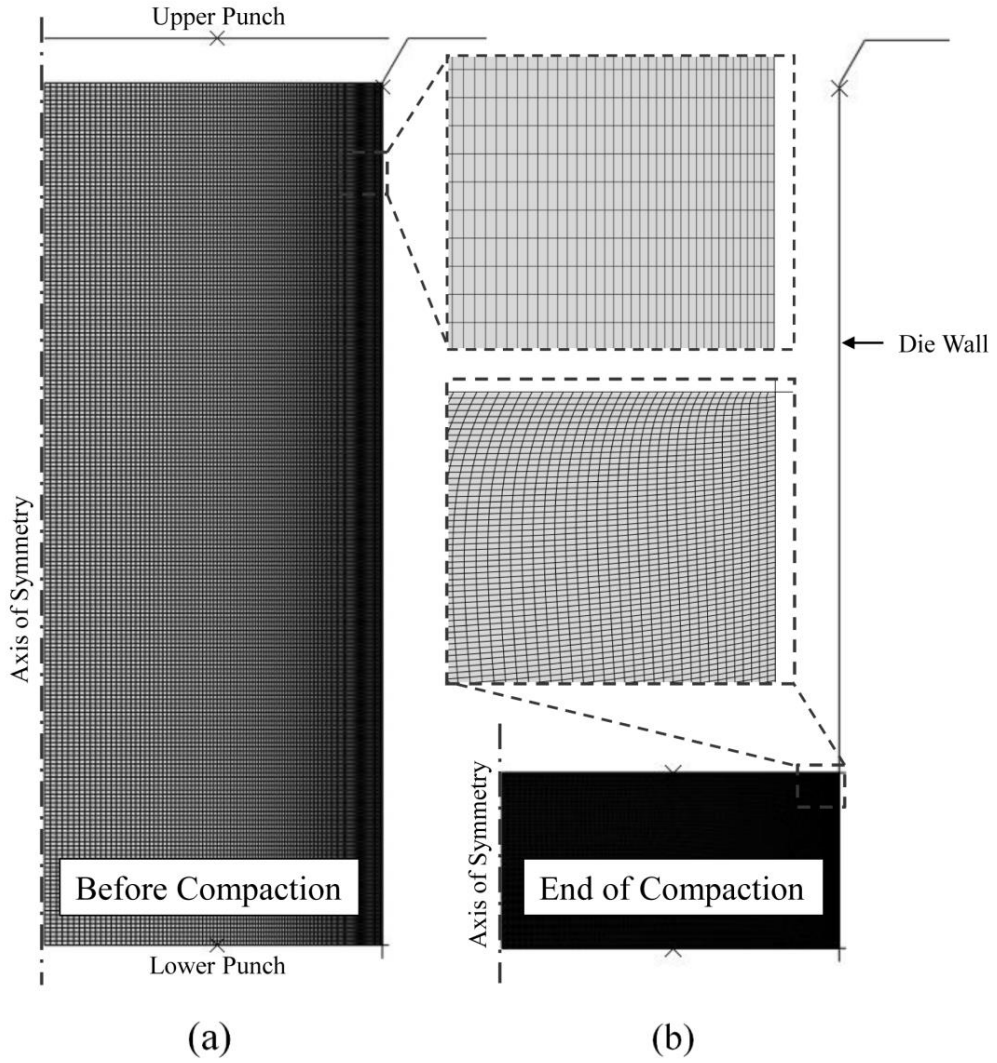

Figure 2.7 Finite element meshes used for both straight and tapered die simulations involving the implementation of the DPC model showing (a) mesh before compaction and (b) mesh at the end of compaction.

An important consideration in FEM simulations involving the DPC model is the de*via*tion between FEM prediction and experimentally measured values of residual wall stress, σ_R. Figure 2.8 shows the maximum wall stress at the end of compaction predicted by FEM simulation compared to experimentally recorded wall stress for MCC in straight die compaction. From this figure, it is shown that there is good numerical agreement with experiment. However, once complete unloading occurs, the DPC model overpredicts the residual wall stress. Figure 2.9 shows the comparison of residual wall stresses that remain after unloading predicted from FE analysis, as well as recorded residual wall stresses from experiment as a function of the maximum compaction pressure for MCC. This implies that a physical mechanism that relieves the radial stress that relieves the radial stress exists and is not captured by elastic unloading.

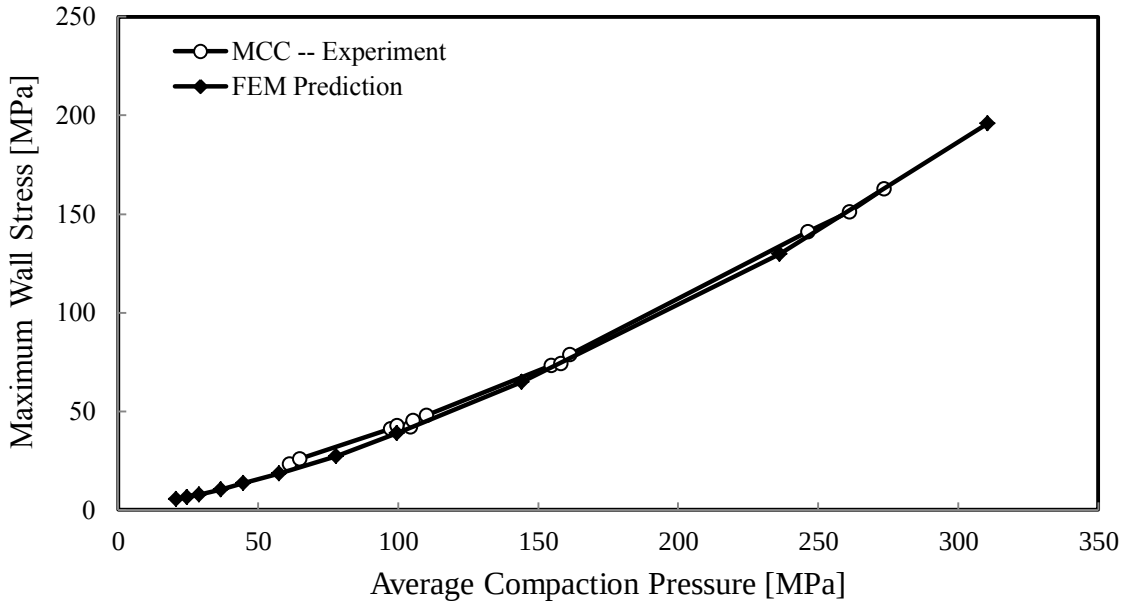

Figure 2.8 Comparison of maximum wall stress predicted from FE analysis involving the implementation of the DPC model and recorded from straight die compaction experiments.

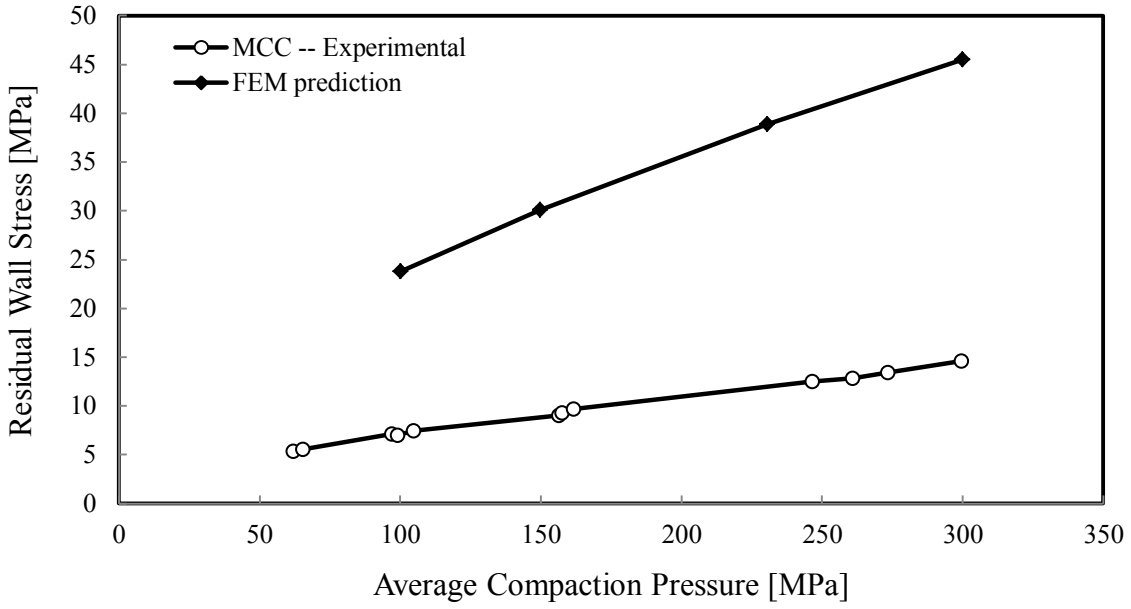

Figure 2.9 Comparison of residual wall stress predicted from FE analysis involving the implementation of the DPC model and recorded from straight die compaction experiments.

2.4 Experimental Results

2.4.1 Internal Structure and Surface of Straight and Tapered Die Compacts

Figure 2.10 and 16 present the x-ray tomography results of the internal structure of compacts compacted at 95% and 86% RD respectively. Both compacts produced from straight and tapered dies have internal defects in the form of partially closed pores and microcracks. Qualitatively, the microstructures of the compacts compacted to the same RD in the two types of dies are identical. A large number of microcracks are present throughout the 95% *RD* compacts. They are oriented perpendicular to the prior compaction direction for both straight and tapered die compacted compacts are evident. These cracks are of the order of 50 µm in the plane and their opening is of the order of 4-6 µm. At 86% RD, microcracking is difficult to observe,

possibly because the crack openings are smaller than those of the higher density specimens and become comparable or smaller than the resolution of the technique. Pores in the 86% *RD* compacts are larger than those of the 95% RD, as expected.

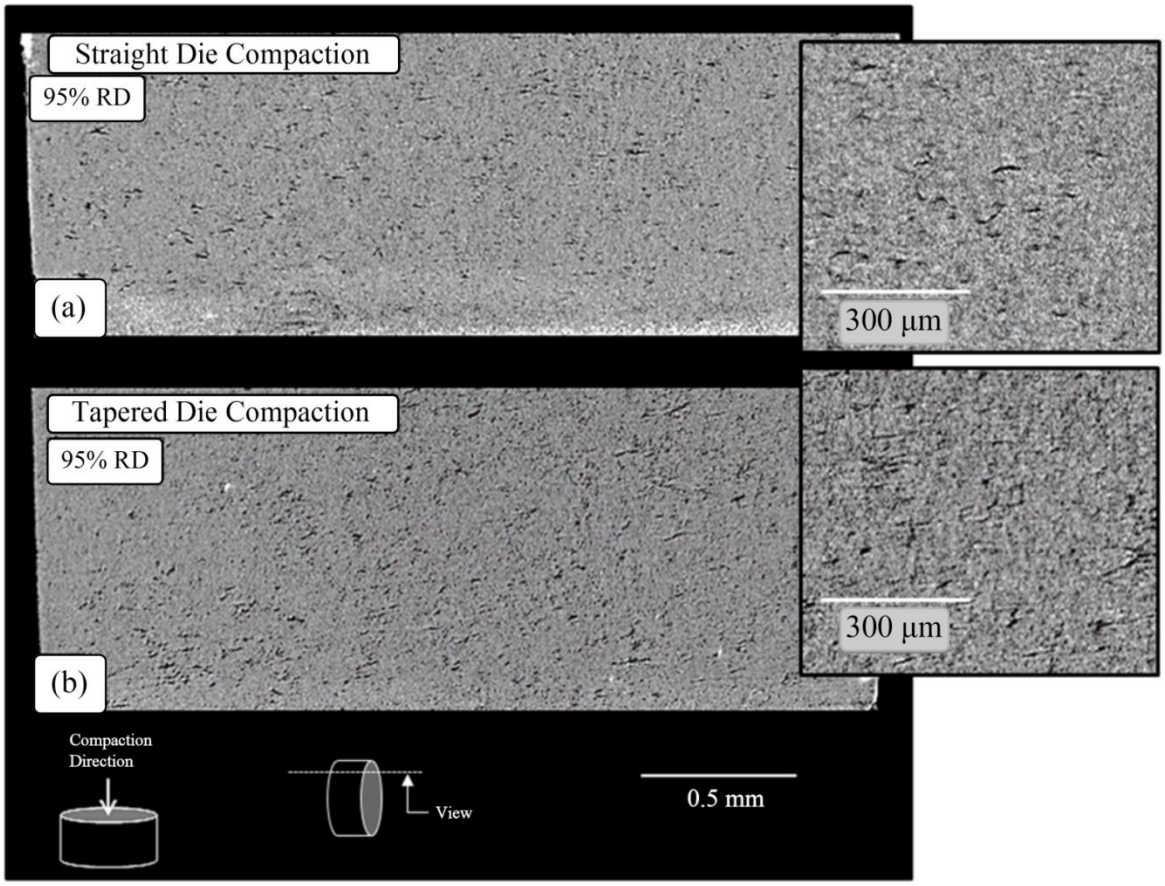

Figure 2.10 Internal structure of (a) straight die compacted microcrystalline cellulose, and (b) tapered die compacted microcrystalline cellulose compacted to approximately 95% RD. The viewing slice is approximately 0.8 mm from the edge of the compact.

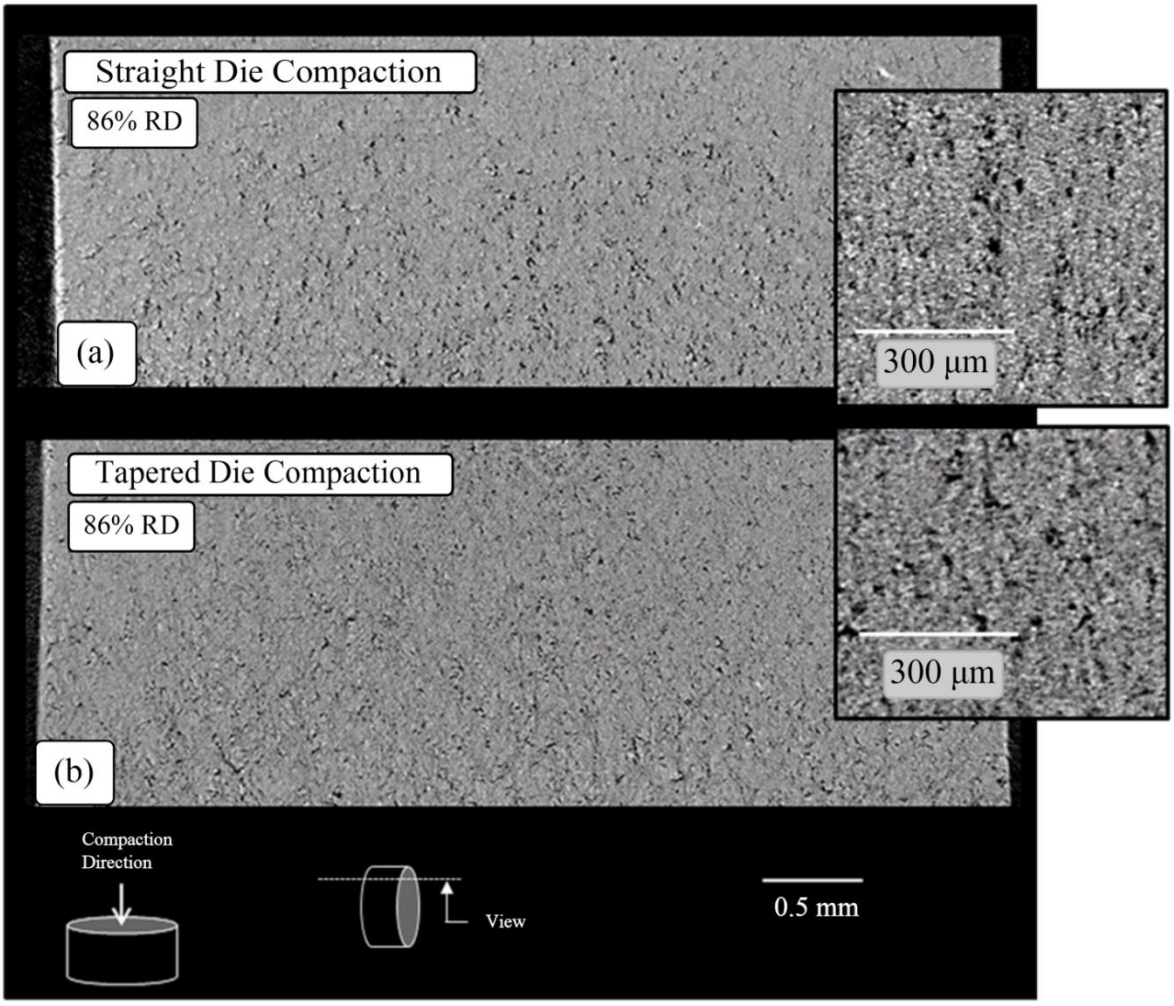

Figure 2.11 Internal structure of (a) straight die compacted microcrystalline cellulose, and (b) tapered die compacted microcrystalline cellulose compacted to approximately 86% RD. The viewing slice is approximately 0.7 mm from the edge of the compact

Figure 2.12 and Figure 2.13 show the structure of 95% and 86% *RD* compacts just below the surface of the compacts. Similar to the internal structure, the surfaces possess diffuse surface microcracking that extends in the direction perpendicular to the prior compaction direction. The compact compacted in the straight die has both larger crack openings and larger crack lengths. This distinction is clear for the higher density compacts. The majority of the larger cracks

appear in the upper part of the compact close to the moving punch. Fewer cracks were observed on the surface of compacts compacted to final relative densities below 86%.

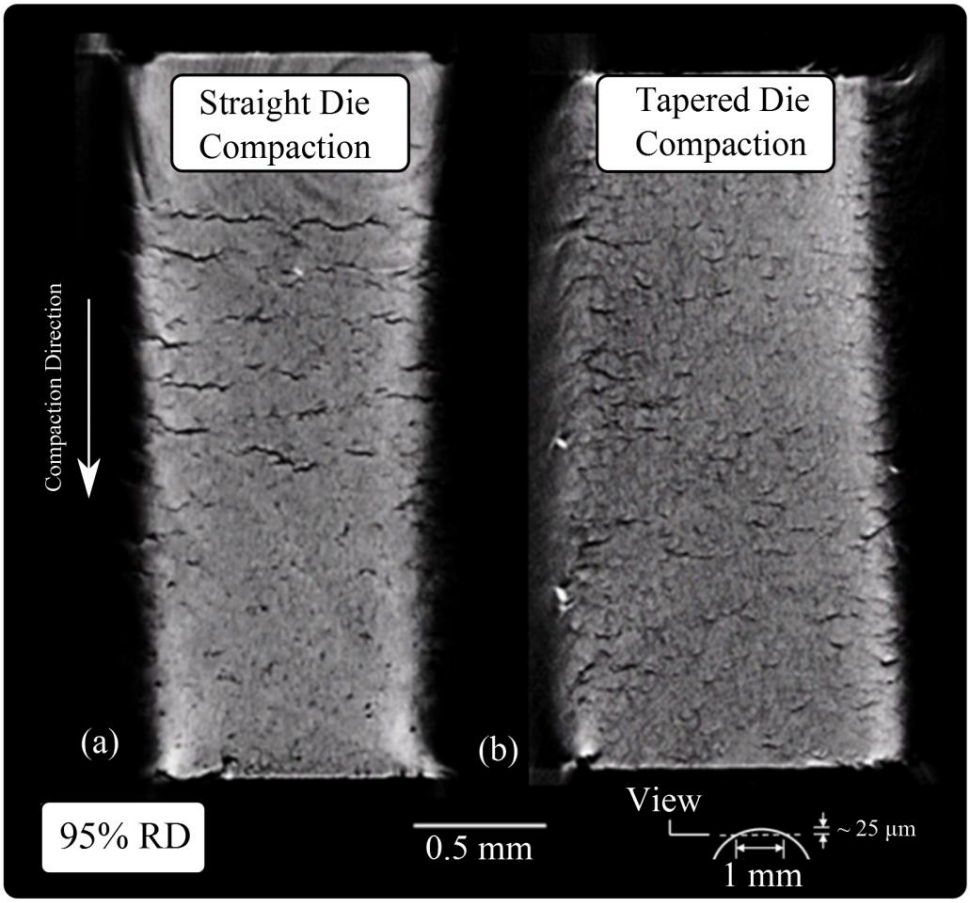

Figure 2.12 X-ray tomographic images of the surfaces of (a) straight die compacted microcrystalline cellulose and, (b) tapered die compacted microcrystalline cellulose compacted to approximately 95% RD.

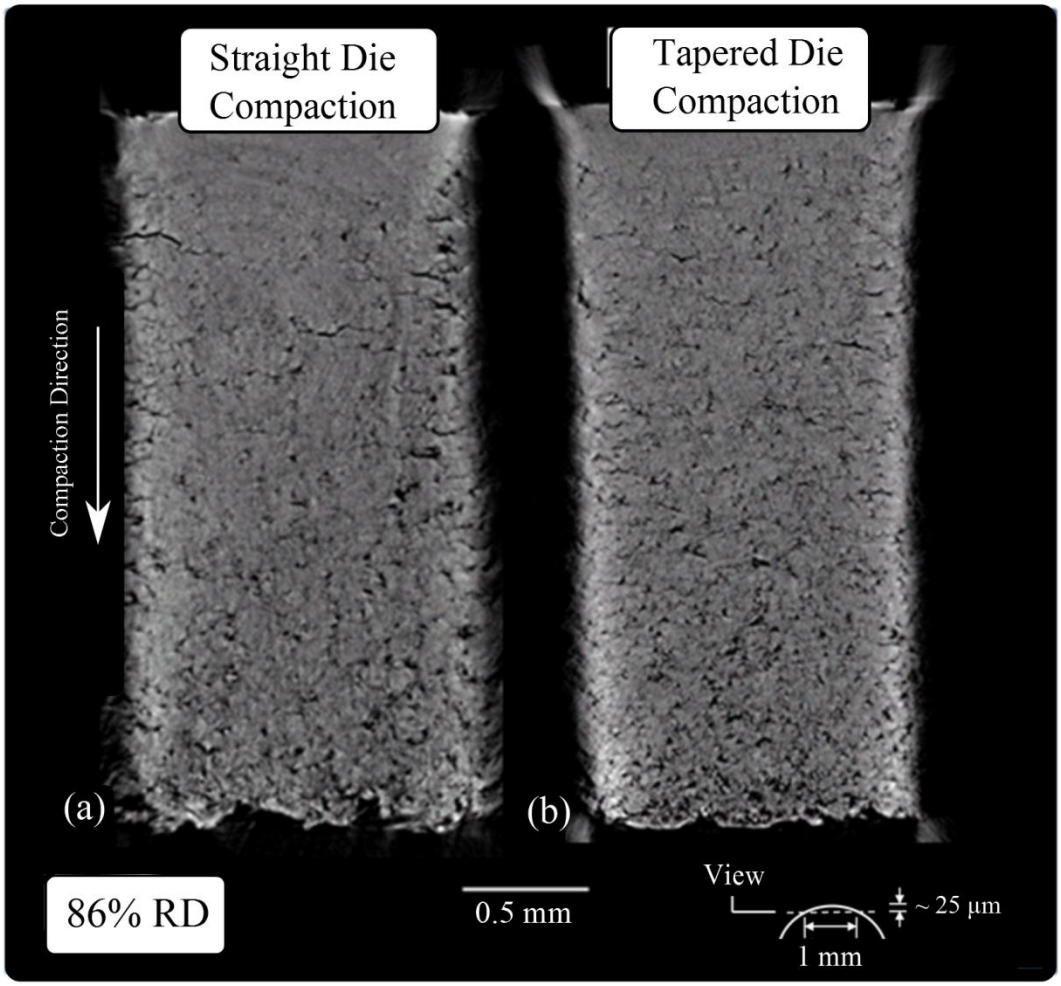

Figure 2.13 X-ray tomographic images of the surfaces of (a) straight die compacted microcrystalline cellulose and, (b) tapered die compacted microcrystalline cellulose compacted to approximately 86% RD.

To reinforce the results from microtomography as well as to characterize the crack opening more accurately, the external surfaces of the compacts were examined in an environmental scanning electron microscopy (ESEM). This technique has a much higher resolution than μCT and allows for observation of cracks with opening smaller than the resolution of μCT. Figure 2.14 shows ESEM micrographs of straight and tapered die compacted compacts compacted to relative densities of 95% and 86% RD. Both compacts at 95% exhibit

diffuse surface microcracking consistent with the results of microtomography. Horizontal cracks appear through the side surface of both compacts from straight or tapered dies. A narrow 400 μm zone free of cracks appears at the bottom of the compact (close to the stationary punch). Also, a narrow zone (~ 200 μm) of crack free surface exists at the top of the compact from the tapered die. The most important difference between compacts produced from the two types of dies is the presence of several larger in size and opening cracks on the side of the compact from the straight die, three of which can be seen in Figure 2.14(a). The pores on the surface of the 95% RD compact are practically all closed while in 86% relative density compacts pores of a few-micron-size can be easily observed. The surfaces of the 86% are dominated by porosity. Pores of the order of 5 μm are present of the surfaces of the compacts as expected. Close examination of Figure 2.14(b) shows the presence of cracks on the straight die compact in the same location as in the 95% RD compacts.

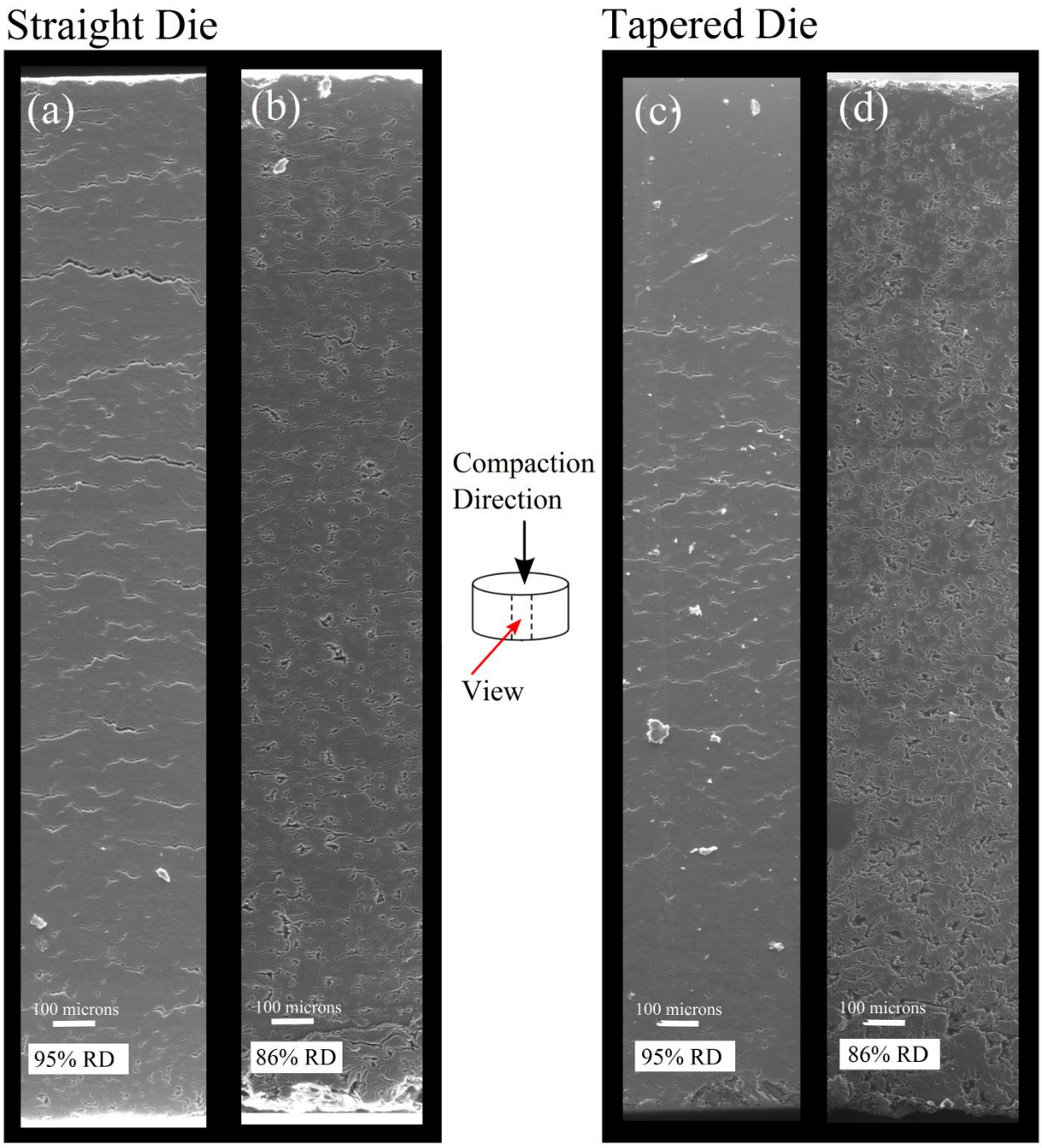

Figure 2.14 Environmental scanning electron micrographs of surface profiles for microcrystalline cellulose compacted in straight and tapered dies and compacted to approximately 95% and 86% RD.

Differences in size and distribution of surface microcracking between compacts produced in the straight and tapered die were quantified by the linear intercept method, which is a technique commonly used to quantify the grain or grain size in crystalline materials [139]. To implement this technique, five line segments extending in the direction parallel to the compaction direction were placed at equal distances apart on ESEM micrographs of 95% RD compacts. The number of times that each line segment intersected a crack, as well as the corresponding crack opening length, was recorded. An example of this method can be seen in Figure 2.15 for the straight die case. Figure 2.16 shows the frequency of the crack opening lengths for the 95% RD straight and tapered die compacted micrographs. At small crack opening lengths, the distributions for the two types of compact are practically identical but the tapered die compact contains no crack opening lengths above 5 μm. The presence of several large cracks in the straight die compact is expected to have an effect on its strength (in the axial direction).

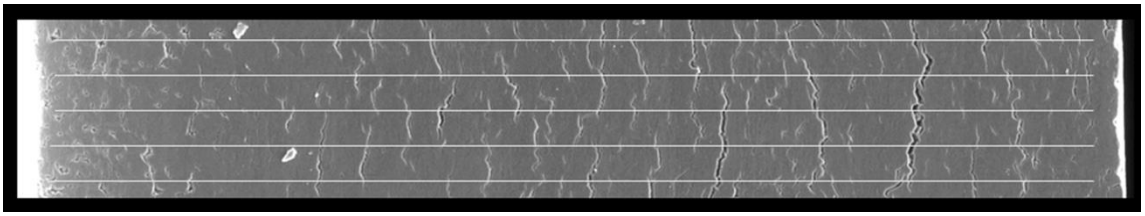

Figure 2.15 Environmental scanning electron micrograph shows line segment placement for use in the line intercept method.

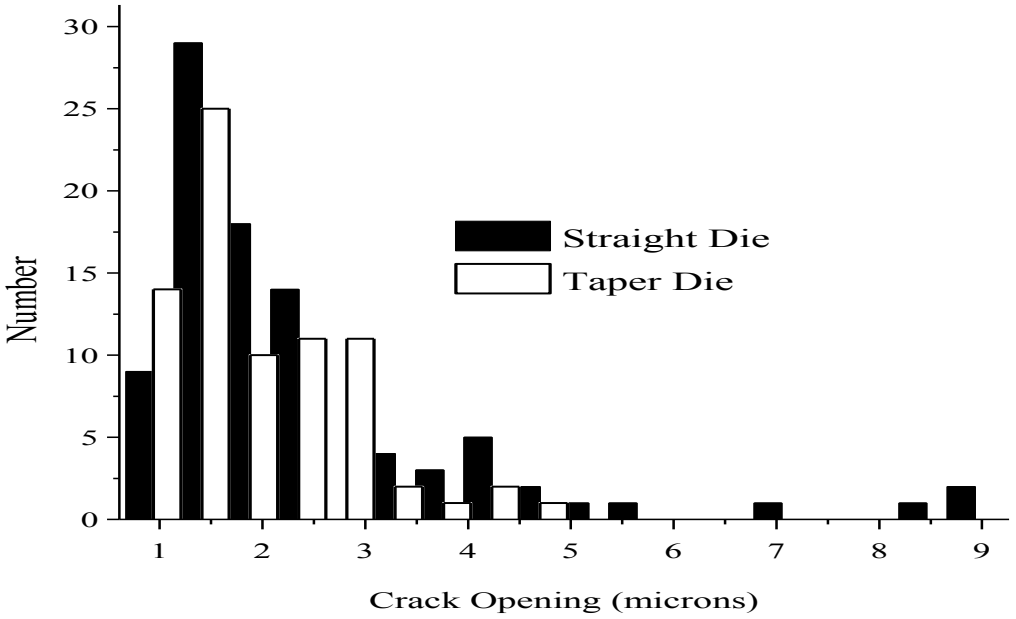

Figure 2.16 Distribution of crack opening lengths for MCC compacted to 95% RD in straight and tapered die. The linear intercept method was used on micrographs shown in Figure 13.

An attempt was made to quantify the spatial distribution of the cracks. The surface was segmented into 8 equally sized zones along the compact. Zone 1 is close to the bottom of the compact (stationary punch), whereas zone 8 is at the top of the compact (moving punch). A crack was counted as a single crack if it could clearly be determined that its extension could be distinguished from surrounding cracks and the crack opening was not closed at any point within the crack extension. Judgment was needed in order to distinguish pores from cracks, which was especially true for zone 1 where porosity is greatest. Figure 2.17 shows that overall the cracks are distributed over the length of the compacts with more cracks close to the center. The distribution of the cracks in the tapered die compacts is broader, while there is a short area close to the top of the tapered die compact that is free of cracks.

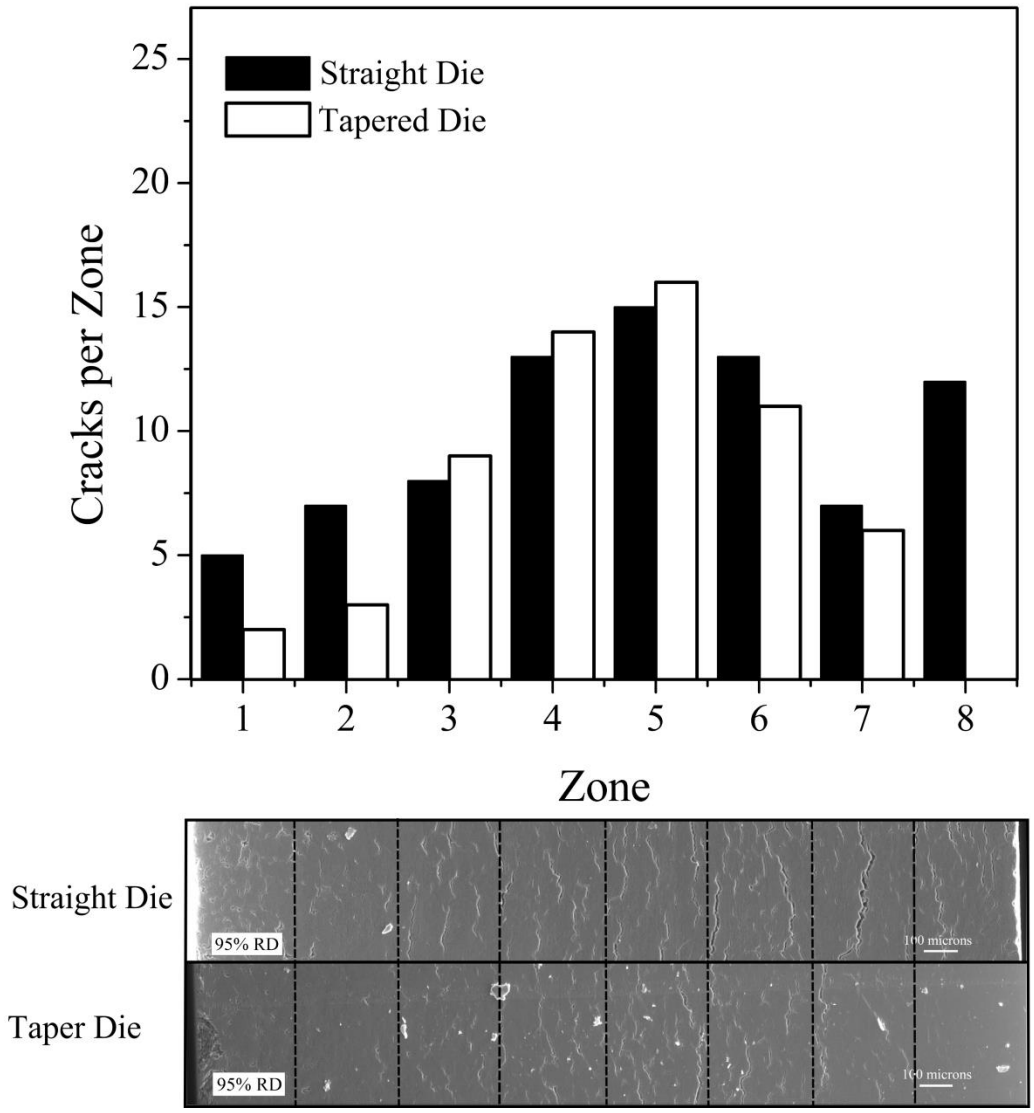

Figure 2.17 The number of cracks per zone, where 1 zone represents 1/8 of the surface profile in the micrograph. Zone 1 represents the region that makes up the bottom of the compact and zone 8 represents the top.

2.4.2 Axial Tension and Diametral Compression Tests

Figure 2.18 shows results of diametral compression for compacts produced from the two types of dies. The difference in the strengths between the two types is marginal with measured values falling within one standard error at each relative density. Therefore, the two types of compacts can be considered to exhibit practically identical diametral strengths. As seen above, the differences between the two types of compacts are the cracks present on their surface. Given that their orientation is along the loading direction in diametral compression and far away from the area where fracture is initiated (close to the center of the compact), they do not affect the diametral compression results.

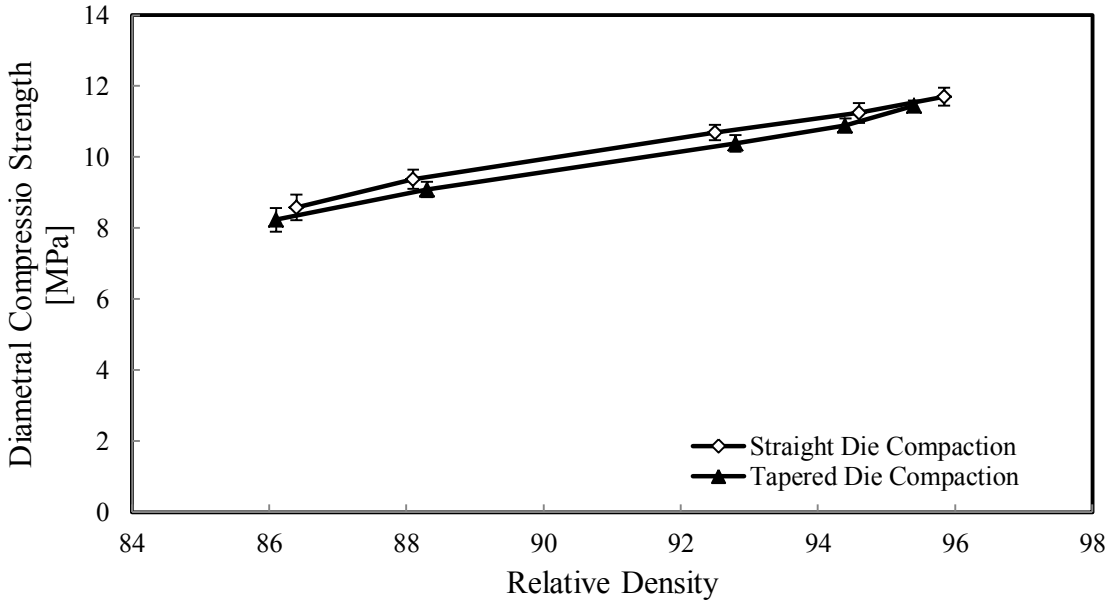

Figure 2.18 Mean diametral compression strength and standard error as a function of RD for microcrystalline cellulose compacted in straight and tapered dies. The mean and standard error were determined from 10 measurements per relative density for each compaction type.

The observed cracks on the surface of the compacts are expected to have a direct effect on their axial strength. Testing along this direction is not common because the small aspect ratio of the specimen requires that the compacts are glued to tabs for tension. The axial strength obtained in this way is difficult to interpret, primarily due to uncertainties in the local stresses imposed by the gripping of the specimens. e.g., the local stress state can de*via*te from tension when the specimens are glued to tabs, and the material mismatch between the tabs and the compact imposes stresses lateral to the direction of loading. Even so, a comparison between compacts from same material compacted in straight and tapered dies at the same density is still meaningful. Given that all other results (microtomography and diametral compaction) verify that the internal structure is identical, any difference in the response in axial tension will reflect the condition of the surface and the cracks on it. Figure 2.19 shows axial strength measurements for straight and tapered die compacts using a modified mechanical testing setup as discussed previously. All compacts tested demonstrated fast, brittle failure. Tapered die compacts consistently produced higher strengths at high densities, but the difference diminishes at densities lower than 85%. These results are consistent with the fact that at higher densities compacts produced in straight dies exhibit larger circumferential cracks than the corresponding ones from tapered dies. The results also demonstrate that diametral compression does not provide a full insight into the strength of the compacts.

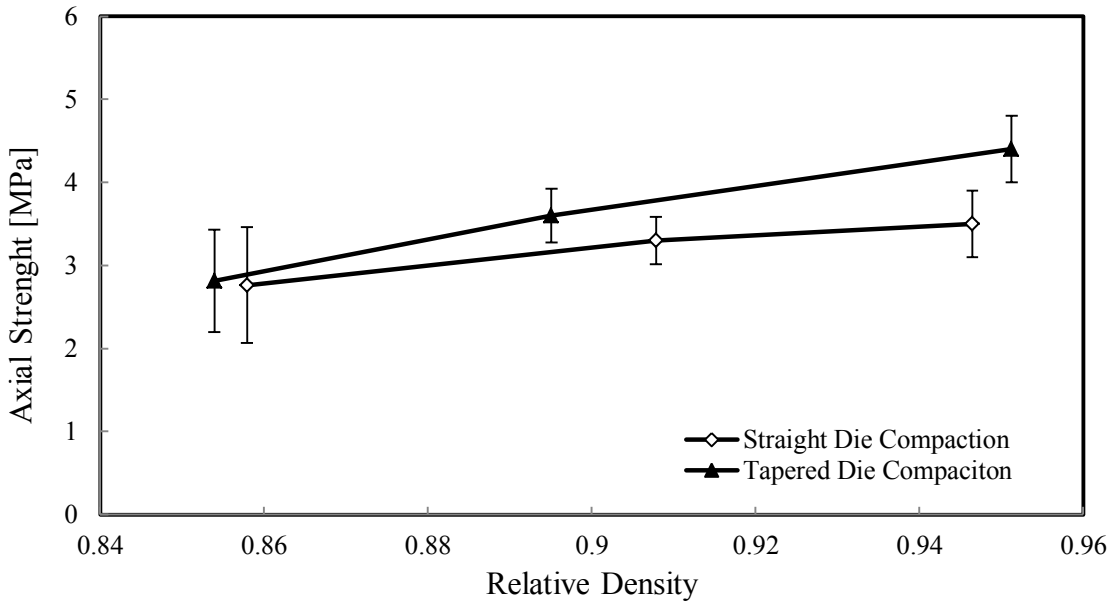

Figure 2.19 Mean axial strength and standard error as a function of RD for microcrystalline cellulose compacted in straight and tapered dies. The mean and standard error were determined from 10 measurements at RD ≈ 0.95 and 0.90 and 8 measurements for RD ≈ 0.85 for each compaction type.

2.5 Numerical Results

The experimental results presented above can be rationalized by studying the mechanical state of the compacts as they exit from the die. Compacts produced in straight and tapered die compaction were also compared using an FEM analysis. The compaction conditions for each case were identical. The predicted density distribution at the end of compaction is presented in Figure 2.20 and shows that there is no difference in terms of local density between compacts produced by the straight and tapered dies. For the results shown in Figure 2.20, a die fill of 12.8 mm and a minimum punch separation of 2.6 mm were used. Experimentally, these compaction conditions produce an out-of-die relative density of approximately 95%. Experimental results

presented in Figure 2.21 show that the average compaction pressure-density relation in both dies is practically identical, and is also confirmed by the simulation that show a difference less than 0.5% for all densities.

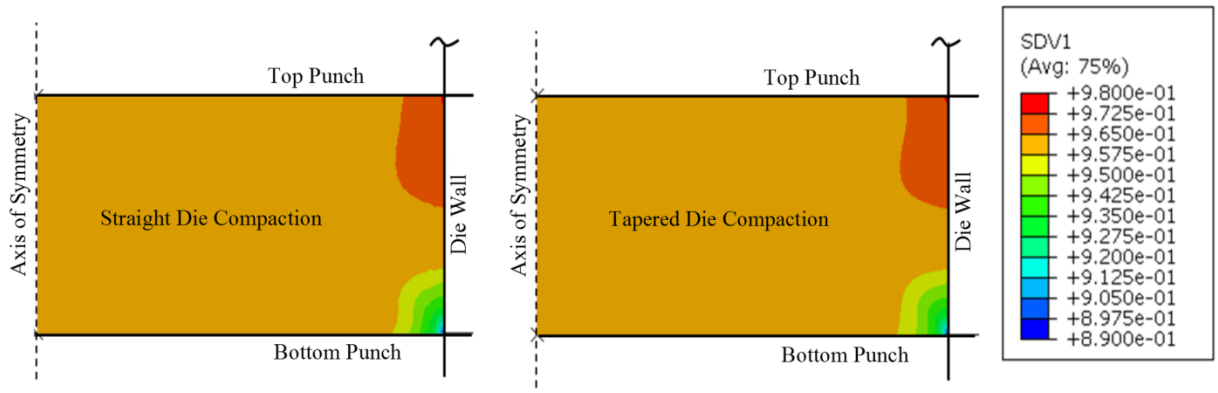

Figure 2.20 FEM prediction of relative density distribution at the end of compaction for straight and tapered die compaction. SDV1 represents relative density.

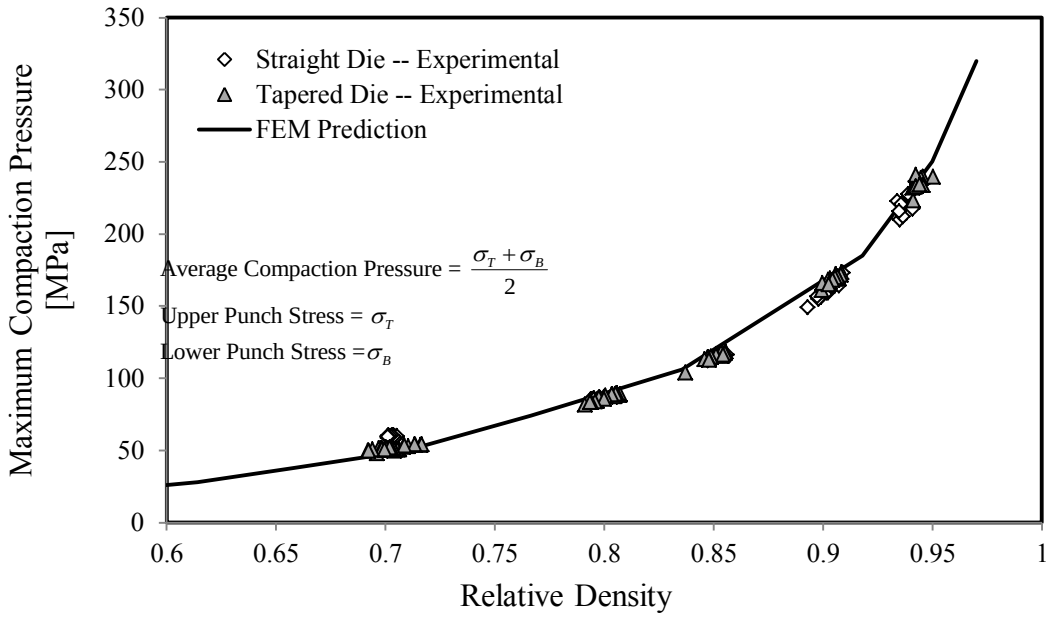

Figure 2.21 Average compaction pressure-density relation of straight and tapered die compaction and the corresponding FEM prediction

Attention was focused on the mechanical stresses in the compact when the compact is partially ejected a specified distance past the die exit. For the tapered die, the die exit is defined as the point at which the die taper meets the die bore (point 2 in Figure 2.22(b)) and is referred to as the start of taper. For the straight compact, the exit is considered to be the point at which the die bore meets the exit chamfer (point 1 in Figure 2.22(a)). Figure 2.22 shows the distribution of stresses in the y direction with an emphasis on tensile stresses for compacts partially ejected approximately 0.6 mm past the die exit and start of taper for the straight and tapered compact respectively. It is important to note that the partial ejection distance of 0.6 mm was simply chosen for comparison purposes only. Any other partial ejection distance produces a similar comparison of the results. A distinct difference between straight and tapered die compacts is observed close to the radial surface of the compacts. The simulation shows the presence of high intensity tensile stresses after the exit of the compact in the straight die (Figure 2.22(a)); whereas the tensile stresses in the tapered compact occur at a location beyond the start of taper and are reduced (Figure 2.22 (b)). Figure 2.22(c) shows that within the straight die there is an intense increase of the compressive stress close to the surface of the die, while immediately after the exit from the die there is a reversal of the sign of the stress, becoming tensile. The tapered die compact shows a noticeable transition from the compressive regime to tensile regime past the start of taper with stresses lower than the partially ejected straight die compact. For the tapered die compact, this transition indicates that the part of the compact is still in contact with the die wall past the start of the taper.

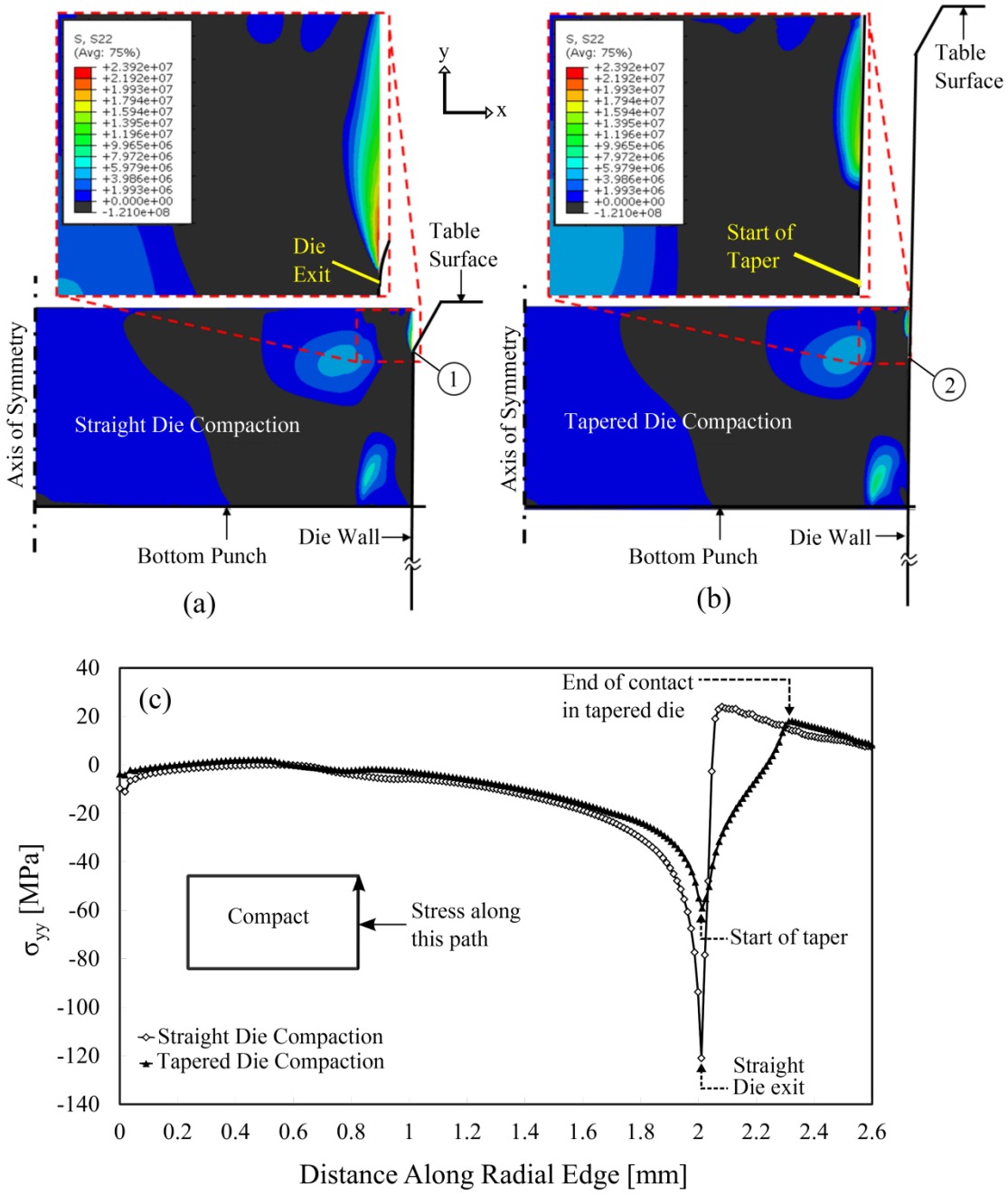

Figure 2.22 Contours of σ_{yy} within the compacts during partial ejection from a straight die ejected ~ 0.6 mm past the die exit (point 1) (a) and a tapered die ejected ~ 0.6 mm past the start of the taper (point 2) (b). The graph in (c) shows the variation of the stresses in the y direction along the outer edge of the compact.

Figure 2.23 shows the distribution of shear stresses for compacts ejected to the same locations shown in Figure 2.22(a & b). A marked difference is observed in the local shear stress close to the edge of the compacts for the two compaction types. For the straight die simulation, there is an excessive intensity in the shear stresses observed towards the radial edge of the compact (Figure 2.23(a)), which is virtually non-existent in the tapered compact (Figure 2.23(b)). From Figure 2.23(a), it is shown that immediately above and below the die exit there is a change in shear direction, which indicates the presence of a singularity. Figure 2.23(c) confirms the presence of this singularity around the exit from the straight die with only a more gradual change in shear stresses for the tapered die around the start of the taper, where this figure shows the shear stress distribution along the radial edge of the two compaction types.

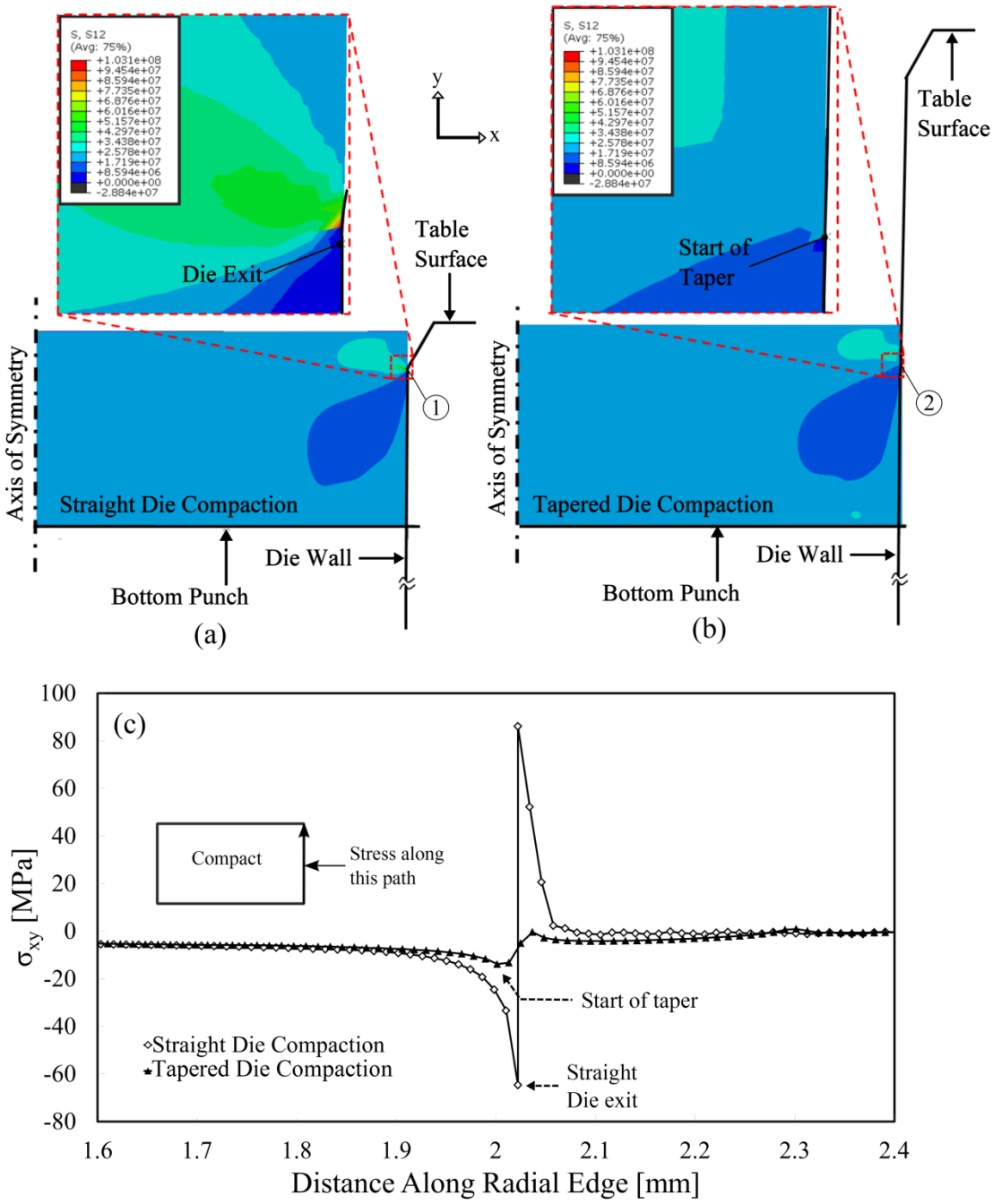

Figure 2.23 Contours of shear stress within the compacts during partial ejection from a straight (a) and a tapered die (b). The graph in (c) shows the variation of the shear stresses along the outer edge of the compact.

It is instructive to focus on the details of the stress field around the exit point of the straight die. Before the exit from the die (point A in Figure 2.24), the stress state in the material is highly compressive in the radial direction within a very narrow area from the surface. This point is surrounded by two highly shearing areas (B and C in Figure 2.24). The area of the surface of the material just outside the die (marked D in Figure 2.24) is under uniaxial tensile stress. Most importantly, the area of the surface immediately beyond the die exit (marked E in Figure 2.24) is under a state of intense shear. It is important to note that a point just below this point of intense shear, the state of stress is similar with a change of sign in the shear direction. As the material attempts to expand elastically, it is constrained by the part of the compact that is still inside the die. The stresses at points D and E are imposing a mixed mode I and II loading mode on the surface of the compact and tends to open the cracks that formed during unloading. It is important to note that the level of stresses shown in Figure 2.24 is exaggerated from the fact that the DCP model used in the FEM simulation does not include the relaxation of the radial stresses due to microcracking that is experimentally observed (see Figure 2.9). Nevertheless, the qualitative features of the prediction are still valid. It is also important to note that qualitative features in Figure 2.24 also hold for the tapered die that is ejected to a location partly beyond the start of the taper with the exception of shear stresses, which are significantly reduced.

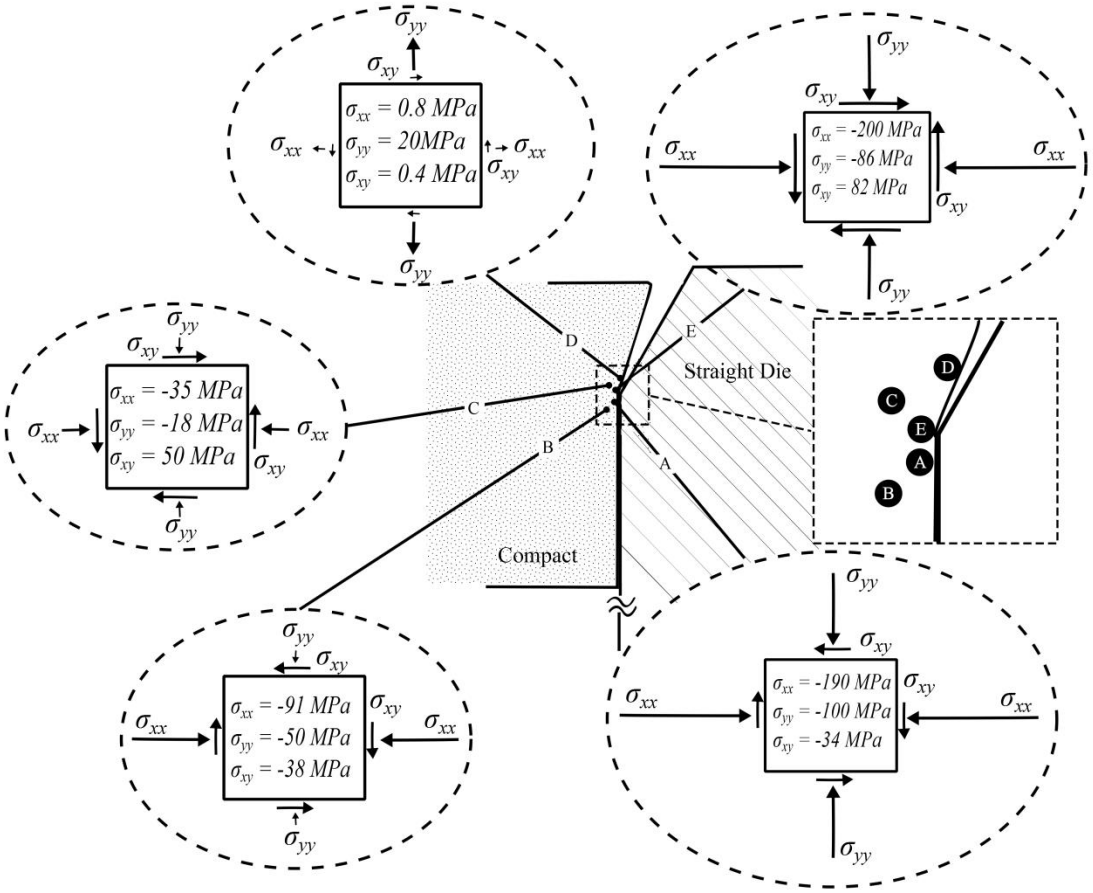

Figure 2.24 Stress field around the exit point of straight die obtained *via* compaction simulation

2.6 Discussion

The results presented above provide a clear picture of the mechanisms of crack formation in compacts during unloading and ejection from the die. Theoretically, microcracks can develop either at unloading or during ejection when the compact is in the die or when the compact emerges from the die. The presence of the cracks within the body of the compact (microtomography results from Figure 2.10) eliminates the possibility that the cracks form during ejection when the compact is in the die, because during this stage any action is limited on

the compact surface due to friction. Similarly, the effect of the interaction of the compact with the edge of the die as it exits should also be localized on the surface—as supported by the FEM results. More intense surface cracks were observed in the straight die compact than in the tapered die compacts, where the shape of the die allows for complete unloading before the compact exits from the die. This thinking process establishes unambiguously that microcracks develop through the body of the compacts during unloading, and may grow further when the compact emerges from the die. The theoretical assertion of Ashby et al. [119, 120], that biaxial compression of a brittle material will generate microcracks oriented in the plane of the compression, is in line with our experimental observations. The difference between what Ashby et al. [119, 120] claimed and the case in hand is that they considered the response of materials under monotonically increasing load, while here the biaxial stress occurs as a result of the changing stress state from the highly triaxial compression at the end of compaction to the biaxial stressing (radial pressing) at the end of unloading. During this transition, the radial stress is continuously decreasing as shown in the radial versus axial stress curve during compaction and unloading shown in Figure 2.25(a). The high stress triaxiality of the stress field during compaction closes the pores and does not create any damage in the microstructure. During unloading, when the axial stress becomes sufficiently low, the formation of the cracks commences. It is suspected that the initiation of the microcracking is demarcated by the deviation from linearity in the radial versus axial stress diagram and the axial stress versus relative density in Figure 2.25(b). During the initial stage of unloading the compact behaves as a linear elastic material, but the initiation of the microcracks relieves the radial wall stress near the last half of unloading. This is consistent with the significant deviation between FEM predicted and experimentally measured values of radial wall stresses shown in Figure 2.9.

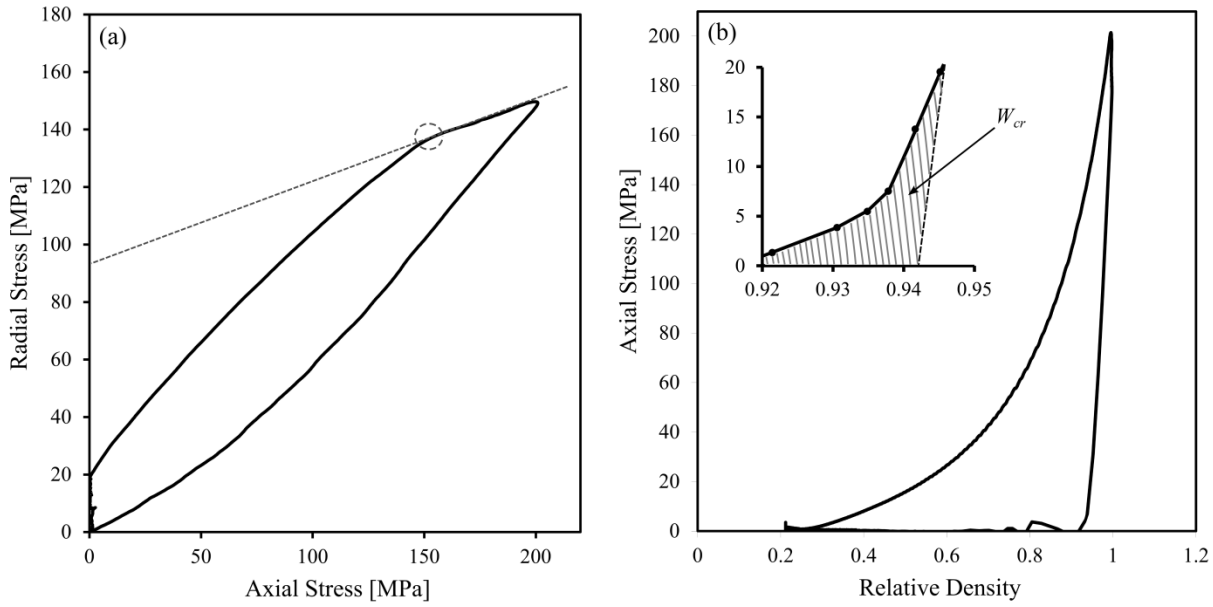

Figure 2.25 Compaction experiments highlighting nonlinearities in the curves for (a) radial versus axial stress and (b) axial stress versus relative density for MCC.

The nonlinearity observed in both the radial versus axial stress and axial stress versus relative density graphs in Figure 2.25 provides an indication of the extent of cracking during unloading. The deviation from linearity (highlighted area in Figure 2.25(b)) indicates to some extent the amount of work that is spent to create the cracks. Although a detailed analysis of the phenomenon is lacking, the generation of microcracking during unloading depends on the maximum radial wall stress, the elastic properties that determine the stress history during unloading and the fracture toughness of the materials, which evolves during compaction. Finally it is noted that the presence of these horizontal microcracks fully justifies the observed strength anisotropy in this material (see [20]), with the axial strength being lower than the radial strength due to the preferred orientation of the cracks.

Regarding the crack growth that occurs when the compact exits from the die, the numerical analysis provides insight regarding the local conditions that cause it. As discussed

previously, surface microcracks generated during unloading grow at the exit from the die due to shear stresses in a mode II or due to tensile stresses along the surface of the compact due to the elastic expansion of the compact upon exiting the die points (D & E in Figure 2.24). The utilization of a tapered die significantly reduces the detrimental effect of the exit of the die by minimizing the level of shear and tensile stresses in the tapered region. Therefore optimization of the die exit can be beneficial for the mechanical properties of the compacts post ejection. An indirect indication of this possibility is discussed in the field of coal compaction [140]. It has been shown that the generation of coal fines or dust from handling – an indication of the strength of the coal briquettes - depends strongly on the die design at the exit. In general, generous fillet radii or even tapered shaping of the exit can reduce the amount of damage on the surface of the compacts and the associated reduction of mechanical properties in the axial direction. A gentle taper along the whole length of the die may be the optimal geometry to avoid the associated level of damage on the surface typically observed in straight die compacts by reducing the level of tensile and shear stresses. At this point there are no general guidelines for the optimum tapering angle, other than the fact that the amount of taper should ideally allow for near complete unloading of the compact within the die. One drawback in this approach is that that there may be a large tolerance between the die and the upper (moving) punch, a situation that can create a fragile "lip" at the edge of the upper face of the compact, and also the opportunity for binding of the material between the punch and die, increasing tooling wear.

Some key points emerge from this discussion. First, the strength of a compact in biaxial compression is clearly emerging as an important parameter that needs to be studied and quantified. Second, there are specific aspects of the unloading sequence that if altered can lead to compacts with fewer defects. In addition to the effect of tapered dies that is discussed here

extensively, the concept of triaxial unloading proposed by Heckel [83] for producing intact compacts essentially is a process that avoids biaxial compression, but is not practical for production.

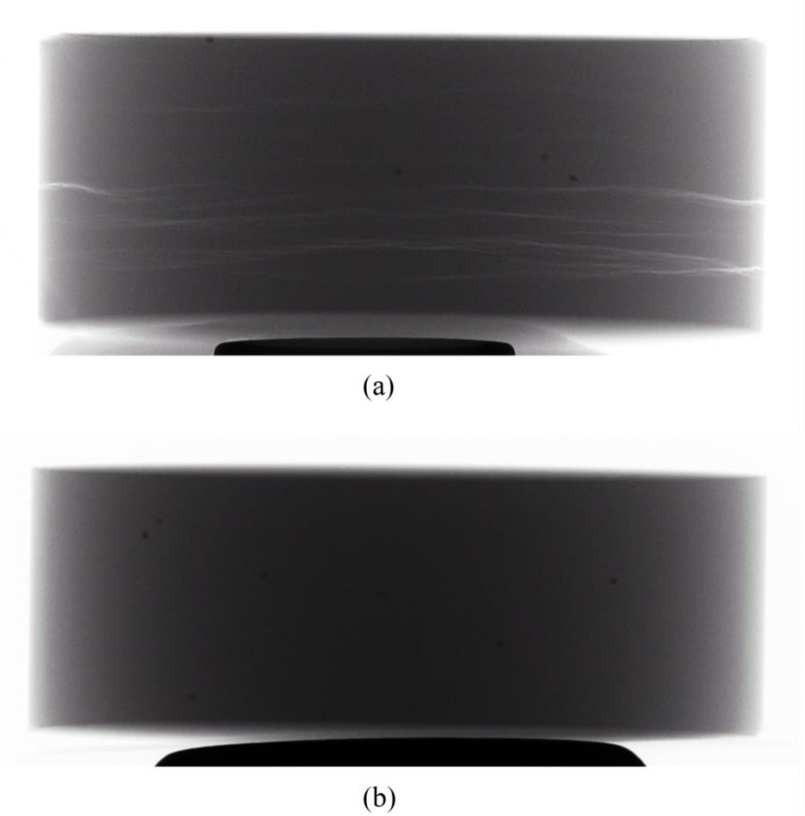

Figure 2.26 X-ray back shadows of sodium chloride compacted by (a) straight die compaction and (b) tapered die compaction.

For materials with lower fracture toughness than microcrystalline cellulose, the interaction of the die exit with the material can lead to even larger cracks and possibly full lamination. Therefore, the use of a tapered die, which essentially minimizes the interaction of the die edge with the expanding compact, can help to minimize damage and possibly prevent capping and lamination failures. An example of this can be seen in Figure 2.26, which shows

the x-ray projections of sodium chloride compacts in straight and tapered dies (Figure 2.26(a) and (b) respectfully. Ideally, the selection of the tapering angle in the tapered dies would be such that it matches a significant percent of the expansion of the compact from the die size. For materials with even lower fracture toughness, it is possible that the unloading process can lead not just to diffuse microcracking as seen here, but also to in-die lamination. These results should translate to powder systems where the primary densification mechanism is plastic deformation of the particle. For systems where densification is achieved *via* fragmentation, aspects of the stress considerations related to the exit are expected to be similar, but microcracking in unloading needs further investigation.

2.7 Conclusions

It has been shown by a combination of experimental and numerical methods that diffuse microcracking develops in MCC compacts upon removal of the axial load within the die. Some of these diffuse microcracks growth to larger sizes under the action of stresses that develop when the compact is about to exit from a straight die. The reason for these stresses is the elastic unloading of the compact after exit from the die. In microcrystalline cellulose, the development of cracks relieves the elastic strain from the partial unloading of the compact and as a result, the crack growth is terminated. In order for the phenomenon to repeat, sufficient volume of the compact needs to emerge from the die. This behavior gives rise to a repeated pattern of laminations cracks. For other materials large amounts of elastic energy stored in compaction and low fracture toughness may lead to complete lamination of the compact. On the contrary, MCC compacts that were compressed and ejected from a tapered die are essentially unloaded in die. The results presented here establish that in die microcracking and further crack extension during

the emerging of compacts from the die lead to defects such as surface cracks and lamination. The work presented here provides the basis for understanding the process and the mechanisms for damage and defect formation in powder compacts.

Chapter 3: Modeling Die Compaction of Powders and the Resulting Strength of Ejected Compacts using the Discrete Element Method

3.1 Introduction

The goals of this work were to (a) take the first steps towards a contact model that could approximate the behavior of powder particles subjected to compressive and tensile forces in high relative density simulations of die compaction, and (b) develop a methodology to easily calibrate the parameters of the proposed contact model from macroscale experiments performed on a real powder system. The key assumption in the formulation of the adhesive, elastoplastic contact model was that a unique force-displacement behavior that uses a heuristic approach to the effect of influencing neighboring contacts in loading could be used to adequately model the die compaction of particles. This assumption was a compromise between describing a more realistic behavior at the contact by explicitly incorporating the influence from neighboring contacts into the model and the desire to produce a contact model for particles subjected to high confining conditions (i.e., high stress triaxiality) without the need to alter the conventional DEM approach to contact force calculations. Thus, a proposed adhesive, elastoplastic contact model was developed with the intent of better predicting the behavior of powders compacted to high densities while remaining straightforward, accessible, and practical for use in terms computational cost.

3.2 Formulation of an Adhesive, Elastoplastic Normal Contact Model

Typical contact behavior for the elastoplastic loading and unloading of a contact in a monosized spherical assembly of particles subjected to isostatic compaction is shown in Figure

3.1. The interparticle contact response shown in this figure was obtained from an axisymmetric finite element analysis of a regular array of monosized spherical particles with a coordination number of $Z = 8$ isostatically pressed to high density. The axisymmetric finite element analysis employed was identical to the FEM implementation performed by Tsigginos et al. [62] for the contact on a spherical particle with coordination numbers equal to $Z = 6$, 8, 10, and 12 (see Chapter 1, section 1.2). As such, details of the FEM analysis are not addressed here. While the importance of the coordination number and its effect on forces generated at a contact cannot be understated, the work presented here was merely meant to obtain the generic form of the force-displacement behavior for the purpose of producing a general adhesive, elastoplastic normal contact model that possesses this generic form. Thus, only a contact on a spherical particle with a coordination number $Z = 8$ was considered.

From the FEM analysis shown in Figure 3.1 for a cohesionless contact belonging to a particle with a coordination number $Z = 8$ it was revealed that the normalized force-displacement behavior ($f/(\sigma_y R^2)$ versus δ/R) resulted in a nearly linear response for a normalized deformation up to $\delta/R \approx 0.11$ for the $Z = 8$ isostatic compaction, where f, σ_y, R, and δ, are the normal contact fore, yield strength, particle radii, and contact deformation respectively. This nearly linear type of force-displacement behavior is in-line with the similarity solution developed by Storåkers et al. [60]. However, a large deviation from linearity is observed for normalized deformations greater than $\delta/R \approx 0.11$. The deviation from linearity in the contact force-displacement behavior has been determined to be associated with constraints imposed to the particle-particle contact by neighboring contacts [53, 55, 62, 64]. Observation of Figure 3.1 shows that force increases significantly for deformations greater than $\delta/R \approx 0.11$, which signifies an increase of the stiffness, k, at the contact. The large increase in force and the corresponding increase in stiffness

at the contact was the result of the decrease in plastic flow of material able to fill the available void space between contacts with increasing deformation.

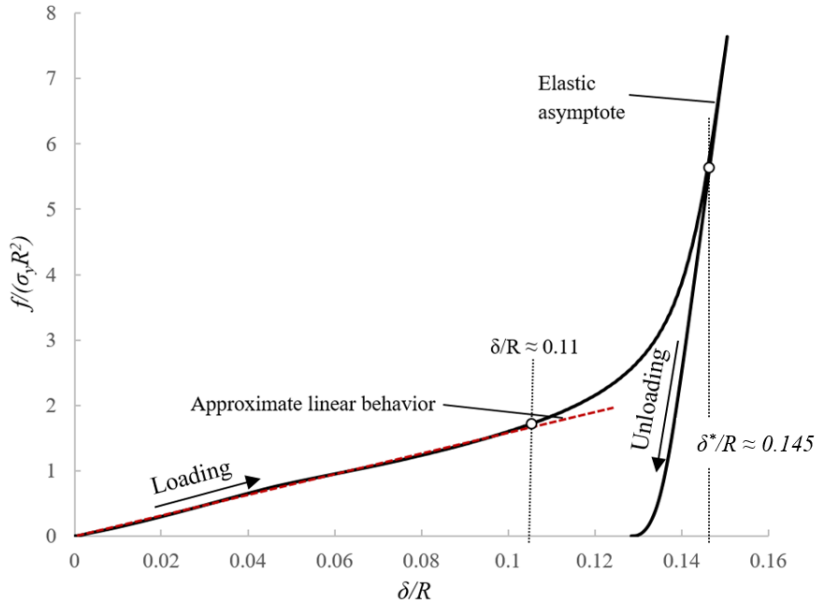

Figure 3.1 FEM result for the cohesionless normalized contact force-displacement behavior of a contact on a particle with a coordination number $Z = 8$.

At an approximate normalized critical deformation of $\delta^*/R \approx 0.145$ and beyond (see Figure 3.1), the force-displacement behavior again displayed a linear response, which indicated that compaction in this stage was dominated by elastic volume reduction of the particle. The onset of this elastically dominated stage of deformation was due to the nearly full closure of the pores and the subsequent diminishing ability of the particles to undergo any further plastic deformation [62, 64]. In Figure 3.1, an oblique asymptote in the force-displacement behavior was observed for the elastically dominated stage of the compaction and is denoted by "elastic asymptote". This observation was also realized in the work performed by Frenning [63, 64] for

the isostatic compaction of monosized spherical particles. Unloading of the contact from the elastically dominated stage shown in Figure 3.1 also revealed the asymptotic behavior for the beginning stages of unloading, which further demonstrated the asymptotic behavior.

Figure 3.2(a) shows the normalized force-displacement behavior for unloading from varying levels of maximum deformation. The slopes of the unloading curves presented in Figure 3.2(a) clearly shows a change in slope from a relatively low slope at smaller deformations to a maximum slope given by the elastic asymptote at the normalized deformation corresponding to the elastically dominated stage of the compression. Figure 3.2(b) shows the normalized unloading stiffness for varying levels of normalized maximum deformations, δ_{max} / R, where δ_{max} represents the maximum deformation achieved prior to unloading for the different unloading curves. The unloading contact stiffness were obtained by taking the slope of the unloading curves at the beginning stage of unloading, as schematically depicted in the inset of Figure 3.2(b). The unloading stiffness was reasonably approximated by a linear increase in unloading stiffness with increasing contact deformation, an assumption considered by Luding [105] in his adhesive, elastoplastic normal contact model (see Chapter 1, section 1.4.1.1).

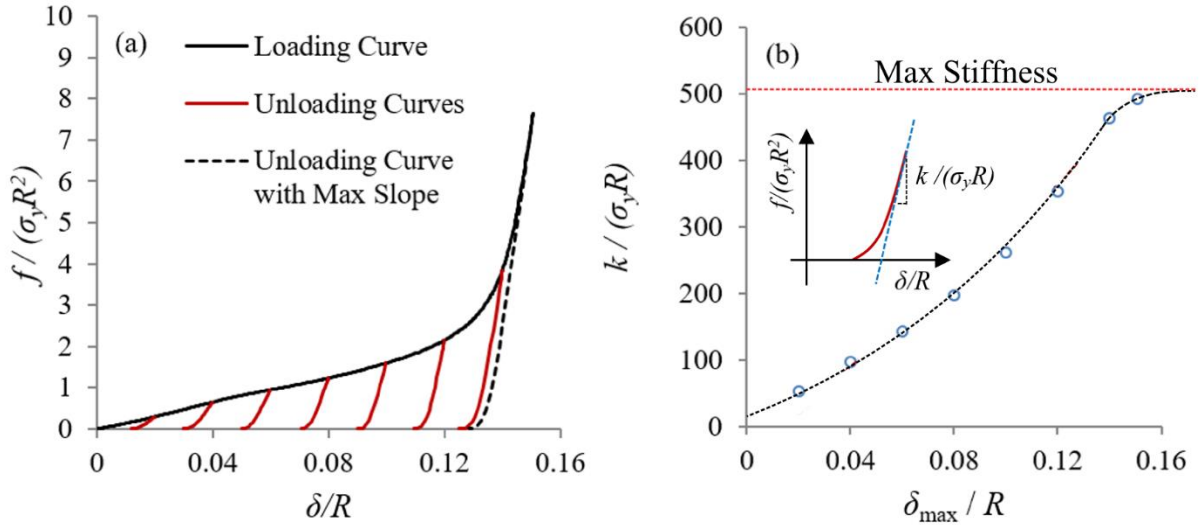

Figure 3.2 (a) Normalized force-displacement behavior of unloading at varying levels of deformation, and (b) normalized unloading stiffness versus varying levels normalized maximum deformations.

3.2.1 Elastoplastic Loading, Unloading of a Contact

The elastoplastic loading of a contact for particles subjected to high confining conditions was assumed to be described by a unique force-displacement behavior with the generic form obtained from FEM analysis. A piece-wise normal contact model for loading was formulated by fitting two curves possessing the same form as the loading curve shown in Figure 3.1. Initial loading of the contact from zero deformation up to a deformation that corresponds to the near termination of plastic flow, δ^*, was assumed to be the sum of two independent terms:

$$f_{\delta \to \delta^*} = f_1(\delta_n) + f_2(\delta_n, \delta_c) \tag{3.1}$$

The first term on the right-hand side of equation (3.1) is the force (f_1) that results from normal contact deformation δ_n between two remote particles; whereas, the second term represents the force (f_2) that is generated as a result contact interaction from neighboring contacts. The force f_2 in equation (3.1) was assumed to be a function of the normal contact deformation and a fictitious deformation δ_c corresponding to the point at which the particle becomes completely incompressible. The force-displacement behavior for $\delta_n > \delta^*$ that corresponds to the elastically dominated region was modeled as a linearly increasing function of deformation with a slope equivalent to the maximum asymptotic stiffness. The piece-wise defined elastoplastic loading model was given by

$$f_l = \begin{cases} f_1 = k_1\delta_n + \dfrac{F\delta_n}{\delta_c - \delta_n} & \text{if } \delta_n \le \delta^* \\ f_2 = \hat{k}_2\left(\delta_n - \delta^*\right) + f_1(\delta_n = \delta^*) & \text{if } \delta_n > \delta^* \end{cases} \tag{3.2}$$

where k_1 and $\hat{k}_2$ are the isolated particle contact stiffness and maximum asymptotic stiffness respectively. These two stiffness measures are input parameters of the DEM contact model. The parameter F in equation (3.2) is an additional input parameter having units of force and is referred to as the interaction parameter in this text.

The force f_l for the elastoplastic loading of a contact is represented by curve 1 in the schematic diagram for the proposed force-displacement behavior of contacts shown in Figure 3.3. The incompressible limit, as shown in Figure 3.3, occurs at the critical deformation given by

$$\delta_c = 2\theta R^* \tag{3.3}$$

where θ is the dimensionless critical deformation limit, and R^* the reduced radius given by equation (1.4). The dimensionless parameter θ represents an additional input parameter in the DEM contact model. The plastic flow limit deformation δ^* is obtained from the deformation at which the contact stiffness becomes equal to the asymptotic stiffness. The contact stiffness in the region of deformation from $0 \le \delta_n \le \delta^*$ is given by

$$S = k_1 + \frac{F}{\delta_c - \delta_n} + \frac{F\delta_n}{\left(\delta_c - \delta_n\right)^2} \tag{3.4}.$$

Solving for the plastic flow limit deformation δ^* in terms of the input parameters $F, k_1, \hat{k}_2$, and θ from the equation $S(\delta^*) = \hat{k}_2$ gives the following result:

$$\delta^* = \delta_c - \sqrt{\frac{F\delta_c}{(\hat{k}_2 - k_1)}} \tag{3.5}$$

The unloading force f_u is represented by curve 2 in the schematic diagram for the adhesive, elastoplastic force-displacement behavior of a contact shown in Figure 3.3. The unloading of contacts was modeled as a linearly decreasing force as a function of decreasing deformation. It was realized that a nonlinear unloading may represent a more realistic description of the force-displacement behavior of contacts; however, since there was both a lack

of experimental details for contact unloading and a desire to calibrate this model from experiments performed on real powder material systems (i.e., particle system consisting on non-spherical particles), a linear unloading force-displacement behavior was used as a compromise.

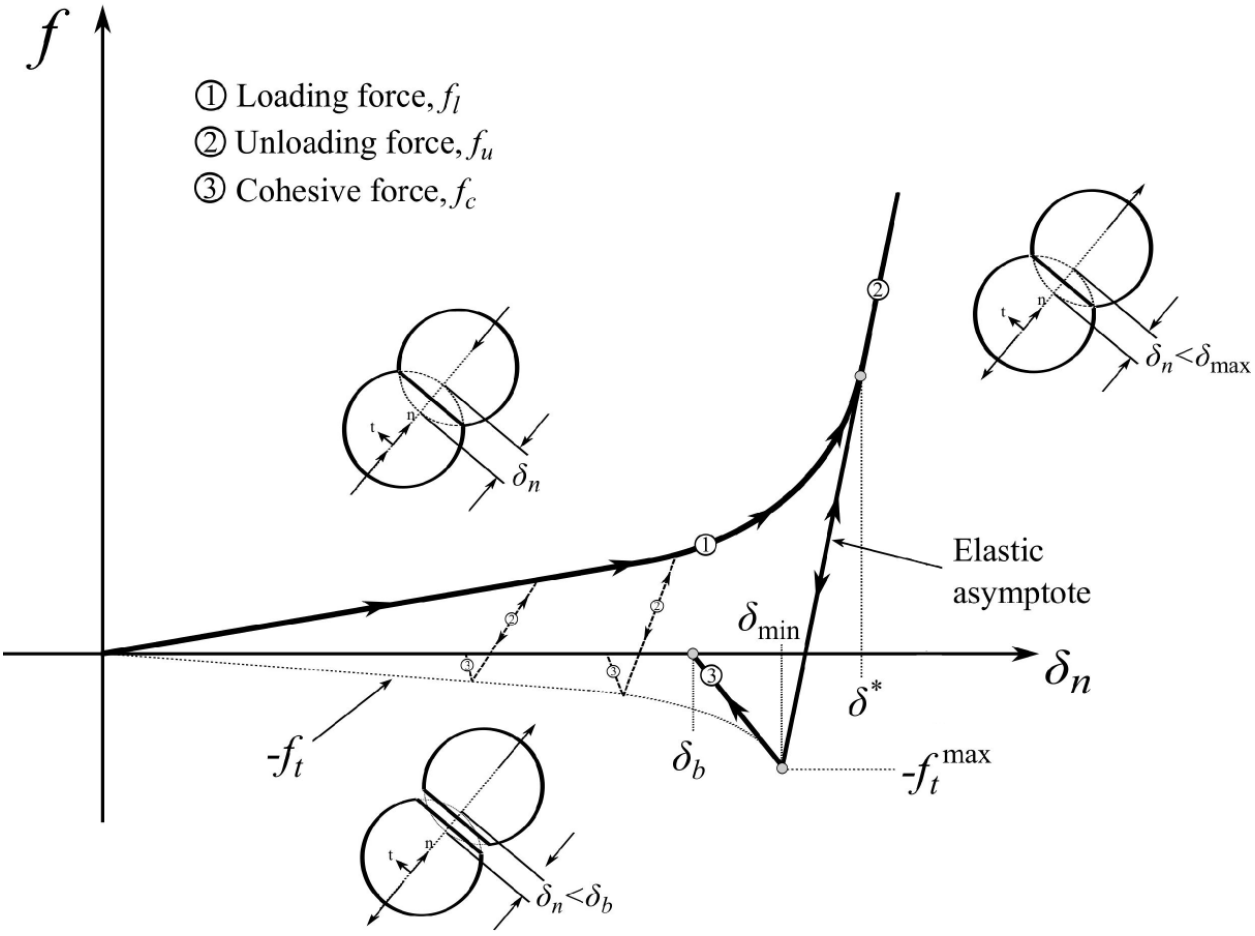

Figure 3.3 Schematic diagram of the normal force-displacement behavior in the proposed contact model

Unloading occurs when the deformation falls below the maximum deformation δ_{max} achieved at the end of loading of the contact. The maximum deformation δ_{max} or the maximum

force f_{max} must be stored at each contact point to define the criterion for unloading. The stored historical value used in the DEM implementation of the contact model in this work was δ_{max}. Thus, unloading of contacts occurs when $\delta_n < \delta_{max}$ as shown in Figure 3.3. During unloading the force decreases along a linear curve with a slope equal to k_2. As schematically depicted in Figure 3.3, for any maximum deformation $\delta_{max} < \delta^*$ the unloading force at contacts takes on the basic form $f_u = k_2(\delta - \delta_{max}) + f_{max}$ and is therefore a function of the historical value δ_{max}. When a maximum deformation $\delta_{max} > \delta^*$ is reached, the unloading force decreases along the asymptotic elastic curve with a slope equal to $\hat{k}_2$ and becomes a function of the plastic flow limit deformation δ^*. If reloading of the contact occurs prior to a contact deformation equal to the minimum contact deformation δ_{min} (deformation at which the maximum tensile pull-off force occurs), the force at the contact will again increase along the same curve (curve 2 in Figure 3.3). The unloading-reloading force-displacement behavior of contacts was given by

$$f_u = \begin{cases} k_2(\delta_n - \delta_{max}) + k_1\delta_{max} + \dfrac{F\delta_{max}}{\delta_c - \delta_{max}} & \text{if } \delta_{max} \le \delta^* \\ \hat{k}_2(\delta_n - \delta^*) + k_1\delta^* + \dfrac{F\delta^*}{\delta_c - \delta^*} & \text{if } \delta_{max} > \delta^* \end{cases} \tag{3.6}$$

To account for the increase in unloading-reloading stiffness with deformation, the slope k_2 was assumed to increase linearly with an increase in maximum contact deformation from a value of $k_2 = S$ at $\delta_{max} = 0$ to the asymptotic elastic unloading slope $\hat{k}_2$ for $\delta_{max} \ge \delta^*$:

$$k_2 = \begin{cases} S + \left(\hat{k}_2 - S\right)\dfrac{\delta_{\max}}{\delta^*} & \text{if } \delta_{\max} \le \delta^* \\ \hat{k}_2 & \text{if } \delta_{\max} > \delta^* \end{cases} \tag{3.7}$$

The linearly increasing unloading-reloading stiffness with increasing maximum deformation given by equation (3.7) is a reasonable assumption for spherical particles as can be seen in Figure 3.2(b). Since experimental details regarding the unloading and reloading of single contacts are lacking, the assumption of a linearly increasing unloading-reloading stiffness with an increasing maximum deformation represented an approximation to the possible nonlinearly increasing stiffness for non-spherical particles. This type of unloading-reloading contact force behavior was also assumed in the contact force model put forth by Luding [105, 141].

A comparison of the proposed adhesive, elastoplastic contact model for two cohesionless particles in contact, FEM simulation of isostatic compaction of mono-sized array of spheres with coordination number Z = 8, and Storåkers similarity solution [60] is shown in Figure 3.4. The purpose of presenting the results shown in Figure 3.4 was to highlight the effect of the interaction parameter F on the force-displacement behavior in loading of the contact. For the proposed contact model results shown in Figure 3.4, zero cohesion was assumed. The isolated particle contact stiffness k_1 was assumed to be given by Storåkers's similarity solution, specifically the isolated particle contact stiffness was given by $k_1 = 3\pi c^2 \sigma_y R$ (see Chapter 1 section 1.2). Figure 3.4 shows the effect of the interaction parameter F with respect to a constant critical deformation δ_c and a constant ratio of $\hat{k}_2/k_1 \approx 30$. It was found that F = 0.18 and $\theta = \delta_c / R = 0.15$ gave a reasonable fitting of the FEM results. For interaction parameter values of $F \approx 0.1 \neq 0$ (F = 0.001 and θ = 0.14 in Figure 3.4), a near bilinear loading is obtained. For an interaction parameter F =0, the similarity solution is obtained.

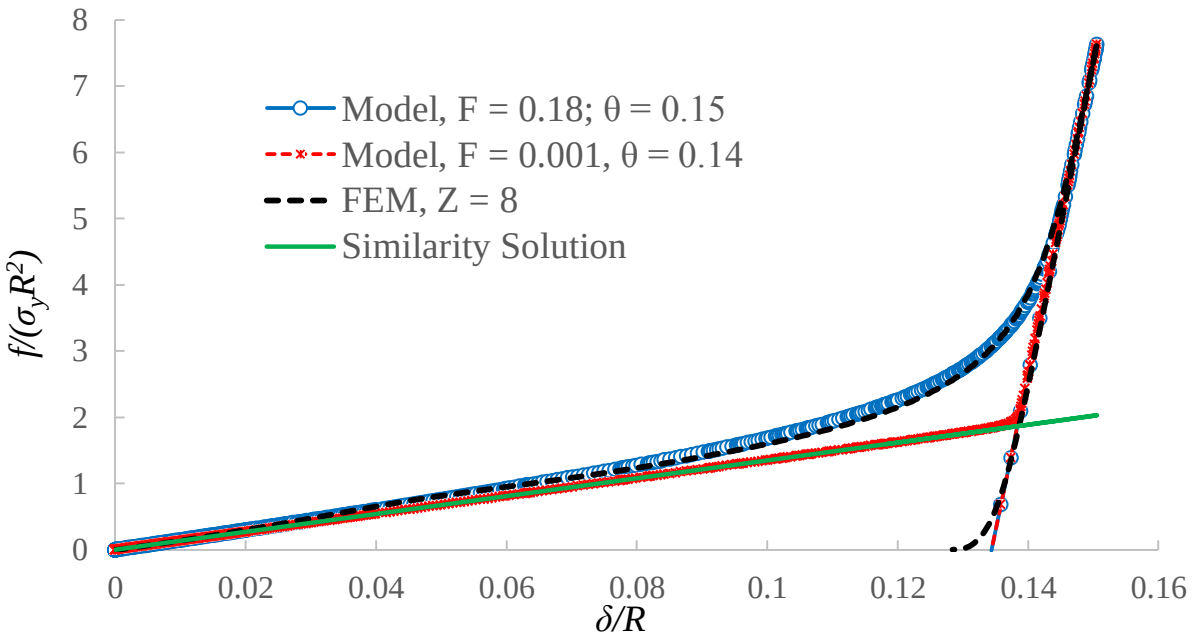

Figure 3.4 Comparison of proposed adhesive, elastoplastic normal contact model with zero cohesion, FEM simulation of isostatic compaction of mono-sized array of spheres with coordination number $Z = 8$, and Storåkers similarity solution.

3.2.2 Tensile Forces at a Contact

In order to enable the evolution of tensile strength in the compacted solid, bonding between individual particles is considered to occur is cases of finite maximum deformations δ_{max} attained at the end of contact loading. An expression that correlates the emerging maximum contact strength to the maximum normal compressive force at the end of contact loading was introduced. More precisely, the maximum tensile pull-off force f_t between two particles was assumed to evolve with the maximum contact force f_{max} given by

$$f_t = \begin{cases} \lambda\left[k_1\delta_{\max} + \dfrac{F\delta_{\max}}{\delta_c - \delta_{\max}}\right] = \lambda f_{\max} & \text{if } \delta_{\max} \le \delta^* \\ f_t^{\max} = \lambda\left[k_1\delta^* + \dfrac{F\delta^*}{\delta_c - \delta^*}\right] = \lambda f_{\max}^* & \text{if } \delta_{\max} > \delta^* \end{cases} \tag{3.8}$$

where the constant λ represents the ratio of the maximum contact tensile pull-off force to maximum contact force at the end of contact loading. It was assumed that the force $f_{\max}^*$ does not increase beyond δ^*. The maximum tensile force behavior given by equation (3.8) was assumed to a behavior similar to the force pull-off behavior established in the analytical expression developed by Mesarovic and Johnson [69], namely $f_t \approx 1.09\chi f_{max}$ (see Chapter 1 section 1.3). However, it is important to note that the proposed cohesive parameter λ and the cohesive parameter χ do not have the same meaning. The cohesive parameter χ introduced by Mesarovic and Johnson represented the ratio of the adhesive energy to the elastic energy stored in the fully unloaded contact. In the proposed model, the cohesive parameter was meant to represent the ratio of the maximum tensile force to the maximum force achieved at the end of loading. Similar to Mesarovic and Johnson's cohesive parameter, the cohesive parameter λ characterizes the level of cohesive forces between contact surfaces and is a parameter that can be obtained from calibration using experimental results. As such, this parameter is another input parameter to the proposed DEM contact model.

Figure 3.3 shows the evolution of the maximum tensile force behavior with increasing deformation. It can be seen that the tensile force-displacement behavior follows the same force-displacement behavior of contact loading for normal deformations in the range $0 \le \delta_n \le \delta^*$. As can be seen from Figure 3.3, decreasing deformation below the plastic contact deformation δ_0 leads to attractive cohesive forces until a minimum contact deformation $\delta_{\min}$ is reached. The

minimum contact deformation $\delta_{\min}$ denotes the deformation at which the maximum load carrying capacity of contact surfaces are achieved and is defined in terms of the maximum contact deformation at the end of loading by

$$\delta_{\min} = \begin{cases} \delta_{\max} - \dfrac{f_{\max}(1+\lambda)}{k_2} & \delta_{\max} < \delta^* \\ \delta^*_{\min} = \delta^* - \dfrac{f^*_{\max}(1+\lambda)}{\hat{k}_2} & \delta_{\max} \geq \delta^* \end{cases} \tag{3.9}$$

where $\delta^*_{\min}$ is referred to as the limiting minimum contact deformation in this text, and corresponds to the deformation at which the limiting maximum tensile contact force $f_t^{\max}$ is reached. The justification for imposing this limiting maximum tensile contact force $f_t^{\max}$ was related to a limiting contact area occurring at the plastic flow limit contact deformation δ^* pertaining to contact impingement. Since cohesive forces between solid particles are strong functions of contact area [69], it was assumed that any further increase in deformation beyond δ^* would not result in any significant increase in contact pull-off forces due to the termination of evolving contact area.

The final portion the proposed contact model considers the cohesive force f_c represented by curve 3 in Figure 3.3. The force-displacement behavior given by this curve was introduced to signify the decrease of load carrying capacity of contacts for decreasing deformation below $\delta_{\min}$. For normal contact deformations $\delta_n < \delta_{\min}$ the load carrying capacity of the contact was assumed to diminish according to

$$f_c = f_t \frac{\delta_n - \delta_b}{\delta_b - \delta_{\min}} \tag{3.10}$$

where δ_b is the full-separation deformation corresponding to the complete loss of load carrying capacity of contacts (i.e., contact decohesion) The full-separation deformation was assumed to be some fraction of the minimum contact deformation and was given by

$$\delta_b = C\delta_{\min} \tag{3.11}$$

where C is a parameter that represents the ratio of the full-separation deformation to the minimum deformation. The additional DEM contact model input parameter C is a parameter with values ranging from zero to one. As shown in Figure 3.3, the cohesive portion of the adhesive, elastoplastic contact model is represented by the negative normalized force curves that form a triangle under the δ – axis. This type of cohesive triangular force-separation response is similar to the typical traction separation behavior often employed in continuum damage modeling [138]. The area of the triangle can be considered the cohesive energy W_c or the energy dissipated due to contact failure:

$$W_c = \frac{1}{2}\left(\delta_0 - \delta_b\right) f_t \tag{3.12}$$

The deformation δ_b allows for tuning of the energy dissipated during contact loss. Figure 3.5 shows a schematic of different contact failure modes based on the input parameter C. When C = 1 the full-separation deformation $\delta_b = \delta_{\min}$, which would result in contact surface separation

occurring instantaneously at the moment the failure criterion $f_t = \lambda f_{\max}$ is reached. This type of contact surface separation would represent an unstable contact separation (i.e., unstable crack propagation), which is indicative of brittle failure (Figure 3.5(a)). For two types of contact failure modes shown in Figure 3.5(b) and Figure 3.5(c), the dissipation of energy associated with contact surface separation can be either due to some degree of plastic deformation occurring during failure or a combination of several adhesive energy dissipation mechanisms at work. Specifically, the energy dissipated for these two types of contact failure modes can be described by the energy release rate $G = W_c = \Delta\gamma_s + \gamma_p + \gamma_{other}$, where $\Delta\gamma_s$ is the adhesive surface energy, γ_p the energy dissipation due to plasticity, and γ_{other} the energy dissipated from other dissipative mechanisms.

For a current normal deformation along curve 3 shown in Figure 3.3 that changes from a decreasing deformation to an increasing deformation (i.e., $\Delta\delta_n < 0 \rightarrow \Delta\delta_n > 0$), it was assumed that reloading of the contact from this tensile state follows the curve given by curve 4 in Figure 3.3. The reloading contact force-displacement behavior given by this curve is similar to the behavior used to define linear softening of damaged surfaces in continuum damage mechanics [138]. By "softening", it is meant that the stiffness at the contact does not reload with a stiffness equal to k_2, but is instead softened such that the reloading slope is less than k_2. Consequently, this type of reloading behavior is also identical to the reloading force-displacement behavior from a tensile state assumed in the contact model introduced by Walton and Johnson [106]. The reloading force was given by

$$f_R = f_c \frac{\delta_n - \delta_0}{\delta_0 - \delta_R} \quad \text{if } \delta_n \geq \delta_R \tag{3.13}$$

where δ_R is reference deformation for reloading. Similar to the stored historical deformation δ_{max}, the reference deformation also represented a stored value in the DEM model implementation for the purpose of accommodating this type of reloading.

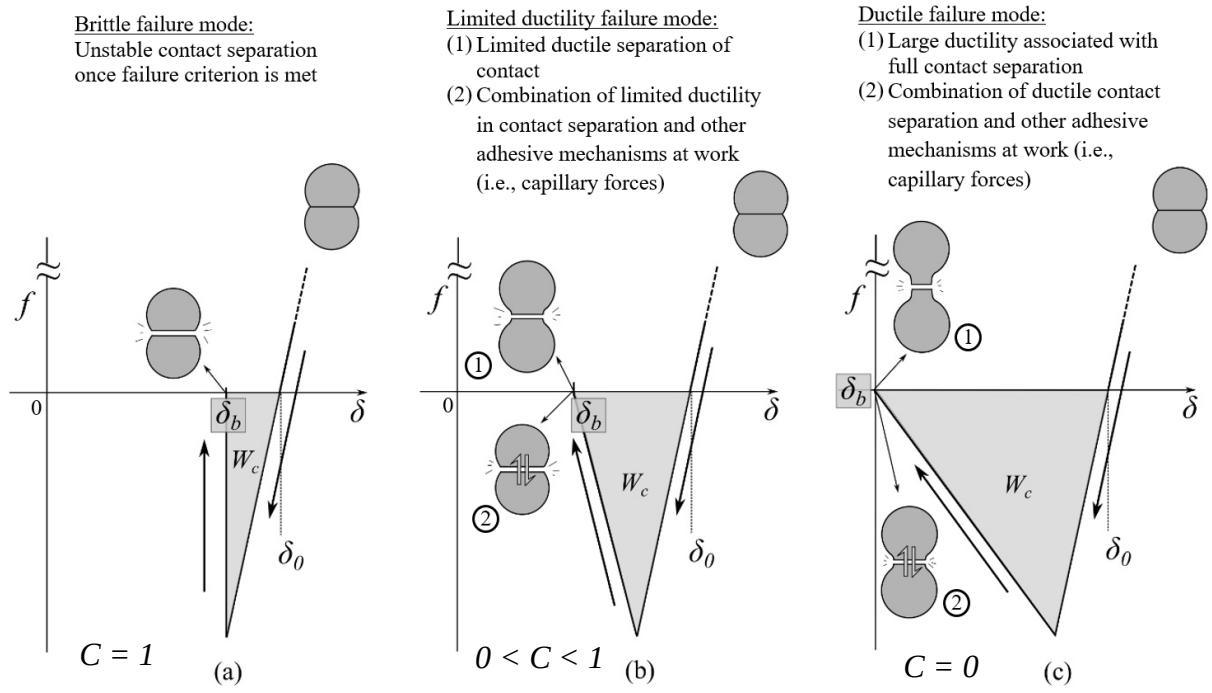

Figure 3.5 Schematic of cohesive portion of adhesive, elastoplastic normal contact model for different contact failure modes as a function of the input parameter *C* where the following failure modes are represented: (a) brittle contact separation, (b) limited ductile contact separation, and (c) large ductile contact separation.

3.2.3 Summary of the Proposed Adhesive, Elastoplastic Normal Contact Model

The proposed adhesive, elastoplastic normal contact model was a model developed to approximate the behavior of particles subjected to high confining stresses, or equivalently, particle assemblies compacted to high relative densities. The proposed contact model uses the

key assumption that a unique force-displacement behavior that incorporates a heuristic approach to the effect of influencing neighboring contacts in loading could be used to adequately model the die compaction of particles. In the formulation of this model, the following DEM input parameters emerged:

- k_1 the isolated particle contact stiffness that arises from only two particles in contact
- $\hat{k}_2$ the maximum asymptotic stiffness related to the full density elastic properties of the particle assembly
- θ the dimensionless critical deformation limit that defined the critical deformation δ_c at which the particle assembly becomes completely incompressible
- λ the cohesive parameter that defined the failure criterion for particle-particle contacts and is defined as the ratio of the maximum tensile force f_t to the maximum force at the end of loading $f_{\max}$
- C the parameter that defines the ratio of the full-separation deformation δ_b and the minimum contact deformation $\delta_{\min}$ and can be thought of as the parameter that determines the level of cohesive energy dissipated during contact separation

Thus, the proposed contact model is a six-parameter model. It should be noted that all other parameters of this contact model are functions of the six DEM input parameters. With the exception of the interaction parameter F, the remaining input parameters were sought in the calibration of the proposed contact model from macroscopic experiments performed on a real powder system. For all simulations performed in this work, the interaction parameter was assumed to be equal to the value found in the fitting of this model to the FEM simulation

performed on a regular array with a coordination number $Z = 8$, specifically the value of the interaction parameter was $F = 0.18$ for all simulations conducted.

3.3 Materials and Methods

In order to investigate the behavior of powder materials in the compaction process, a number of suitable simulations were chosen with the idea that these simulations could reflect the real behavior of compacted powders and provide valuable insight into the compaction behavior. While it is quite possible to conduct a DEM study of full scale simulations for the compaction of powders, in the interest of computational cost and efficiency, simplifications such as using a represented volume of particles and mass scaling (see Chapter 1 section 1.4.1) allow for a much more manageable simulation time and treatment of the DEM output data.

Since die compaction is the most practical and common means of producing powder compacted parts, this work was primarily interested in the behavior of compacted powder in the die compaction process, specifically the three stages: loading, unloading, and ejection. As such, compactions related to isostatic and triaxial compactions were not considered. The effect of flow as it relates to die filling was also not considered in this work.

3.3.1 Material Selection

The material used for the calibration of the proposed DEM model parameters was hot-melt extrusion (HME) copovidone powder, a material often used in the pharmaceutical industry as a binder material or matrix material for controlled-release tablet formulations. The

copovidone extrudate was milled using an FS 75 table top Fitz-mill (Fiztpatrick, Elhurst, IL) and sieved between a 212 micron and 106 micron screen to produce particle size diameters within this range. The true density of the powder was attained using the pycnometer testing machine, Accupyc II TEC (Micromeritics Instrument Corporation, Norcross GA, USA), which gave a true density value of 1.21 g/cm^3 and the bulk density at filling of 0.54 g/cm^3 for the sieved powder that was equilibrated in a 22-23% relative humidity (RH) environment for two weeks.

HME copovidone powder provides some attractive characteristics that make this material a suitable model material for the extraction of the proposed DEM model parameters. The proposed DEM model assumes deformation at the contacts occurs by elastic-perfectly plastic deformation with little or no hardening. Powder materials possessing internal porosity would represent materials in which the plastic strain hardening persists well beyond the incipient yield point of the powder granule. It has been found that hot-melt extrusion technology results in significantly lower or negligible pore sizes and porosity for extruded polymer materials [142]. HME copovidone powder has negligible internal porosity; thus, a single value for its yield strength can be used.

Another important consideration of the model material used for the extraction of the model parameters is the separation of contacts *via* interparticle decohesion rather than transgranular fracture of the individual powder particles. The proposed model assumes that the generation of defects (i.e. cracks) occur as a result of contact loss and does not take into account fracturing of the individual powder granules. An investigation of a fracture surface a compact that was diametrically compressed until failure was performed using a Zeiss Supra 50VP (Carl Zeiss Microscopy, LLC, Thornwood NY, USA) scanning electron microscope. The fracture surface was sputter-coated with conducting material (platinum/palladium) and imaged using

conventional high-vacuum SEM with an accelerating voltage of 5 kV. Figure 3.6(a) shows the fracture surface of a copovidone compact initially die-compacted to a relative density of approximately 95 %. The morphology of the surface points to failure along the prior particle boundaries. Interesting is the smooth appearance of the fracture surface at higher magnifications (Figure 3.6(b)). The smooth surface in Figure 3.6(b) indicates failure as a result of particle-particle decohesion where the fracture path follows the compressed particle grains of the compact. While some degree of particle transgranular fracturing may occur in this material, it is assumed that the primary form of contact loss is from separation of particle-particle surfaces.

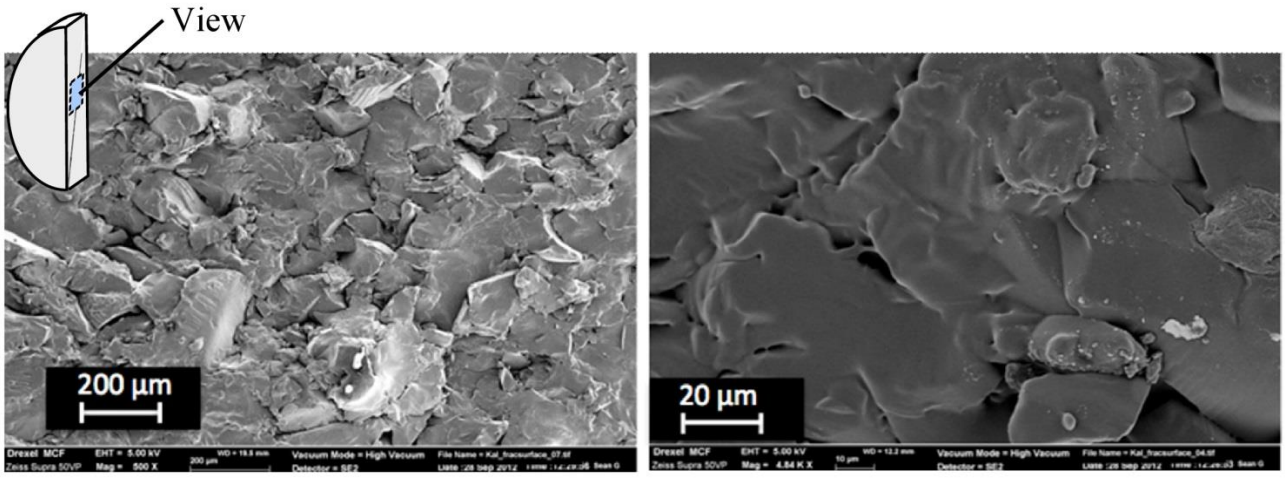

(a) (b)

Figure 3.6 (a). Fracture surface of diametrically compressed copovidone compact at 500 X mag, and (b) the same fracture surface at a higher magnification.

3.3.2 Macroscale Mechanical Testing Experiments

The identification of the model parameters were made using macroscopic experimental data obtained from two experiments. Die compaction experiments were carried out by the use of a fully instrumented Huxley Bertram compaction simulator (Huxley Bertram Engineering Ltd, Cambridge England). The copovidone powder was compressed in a lubricated die *via* the displacement of top and bottom punches. Die compaction experiments using a 10 mm diameter die and flat punches, with sodium stearyl fumurate used as a lubricant for each compaction experiment were conducted to produce tablets having a relative densities ranging from approximately 70% to 95% RD. For each compaction experiment, forces on upper and lower punches were recorded using load cells with a 50 kN capacity. Measuring and recording radial stress during each experiment was achieved using an instrumented die with a 200 MPa capacity piezoelectric sensor.

For the extraction of the proposed DEM model parameters pertaining to tensile forces at contacts, diametral compression strength tests were performed using a VK200 tablet hardness tester (Agilent Technologies, Santa Clara, CA). The diametral compression test, also referred to as the Brazilian disk test in rock mechanics [142] and the hardness test in pharmaceutical assessment of tablet strength [143], is a typical test for compacts that relies on the generation of a lateral tensile stress at the center of the sample to probe the tensile strength of the material [134, 135]. Compact breaking forces were measured for each relative density compact at a test speed of 0.02 mm/s and the diametral tensile strengths were calculated using the following equation

$$\sigma_T = \frac{2P_f}{\pi Dt} \tag{3.14}$$

where P_f is the load at failure, D is the diameter of the specimens, and t is the measured compact thickness.

3.4 Numerical Modeling and the DEM Implementation

The discrete element method was used to simulate the compaction of an assembly of particles in the die compaction process. The open-source code LIGGGHTS version 3.2.1 (**L**AMMPS **i**mproved for **g**eneral **g**ranular and **g**ranular **h**eat **t**ransfer **s**imulations) was used for running all DEM simulations in this work. LIGGGHTS [144] is an extension of the well-known molecular dynamics code LAMMPS. Aside from the myriad of features that are comparable to many commercial DEM codes, LIGGGHTS is highly extensible and allows for modifying and extending the source code. Since the current version LIGGGHTS DEM code implementation only consists of general normal contact models (e.g. Hertz, Hooke, and Luding contact models) , it was necessary to modify and extend the capabilities of LIGGGHTS by incorporating the newly proposed adhesive, elastoplastic normal contact force model. Like many available DEM codes, LIGGGHTS also offers the ability to employ parallel computing. This parallel computing capability was taken advantage of for all simulations performed.

Unless otherwise stated, all DEM compaction simulations consider the pressing of powder particles in cylindrical dies in which the final geometry was modeled as a cylindrical flat-faced compact as depicted in Figure 3.9. Using the DEM, the interactions between spherical particles are accounted for by simulating the evolution contacting particles during the pressing of

the particle assembly from an initial solid fraction to a final relative density. At each incremental time step, the interparticle forces between contacting particles are calculated, which allows for the determination the new position of each particle at the following time step $t + \Delta t$. The evaluation of the time step Δt for the particle assemblies was achieved by calculating the critical time step as suggested by Itasca [94] (see Chapter 1, section 1.4.1):

$$\Delta t_c = \sqrt{\frac{m}{k}} \tag{3.15}$$

where m is the mass of the smallest particle and k the largest expected stiffness. In this work, only monosized assemblies of spherical particles were considered and mass scaling of the nominal density (10^4 times the nominal density) of the particles was employed in order to attain a reasonable critical time step. The forces and particle motions have been found to be largely unaffected by mass scaling provided that particles are maintained at equilibrium conditions [46]. For the varying levels of stiffness used in this work, a critical time step of $\Delta t_c = 2.5 \times 10^{-6} s$ was found to be sufficient for all compaction simulations.

3.4.1 Generation of Initial Configurations

Initial configurations (i.e., initial filling of the die) of monosized assemblies of spherical particles were obtained by deposition of initially non-contacting particles from a fixed height of two times the die height under the force of gravity (Figure 3.7(a)). It was necessary to scale the acceleration due to gravity to reflect the mass scaling used in the DEM implementation (

$g_{scaled} = \rho_{actual} g / \rho_{scaled}$). At the beginning of every deposition simulation performed, the spherical particles where randomly distributed in space and each particle was given a random initial velocity with a mean of zero m/s and a standard deviation of ± 10^{-3} m/s. The gravity deposition method used to obtain the initial configuration generally involves significant particle movement and large numbers of collisions under highly dynamic conditions. Noting this fact and the fact that mass scaling was used, it was decided that particle-particle contact interactions would be modeled using a purely Hertzian contact force-displacement behavior (see Chapter 1, section 1.2) for deposition purposes only. Thus, the particle-particle contact deformations for final random initial configuration experienced only small strain deformations per particle with an average maximum deformation of $\overline{\delta}_{\max} \approx 5 \times 10^{-5} R$.

An important consideration for generating the initial configurations of particle assemblies used in simulations performed in this work was the requirement of an initially stable system. Therefore, a *percolating* initial configuration was sought. A percolating network of contacts that spanned the entire initial configuration and transmitted the applied boundary stresses across the system was achieved when (1) the kinetic energy *KE* of the system was many orders of magnitude smaller than the potential energy – typical five orders of magnitude, and (2) an initial relative density in the range $0.56 < RD < 0.64$ was acquired. In the seminal paper by Scott and Kilgour [145] it was found that initial packings of a random monosized spherical assembly of particles possessed an initial relative density equal to 0.64 and is typically referred to as a random *close* packing (RCP). Later, it was found that a lower random *loose* packing (RLP) limit of $RD = 0.56$ still gave a stable percolating structure [145]. Therefore, a stable system was assumed if the calculated relative density fell within the RLP to RCP ranges. For initial relative densities within this range, the average coordination number *Z* falls within the range of

approximately $4.2 < Z < 6.2$ [48]. The initial relative density for the assemblies generated was calculated by

$$RD_0 = \frac{4/3\, N_p\, \pi R^3}{\pi R_d^2 H_0} \tag{3.16}$$

where N_p, R, R_d, and H_0 are the number of particles in the particle assembly, the radii of the particles, the radius of the die, and the initial die fill height respectively. The initial die fill height was taken as average height of particles in the range ($z_{\max} - R \le z_p \le z_{\max} + R$), where $z_{\max}$ is the z-center-point-coordinate of the particle p possessing the maximum height in the assembly. To increase both the likelihood of generating a stable initial configuration and to achieve the highest possible initial relative density, an interparticle coefficient of friction μ of 0.01 was used for deposition simulations. The input parameters of the Hertz contact model, equivalent elastic modulus E^* and Poisson's ratio v, where made equal to 10 GPa and 0.3 respectively.

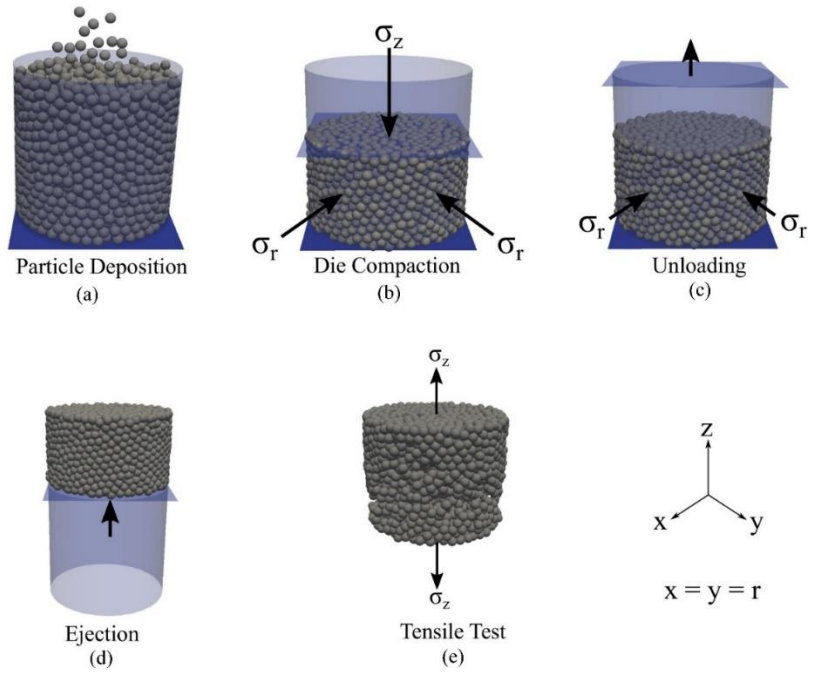

Figure 3.7 Schematic of the various stages of the compaction process and tensile testing of monosized assemblies of spherical particles simulated in the DEM.

Figure 3.7(b-d) shows the three main stages of the die compaction process. To simulate the compaction process, the punches and die walls were modeled as frictionless rigid surfaces. The pressing of the powder assembly was facilitated by the downward displacement of the upper punch while maintaining a stationary position of the bottom punch (Figure 3.7(b)). To minimize the influence of the dynamic and inertial effects, a constant velocity equal to 1.5 X 10^{-4} m/s was imposed for the motion of the top wall for the loading stage. The imposed wall velocity was calculated to be less than the maximum speed corresponding to a critical time step for a moving boundary by the use of Kremmer and Favier's [95] critical time step calculation (see Chapter 1, section 1.4.1). Similarly, unloading was accomplished by the recession of the upper punch using the same punch velocity during the loading phase (Figure 3.7(c)). Finally, the compact was ejected from die by employing an upward displacement of the bottom punch at a velocity of 2.0

X 10^{-4} m/s. Using the velocities of the moving boundaries and critical time steps discussed above, simulation results showed no requisite for contact damping. Although damping is a common approach to minimize inertial and dynamic effects, it was found that simulation results were largely unaffected by the use of damping when using reasonable damping coefficients (i.e., coefficients of restitution in the range of $0.85 \leq e \leq 1$ are generally considered reasonable [105]).

To assess the strength of the ejected pressed powder assembly, tensile test simulations were performed as depicted in Figure 3.7(e). The macroscopic rate of deformation imposed to the compact during tensile test simulations was achieved by employing a translational boundary condition in the z-direction to the centers of particles that constitute the upper boundary of the compact while the particles representing the lower boundary of the particles are kept stationary. No boundary constrainst in the x and y directions were imposed on upper and lower boundary particles. Since it was expected that an unstable contact separation may be possible during the tensile test simulations, the imposed velocity of the upper boundary was made equal to 1.5 X 10^{-6} m/s to ensure a "safe" integration of the equations of motions – two orders in magnitude less than the critical time step used in loading and unloading of the powder assembly.

3.4.2 Contact Forces

For compaction, unloading, ejection, and tensile testing (Figure 3.7(b-e)), the normal force-displacement behavior was modeled using the proposed adhesive, normal contact model. For simulations performed in this work, the model input parameter that represents isolated particle-particle contact, k_1, was replaced by Storåkers' similarity solution for elastic-perfectly plastic material behavior ($k_1 = 3\pi c^2 \sigma_y R$). Concerning the tangential forces at contacts, a tangential force-displacement behavior that has been implemented in DEM models of

compaction by other researchers was employed [48, 105, 110]. Specifically, it was assumed that the contacts were either in a state of gross sliding, modeled by the Coulomb friction model (see Chapter 1, section 1.4.4), or in a sticking state defined by a tangential stiffness k_t:

$$T = \begin{cases} -k_t \delta_t & k_t \|\delta_t\| \le \mu f_n \\ -\mu f_n & k_t \|\delta_t\| > \mu f_n \end{cases} \tag{3.17}$$

The variables δ_t and μ in equation (3.17) are the tangential displacement and the interparticle coefficient of friction respectively. This type of tangential force behavior persisted throughout loading and unloading of the particle assembly, regardless of the level of deformation. The tangential stiffness k_t was assumed to be defined by a multiple of the normal stiffness S given by equation (3.4). In the work by Olsson and Larsson [110], they suggested that values of k_t in the range of 0.5-5 times the normal stiffness gave stable numerical results. Martin [80] has suggested that the tangential stiffness should be sufficiently large to ensure the sticking state. In this work, the tangential stiffness was assumed to be two times the normal stiffness $k_t = 2S$ where S is given by equation (3.4).

At this point, it should be emphasized that rotation of particles were not included into the DEM implementation. Therefore, the equilibrium of moments as a consequence of interparticle frictional effects were not ensured. The justification for excluding rotation was due to the fact that large plastic deformation was expected for particle contacts subjected to high confining conditions in the compaction process. These large plastic contact deformations should act to prevent the possibility of rotation. Redanz and Fleck [45] found that rearrangement of particles due to particle rotation was negligible for plastic contacts in the compaction of 2D random

arrangement of monosized disks. However, the same cannot be said for contacts that have not been subjected to these large plastic deformations. Experimental [146] and numerical [147] results have shown that particle rotation does influence the macroscopic response of powders. The influence from particle rotations can be primarily attributed to the beginning stages of compaction before significant contact deformation has taken place. Further work should be conducted to assess whether or not rotation of particles significantly affects the macroscopic response for poly-sized particle systems.

3.4.3 Convergence Study

To obtain the relevant simulation data for calibration of the proposed adhesive, elastoplastic normal contact model parameters, as well as the effect that these input parameters have on the macroscopic response, it was necessary to decide on the number of particles to be used in the DEM simulations. A convergence study was conducted to evaluate the macroscopic response from die compaction results for a number of particle systems: N_p = 500, 2000, 3000, 5000, 10000, and 20000. Convergence was assessed in terms of the maximum axial stress at a final relative density of 0.98 and in terms of the corresponding tensile strengths of each of the particle systems. The evaluation of convergence for maximum compaction pressure included both compaction of the particle systems in rigid dies, as depicted in Figure 3.7, and compaction using periodic boundary conditions for particle systems N_p = 2000, 3000, and 5000. An example of an initial configuration for a 3000 particle system using periodic boundary conditions is shown in Figure 3.8. The periodic boundaries exist in the x and y directions, which means that any particle leaving an outer boundary in either the x-z plane or the y-z plane will enter the boundary opposite to these planes. Thus, it is assumed that the material response can be

represented by the repeated representative volume of particles, which fill infinite space in the x and y directions. Here, a comparison of the maximum compaction pressure is made to show how the particle systems behaves with and without walls.

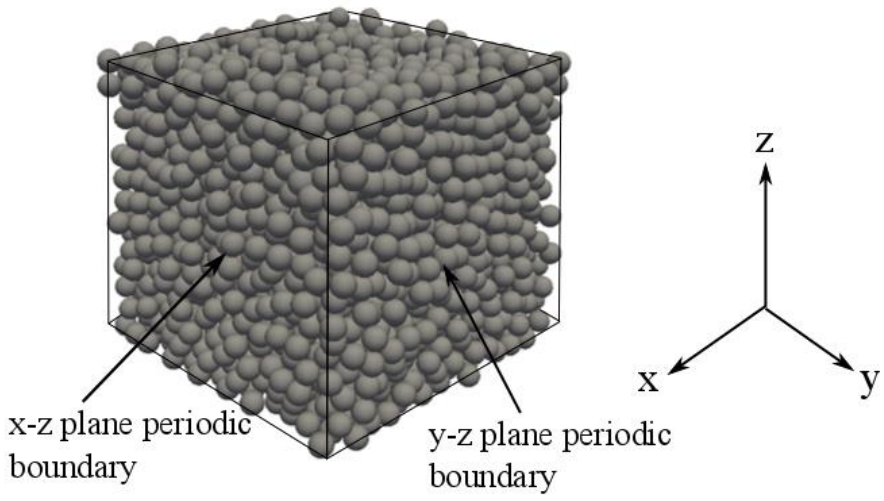

Figure 3.8 Initial configuration of 3,000 particle assembly with periodic boundary conditions in x and y directions

Figure 3.9(a-b) shows results from a convergence study performed on the different particle systems discussed above. Table 3.1 gives the model input parameters used in the convergence study. The results shown in Figure 3.9(a) are for the normalized maximum compaction pressure at 0.98 in-die-RD for particle systems compacted in rigid dies and compacted using periodic boundary conditions, as well as the computational time [1](CPU time) required to simulate the loading, unloading, and ejection stages of the compaction process. Similarly, Figure 3.9(b) shows the normalized axial tensile strength results for the various particle systems along with CPU time necessary to complete the simulations. The maximum compaction pressure and the tensile strength of the particle systems shown in Figure 3.9 have

been normalized by yield strength, which was defined in terms of k_1 by $\sigma_y = k_1 / \left(3\pi c^2 R\right)$. Figure 3.9(b) does not include tensile strength results for the systems compacted using periodic boundary conditions as it was not possible to eject these compacts.

Table 3.1 DEM model input parameters

Parameters	Value	Units
ρ	10^7	kg/m^3
R	100	µm
k_1	37.5	kN/m
$\hat{k}_2 / k_1$	30	
F	0.18	
θ	0.35	
λ	0.175	
C	0.75	
μ	0.2	
Δt_c	2.5	µs
v (Upper punch)	0.15	mm/s

From Figure 3.9(a), it is shown that a significant difference between N_p = 500 and 20000 particle systems compacted in rigid dies. Near-convergence for the assemblies compacted in rigid dies appears to occur for roughly N_p =10000. The CPU time increase is shown to range from approximately 0.4 hours for the N_p =500 particle system to approximately 10 hours for the N_p =20000 particle system. From Figure 3.9(a), it can be seen that convergence appears to occur much sooner when using periodic boundary conditions.

The result shown in Figure 3.9(a) reveals both the effect of the walls and the effect that the number of particles has on the effective area of contact between the particles and walls.

When rigid walls are used, particles belonging to smaller particle systems tend to align with wall boundaries giving little ability for lateral movement of the particles. The result of this hindrance of lateral movement means that particles become "locked" into position much sooner for smaller particle systems than for larger particles systems. Furthermore, the ratio of the total effective particle-wall contact area to the area of the punch surface decreases for smaller particle systems—the reason for lower normalized maximum stress for smaller particle systems when calculating stress in terms of the surface area of the punch. The larger observed maximum stress calculated from the total effective particle-wall contact area for smaller particle systems shows how the effect of the aligning particles along the rigid boundaries results in larger stresses and an overall increase in the rigidity of the material response. This effect is confirmed by comparing compaction of particle systems in periodic cells, where it can be seen that the stresses are lower—an indication that lateral movement is less hindered.

Results from the convergence study of the normalized tensile strength shown in Figure 3.9(b) reveals that assessing convergence in terms of the number of particles is complicated by the fact that pressed powders tend towards brittle-like behavior. From Figure 3.9(b) it is shown that a monotonically increasing or decreasing normalized tensile strength as a function of the size of the particle system is non-existent. For brittle or quasi-brittle materials, the maximum stress that a specimen can withstand before failure may vary, even under identical testing conditions [148]. This type of behavior is related to the distribution of physical micromechanical flaws (i.e., microcracks) present in the body or surface of the brittle sample. For the sake of simplicity, it is assumed in this work that near-convergence occurs for the N_p = 5000 particle system.

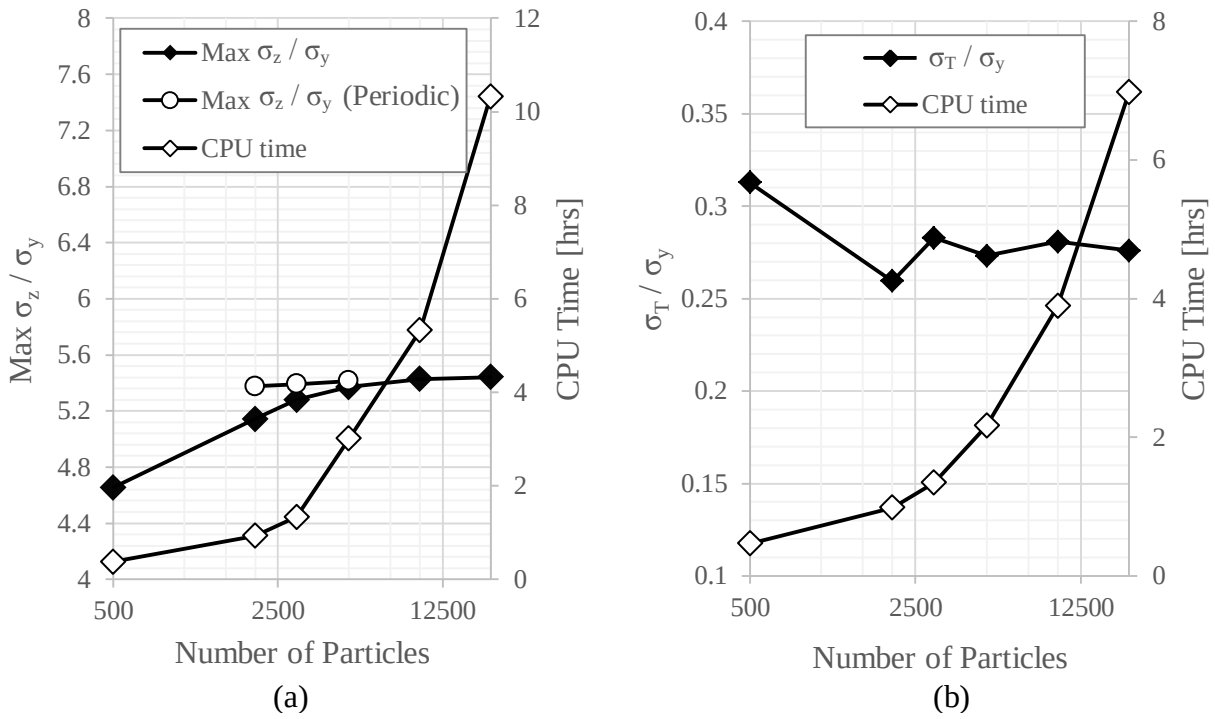

Figure 3.9 Particle number convergence study with (a) normalized maximum compaction pressure at 0.98 RD for particle systems compacted in rigid dies and compacted using periodic boundary conditions and (b) normalized axial tensile strength of particle systems compacted in rigid dies. Included in (a) is the CPU required to complete the loading, unloading, and ejection stages of the compaction process and in (b) is the computation time required to complete the tensile test simulations.

Unless otherwise stated, the number of particles used in all simulations performed was equal to N_p = 3000. This particle system was decided upon based on a compromise between accuracy of the simulated results and CPU time. For loading and unloading simulations, the choice of N_p = 3000 means a percent error in simulated results of approximately 3.3%. Similarly, assuming the tensile strength results do not change significantly for different initial configurations, the percent error in simulated tensile strength results would give approximately

2.6%. The initial relative density of the 3000 particle system was calculate to be approximately equal to 60% RD.

3.5 Calibration of Contact Model Parameters

One of the goals of this study was aimed at the ability to easily calibrate the parameters of the proposed contact model for a real powder system—in this work, HME copovidone. It was important to establish the nature of experimental testing that was used for the purpose of calibration. The two possibilities for experimental testing are tests performed at the local level (i.e., test performed on individual particles) or tests performed on macroscopic samples. Local level tests may include, for example, atomic force microscopy (AFM) using colloidal probes—referred to as colloidal probe microscopy—to obtain results pertaining to the cohesive properties of the contacts. While it has been shown that this method of obtaining information about cohesive properties is possible, this type of testing is riddled with several undesirable outcomes [149]. Example include large variability in the results as well as the fact the typical colloidal probes are on the order of hundreds of nanometers, which are much smaller than typical particle sizes used in powder compaction applications. It is felt that results obtained from using these small probes are not representative of real problem. Similar to the difficulty in obtaining information related to the cohesive properties of particles from local level tests, the same difficulty can also be imagined for acquiring the contact force-displacement behavior of particles. In general, performing tests on individual particles is difficult to say the least. Therefore, testing on macroscopic samples was the approach taken in this work. In order to obtain the input parameters of the proposed contact model from macroscopic tests, it was necessary to employ statistical methods that allowed for the systematic determination of the

input parameters. As such, the statistical method chosen for this purpose was the use of a *Design-of-Experiments* (DOE) approach.

There is currently a lack of knowledge related to how DEM model parameters should be determined for compaction of powders to high densities in order to produce accurate quantitative predictions. A method that has been used extensively for the screening of parameters in experimental studies is the DOE procedure. The DOE procedure is an effective method for planning experiments for the purpose of obtaining data for analysis of multiple variables that affect a response in an efficient and systematic way. This method has also found wide use in the extraction of parameters of micro-mechanical models and has been proved successful for the determining the of optimal model parameters the best predicts the material response. One of the first works to apply the DOE method to DEM models was performed by Yoon [150] to calibrate bonded particle (i.e. non-penetrating, hard spheres) contact model parameters for simulations involving the uniaxial compression of 2-D circular disks with elastic material properties representative of rock materials. Favier et al. [151] used DOE methods to calibrate DEM models for mixing and hopper based simulations. More recently, a rather robust work related to the use of DOE for the calibration of contact model parameters was introduced in the Ph.D. thesis by Johnstone [152], in which model parameters were calibrated for contact models related to flow. Specific DOE methods, such as the Taguchi DOE method, have been used for the calibration of bonded agglomerates by Hanley et al. [153].

There are many different DOE methods that exist and the best choice of these methods depends on the objectives of the analysis. The objective of this analysis was concerned with obtaining the proposed normal contact model input parameters that result in the best prediction of the loading, unloading, ejection, and tensile strength behavior of a real powder material—in

this case, HME copovidone. The DOE methodology chosen for the extraction of the model parameters was a responses surface methodology (RSM). A response surface design is a set of advanced DOE techniques that allows for understanding and optimizing a response. Response surface methodology is often used to refine models; especially if curvature in the response is suspected [154]. The two main types of response surface designs are the *Central Composite Design* (CCD) and the *Box-Behnken Design* (BBD). The RMS adopted in this work was the Central-Composite-Design (CCD). The difference between the CCD and the BBD is detailed in the reference [154]. The CCD was used to construct an analytical model of the DEM results as a function of the model parameters

3.5.1 The Central Composite Design Response Surface Methodology

The CCD methodology used in this work is the most commonly used response surface design and is briefly described here. CCDs are a factorial or fractional factorial design with center points, containing a group of axial points (also referred to as star points) that allow for estimating curvature of a response (i.e., nonlinearity in responses). Figure 3.10 shows a schematic of a two-parameter CCD. Each of the points shown in Figure 3.10 refer to *factor level settings* for an experimental run (in this work, a simulation run) that corresponds to a response. The factor level settings are typically defined by *coded* variables, which are variables that have been mapped from actual input parameters (referred to as *uncoded* variables) to upper, lower, central, and axial variables given by +1, -1, 0, and α respectively. By mapping input parameters from the actual input parameters to coded variables, *orthogonality* of responses may be possible. Orthogonality allows for the estimation of RS model terms independently, meaning each of the model terms' effect on a response at a given factor level can be analyzed independently from the

other terms effecting the response. To ensure orthogonality, the CCD must be *rotatable*. Whether or not a CCD is rotatable is determined by α factor level settings. The factor level setting α is the distance of each of the start points from the central points. When this factor level setting is such that the distance away from the central point results in a rotatable CCD, both orthogonality and minimization of variation in regression coefficients of the response surface models are achieved [154].

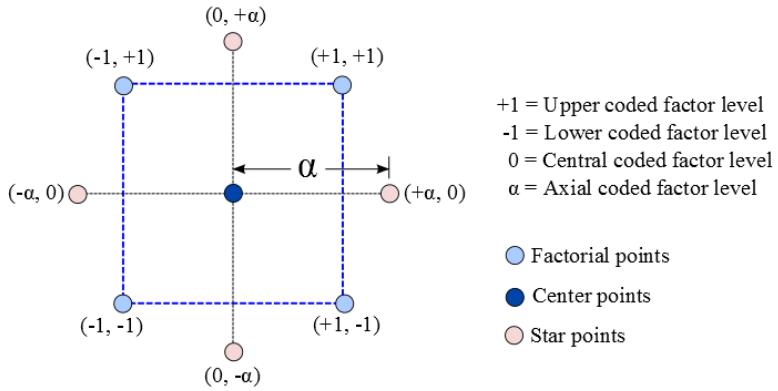

Figure 3.10 Schematic of a two-parameter central composite design

In many RSM design of experiments, the functional form of the relationships between the response and the independent variables (in this work, the model input parameters) is unknown. In order to approximate the relationship between the response y and the set of independent variables x_i, a function that considers the independent variables and interactions of these variables is typically assumed. In this work, a *second-order* model that has the ability to model curvature of the system response was considered:

$$y = \beta_0 + \sum_{i=1}^{\kappa} \beta_i x_i + \sum_{i=1}^{\kappa} \beta_{ii} x_i^2 + \sum \sum_{i<j} \beta_{ij} x_i x_j \tag{3.18}$$

The variables β_i and κ are the coefficients of the second-order model response surface and the number of input parameters respectively. While it is desirable to know the true functional relationship between the response and independent variables, the second-order approximating model will be a reasonable approximation to the response provided the solution domain of interest for each of the *n* variables is not too extensive. The method of least squares regression is used to estimate the coefficients of the response surface given the outcome of responses that are generated at each of the factor levels. Once the coefficients are determined, the resulting second-order model constitutes a response surface, which allows for a further analysis using the fitted surface.

The objective of many RSMs is to use the fitted surfaces as a means of obtaining the input parameters that result in an *optimum response* that produces a best fit to experimental results. Optimization consists of maximizing, minimizing, or targeting a response by systematically choosing input values from within an allowed set (factor level settings) and computing the value of the function. In general, optimization in RSM involves finding the "best available" values of an objective function (second-order response surface model) given the defined factor level settings subject to constraints. This type of optimization problem is referred to as constrained optimization or *nonlinear programing methods* [154, 155]. The general minimizing nonlinear program optimization problem for multiple responses is given by

$$\min \left\| y_n - y_m^* \right\|$$
$$\text{Subject to contraints on } y_m \tag{3.19}$$

where y_n and y_m, are the objective functions corresponding to the n^{th} and m^{th} response. The value of y_n^* represents the actual experimental value. The optimization given by equation (3.19) is solved using iterative procedures.

Another approach to optimization of multiple responses is the optimization technique developed by Derringer and Suich [156] and is the approach adopted in this work. This approach uses *desirability functions*, which are functions that are used to convert each response y_n into an individual desirability function d_n. The range of d_n can vary from zero to one, where $d_n = 1$ is most desirable and $d_n = 0$ is least desirable. To obtain the set of input parameters x_i that represents the optimum response, an overall desirability in terms of multiple responses is computed by the geometric mean of individual responses that produced a value closest to one:

$$\bar{D} = (d_1 \cdot d_2 \cdot \ldots \cdot d_n)^{1/n} \tag{3.20}.$$

When the target of the response is to minimize the difference between the response y_n and the experimental value y_n^*, the individual desirability d_n is computed by

$$d_n = \begin{cases} 1 & y_n < T_n \\ \left(\dfrac{Up - y_n}{Up - T_n} \right)^w & T_n \le y_n \le Up \\ 0 & y_n > Up \end{cases} \tag{3.21}$$

where $T_n = \left\| y_n - y_n^* \right\|$, Up = upper limit found from all runs, and w = weight. To obtain an individual desirability closest to one, an iterative procedure is used by systematically changing the independent variables x_i until a response corresponding to the highest desirability is obtained. When $w > 1$, more emphasis is placed on hitting the target, whereas, less emphasis is placed on hitting the target when $0 < w < 1$. Computations of desirability in this work used a weight $w = 1$, which gave equal emphasis on hitting the target for all responses.

3.5.2 Response Surface Generation using the CCD

The CCD was used to generate analytical functions for the responses considered from macroscopic experimental data obtained from two experiments—specifically, die compaction experiments using an instrumented die and diametral compression strength tests. The CCD analysis performed in this work was facilitated by the use of the commercial software Minitab 17 ®. For the six-parameter proposed contact model, two CCDs were employed. The treatment of response surface generation by two CCDs rather than just one was justified on the basis that the parameters λ and C that define the tensile forces at contacts had negligible influence on simulation responses in loading and the beginning stages of unloading. For a number of simulation runs, it was found that less than 2% of contacts were in a tensile state during loading of the pressed particle assembly—a result also found in the work conducted by Pizette et al. [157] on the compaction of powders using the DEM. During unloading, there would surely be contact forces in a tensile state; however, unloading slopes were defined in terms of the very beginning stages of the compaction (see inset of Figure 3.2(b)) where cohesion at the contact

plays only a minor role. Thus, response surface generation for loading and unloading from simulation results was assessed independently from tensile test simulation results. Responses pertaining to loading and unloading were achieved using experimental results obtained from die compaction experiments, whereas the latter was achieved using diametral compression strength tests. Note that the interaction parameter F was fixed to a value of 0.18 for all simulations performed. The two CCDs were employed as follows:

1. Loading-unloading CCD to generate response surfaces in terms of $k_1, \hat{k}_2/k_1$, and θ that have a dominant influence on loading and unloading. Interparticle coefficient of friction μ was also included as a model parameter in this CCD as it had a substantial effect on simulation responses.
2. Tensile strength CCD to generate response surfaces pertaining to the parameters λ and C that influence tensile strength results.

For loading and unloading, the CCD was used to generate response surfaces as a function of the four model input parameters discussed above from compaction simulations performed on 3000 particle systems compacted to 98% RD. The four-parameter CCD required 2^4 factorial runs + 8 start point runs + 1 center point run = 25 total runs, which resulted in approximately 33 hours of total simulation time. The results obtained from the CCD runs were then used to create response surfaces, where the responses of interest in this work were the plastic and elastic strain energies given by

$$U_P = RD_0 \int_{0.6}^{0.98} \sigma d(RD)$$
$$U_E = \frac{1}{2} RD_0 \sigma \left(0.98 - RD_u\right) \quad (3.22).$$

The responses U_p and U_E are the plastic and elastic strain energies respectively with respect to relative density—thus, the reason for the appearance of RD_0 in equation (3.22). The relative density RD_u was the relative density calculated from unloading slopes as shown in Figure 3.11. Figure 3.11 shows a schematic of an ideal matching of strain energies for axial stress (Figure 3.11(a)) and radial stress (Figure 3.11(b)) between experimental and a DEM simulation. From Figure 3.11, it can be seen that the expectation of a perfect match is not possible due to the fact the 3000 particle system possess an initial relative density RD_0 = 0.6 as opposed to an initial relative density RD_0 = 0.46 for copovidone powder. Nevertheless, the aim of the loading-unloading CCD analysis was to obtain the optimum input parameters that minimized results between the strain energy results from DEM simulations and experimental results, specifically the goal was to obtain the responses y that satisfied the targets $T = \min \left\| U - U^* \right\|$ for both axial and radial stress versus relative density by employing the optimization procedure given by equations (3.20 and 3.21).

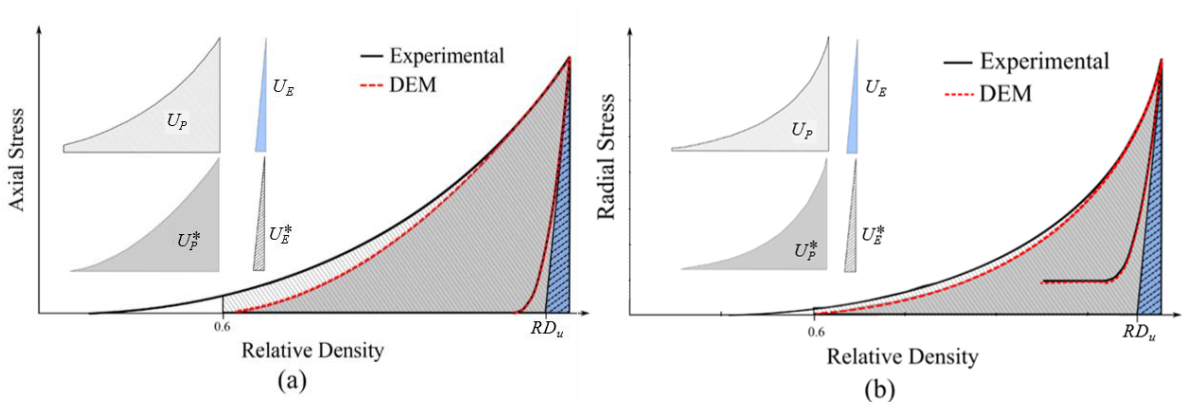

Figure 3.11 Schematic of response for plastic and elastic strain energies compared to experimental plastic and elastic strain energies for (a) axial and (b) radial stress versus RD

The tensile strength CCD analysis was used to generate response surfaces as a function of the the two input parameters λ and C from tensile test simulations performed on 3000 particle systems. Tensile test simulations were performed for particle assemblies compacted to in-die relative densities of 75%, 85% and 98%. The number of simulations required for the two-parameter CCD analysis was equal to 2^2 factorial runs + 4 start point runs + 1 center run = 9 total runs per each relative density compaction. Thus, the total number of runs was equal to 27, which resulted in approximately 43 hours of total simulation time. From the 27 total runs, three response surfaces were generated for the three different relative densities. The responses of interest in the tensile strength CCD analysis were the tensile strength measures from each of the simulations. The tensile strength was calculated according to the following equation:

$$\sigma_T = \frac{P_f}{A} \tag{3.23}.$$

where P_f was the maximum attainable force in the simulation and A the area of the punch surface. The aim of this analysis was to obtain the optimum input parameters that minimized results between the response σ_T from simulation and the measured tensile strength of copovidone powder compacts σ_T^*. Thus, the optimization of the input parameters were achieved by obtaining responses y that satisfied targets $T = \min\left\|\sigma_T - \sigma_T^*\right\|$. It is important to note that the tensile strength measure from diametral compression tests performed on the copovidone compacts is not exactly the tensile strength that would be measured using uniaxial tension tests as depicted in Figure 3.7(e). It is expected that microcracking in the prior compaction direction and the elongated pressed particle morphologies in the direction parallel to the prior compaction direction—an observation discussed in Chapter 2—would result in different strength measures between the two tests. In other words, strength anisotropy may be possible. In this work, axial tension test simulations were chosen as a compromise between a more manageable simulation set-up and reduced computational time as opposed to a more difficult simulation set-up and larger expected CPU time for diametral compression strength testing.

For both loading-unloading and tensile strength CCDs, it was important to ensure that the input parameters for different factor level settings existed over a large enough solution domain to produce simulation responses that encompassed experimental values of interest. Table 3.2 lists the coded to uncoded factor level settings used for the loading-unloading CCD. The values corresponding to the input parameter $k_1 = 3\pi c^2 \sigma_y R$ were obtained from defining the following yield strengths: σ_y = 25 MPa, 27.5 MPa, 30 MPa, 32.5 MPa and 35 MPa. Table 3.3 lists the coded to uncoded factor level settings for the tensile strength CCD. For both CCDs, α factor level settings result in rotatability and orthogonality.

Table 3.2 Coded to uncoded factor level setting for loading-unloading CCD

Microparameters	Coded to uncoded factor levels				
	-2	-1	0	1	2
k_1 [kN/m]	34.16	37.58	41.00	44.41	47.83
$\hat{k}_2/k_1$	25	30	35	40	45
q	0.275	0.3	0.325	0.35	0.375
r	0.05	0.1	0.15	0.2	0.25

Table 3.3 Coded to uncoded factor level setting tensile strength CCD

Microparameters	Coded to uncoded factor levels				
	-1.414	-1	0	1	1.414
λ	0.05	0.087	0.175	0.263	0.3
C	0.50	0.573	0.75	0.927	1

It was necessary that simulation responses from the different factor level settings resulted in $L \le y_n^* \le Up$, where *L* and *Up* represents the lower and upper limit responses from all runs. To ensure that the solution domain resulted in responses that included the measured values within the upper and lower limit responses, factorial runs were completed first. Then, the upper and lower limit responses for each of the response variables were determined. If it was found that the measured values fell outside the upper *Up* and lower *L* limits, the solution domain would then need to be increased. The upper limit responses *Up* and lower limit response *L* for the CCDs are given in Table 3.4. For the chosen factor level setting, it was found that all upper and lower limit responses encompassed the experimental measures for each of the responses as shown in Table 3.4.

Table 3.4 Upper and lower limit responses

Response Variables	*Up* [MJ/m^3]	*L* [MJ/m^3]	Experimental [MJ/m^3]
U_p (Axial)	30.84	18.03	21.67
U_p (Radial)	17.29	10.41	11.07
U_E (Axial)	4.99	1.16	2.07
U_E (Radial)	6.01	1.17	1.98
	Up [MPa]	*L* [MPa]	Experimental [MPa]
σ_T (98% RD)	6.23	0.87	2.39
σ_T (85% RD)	3.08	0.31	1.10
σ_T (75% RD)	1.19	0.08	0.50

3.6 Results and Discussion

DEM simulations were conducted using the factor level settings listed in Table 3.2 and Table 3.3. First, simulations pertaining to loading, unloading, ejection, and tensile strength were conducted to obtain the input parameters associated with the CCD analyses. The response variables were then calculated and the optimization procedure discussed above was employed to obtain the optimum parameters that result in a best fit to experimental results. The targeted responses and their associated desirability values, along with the optimized input parameters are given in the CCD analysis output displayed in Table 3.5. The fitted response surface functions acquired in the CCD analysis are given in Appendix B. One thing to notice from the CCD analysis results given in Table 3.5 is the close matching of the DEM responses using the proposed contact model. From the values listed in Table 3.5, it can be seen that there is only a

slight deviation between plastic strain energies, which was to be expected due to the fact that the initial relative density of the DEM particle assembly starts at a greater value than the copovidone powder. Deviations are also noted for the targeted tensile strength measures. However, these differences are relatively small and can be considered satisfactory.

Table 3.5 Optimization of input parameters

	Axial $\min\|U_p - U_p^*\|$	Radial $\min\|U_p - U_p^*\|$	Axial $\min\|U_E - U_E^*\|$	Radial $\min\|U_E - U_E^*\|$	98% RD $\min\|\sigma_T - \sigma_T^*\|$	85% RD $\min\|\sigma_T - \sigma_T^*\|$	75% RD $\min\|\sigma_T - \sigma_T^*\|$
Target	0	0	0	0	0	0	0
Response	0.0014	0.1949	0	0	0.0592	0.087	0.0425
Desirability	0.9993	0.9687	1	1	0.9843	0.9561	0.8996
Input Parameters	k_1 [kN/m]	$\hat{k}_2/k_1$	q	n	λ	C	
Optimized Result	35.06	37.06	0.323	0.21	0.187	0.895	
	Composite Desirability = 0.9921				Composite Desirability = 0.9406		

Taking advantage of the analysis results given in Table 3.5, the proposed contact model parameters were identified and allowed for the matching of DEM results to the experimental results for the compaction of copovidone powder compacted to in-die relative densities of 98%, 85%, and 75%. Figure 3.12(a-b) shows the comparison of the optimized DEM results and experimental results for the evolution of axial and radial stress as a function of relative density. Observation of the radial unloading curves revealed a deviation between numerical and experimental results. This discrepancy was assumed to be due to the assumption of a linear unloading-reloading stiffness at the contacts in the proposed contact model. It was realized that a

nonlinear unloading may represent a more realistic description of the force-displacement behavior of contacts; however, Figure 3.12 shows that the use of the CCD methodology provides a satisfactory matching of the experimental results with this one exception.

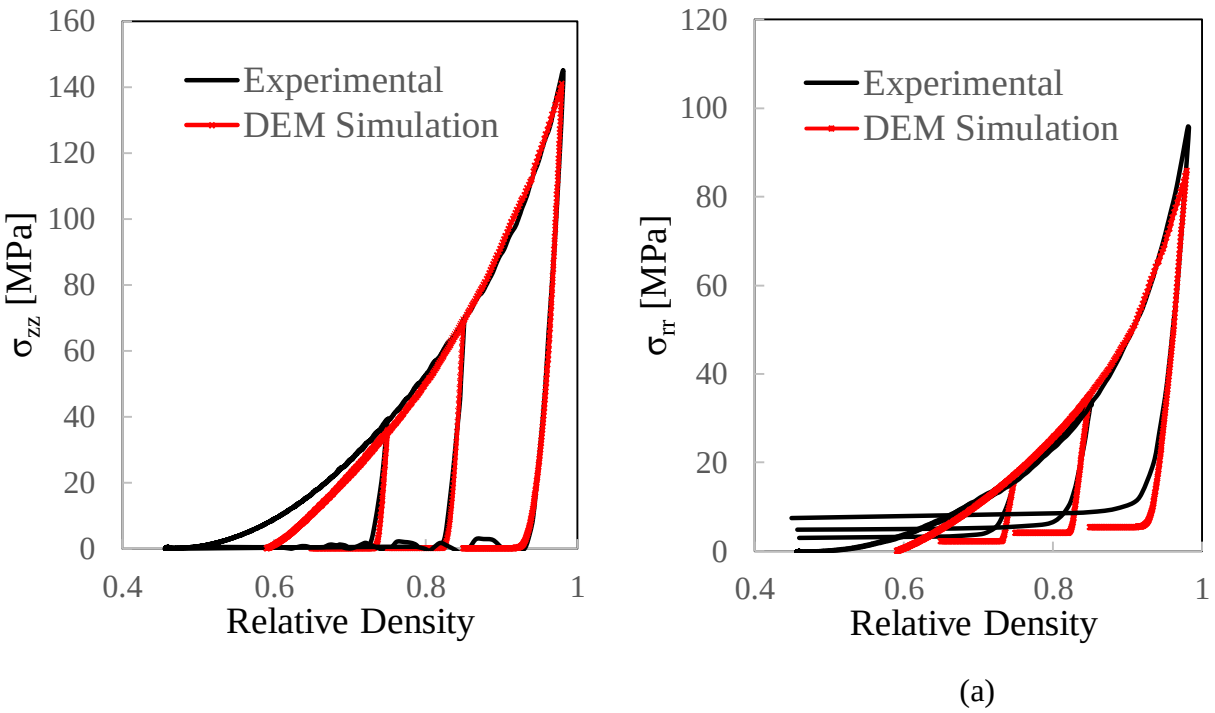

(a)

Figure 3.12 Optimized DEM simulation results compared to experimental results for the evolution of axial stress (a) and radial stress (b) as a function of relative density

An important observation made for the results presented in Figure 3.12(b) was the nonlinearity in unloading and the predicted level of residual wall stress σ_R for each of the relative density compactions. When it is assumed that the stress within a compact is uniform at the end of compaction and the powder material behaves linear-elastically during unloading, the residual wall stress can be calculated using the condition of no strain in the radial direction, $\Delta\varepsilon_{rr} = 0,$ by

$$\sigma_R = \sigma_{rr}^{\max} - \frac{\nu}{1-\nu}\sigma_{zz}^{\max} \tag{3.24}$$

where the r and z subscripts indicate the radial and axial directions and ν is Poisson's ratio of the material. The superscript max indicates values at maximum load. The result of the calculation given by equation (3.24) for the compaction of copovidone is the linear elastic prediction of residual wall stress shown in Figure 3.13(a) using Poisson's ratios found in the work conducted by Garner et al. [29] for each of the relative densities considered. Clearly, this calculation over predicts the true level of residual wall stress also shown in Figure 3.13(a). The nonlinearity in unloading is an indication of inelastic phenomena (i.e., microcracking) that has taken place during the unloading. It was suggested in Chapter 2 that the inelastic phenomena, which can be assumed to be dominated by microcracking, is related to the level of interparticle cohesion, the level of maximum wall stress at the end of loading, and the stored energy in the compact. If the combination of the stored elastic strain energy at contacts and wall stresses applied to the entire compact are sufficient to of overcome cohesion between particle contacts, the result is a relief of radial wall stresses. Therefore, the level of residual wall stress should reflect the level of cohesion between particle contacts. Figure 3.13(b) shows the comparison of the predicted tensile strength using the optimized parameters given in Table 3.5 and experimental results. Fairly good agreement between the predicted tensile strength and experimental results is observed. The predicted level of residual wall stress at each relative density compaction shown in Figure 3.13(a) shows reasonable agreement compared to experimental results. This reasonable agreement between the predicted residual wall stress and experimental results was assumed to predominantly the effect of the parameters that characterize the level of cohesion at the contacts.

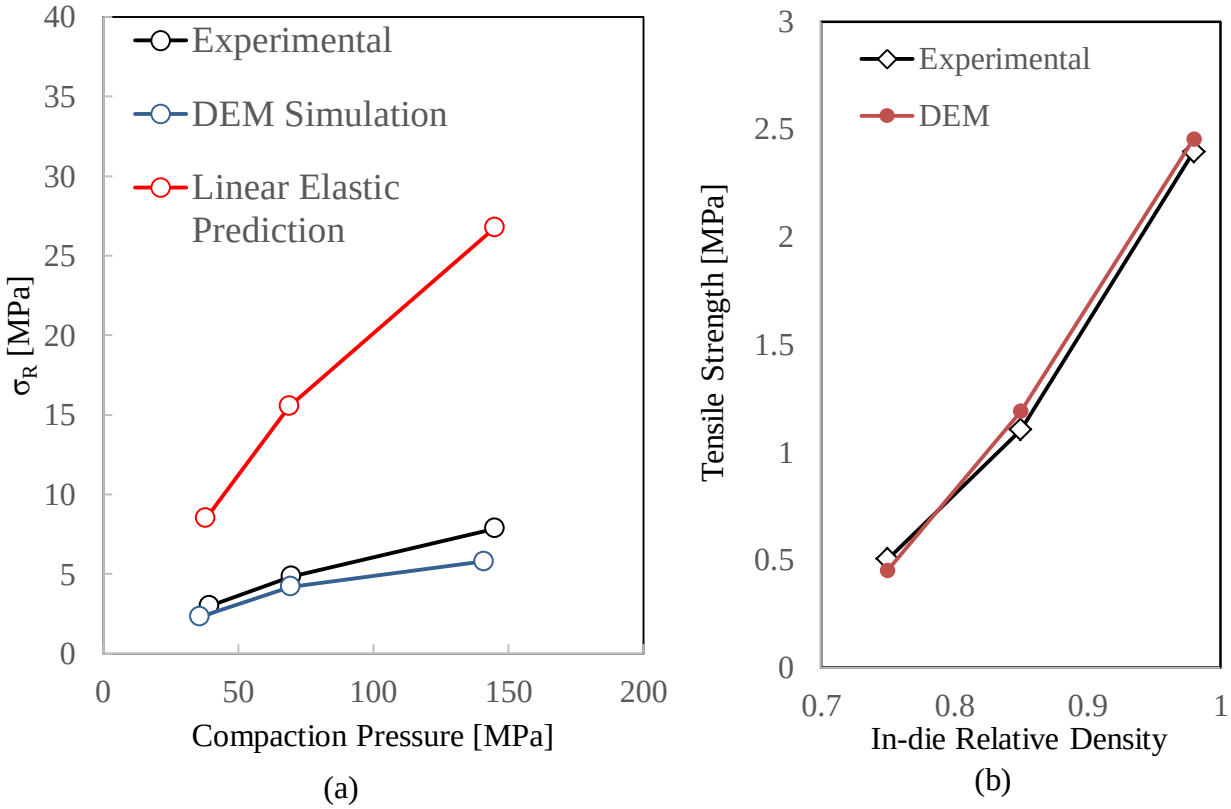

Figure 3.13 Comparisons of (a) residual wall stress for a linear elastic prediction, experiment, and DEM prediction, and (b) tensile strength for experiment and DEM prediction.

3.6.1 Connection between Particle Contact Cohesion and Residual Wall Stress

To further expound upon the connection between particle contact cohesion and the level of residual wall stress that exists after complete unloading, a study that considered the compaction of microcrystalline cellulose (Avicel PH102) with and without lubricant was conducted. The lubricant used in this study was magnesium stearate (MgSt). Parameter sensitivity studies of DEM simulations generated in the CCD analyses were used to gain a deeper understanding of the connection between residual wall stress and tensile strength observed experimentally. The negative effects of MgSt on strength of compacts have been

known widely in the pharmaceutical industry [158]. To this author's knowledge, there has not been a study that has considered the effect of MgSt on residual wall stress and the connection to tensile strength.

For compaction of MCC with MgSt, a powder blend consisting of 1% MgSt was produced. The MCC-1% MgSt mixture was blended using a Turbula Shaker-Mixer (GlenMills, Clifton NJ) for 20 minutes at 45 revolutions per minute to ensure optimum MgSt coating of MCC particles. It was assumed that compaction behavior in loading of the MCC-MgSt blend was not significantly affected by the presence of the relatively small amount and small particle size of MgSt relative to MCC in the mixture—an assumption confirmed in the work conducted by Zuurman et al. [158]. Instead, it was assumed that only the cohesive properties were affected. Therefore, the particles that constitute the MCC-1% MgSt blend can be thought of as just MCC particles with lower cohesive properties. A range of relative density compactions from approximately 70% RD to 85% RD were performed using a Huxely Bertram compaction simulator with an instrumented die, and tensile strength of compacts were assessed using diametral compression testing.

Figure 3.14(a-b) shows the residual die wall stress and tensile strength measurements for MCC powder with and without lubricant. From Figure 3.14(a), it can be seen that the MCC-1% MgSt blend consistently produced a lower level of residual wall stress for each relative density compaction compared to the MCC compactions without lubricant. Similarly, Figure 3.14(b) shows lower tensile strength measurements for the MCC-1% MgSt blend compared to the MCC powder with no lubricant added. It can be seen from Figure 3.14 that the presence of lubricant causes a strong decrease in compact tensile strength and a relatively small, but statistically significant, decrease in residual wall stress.

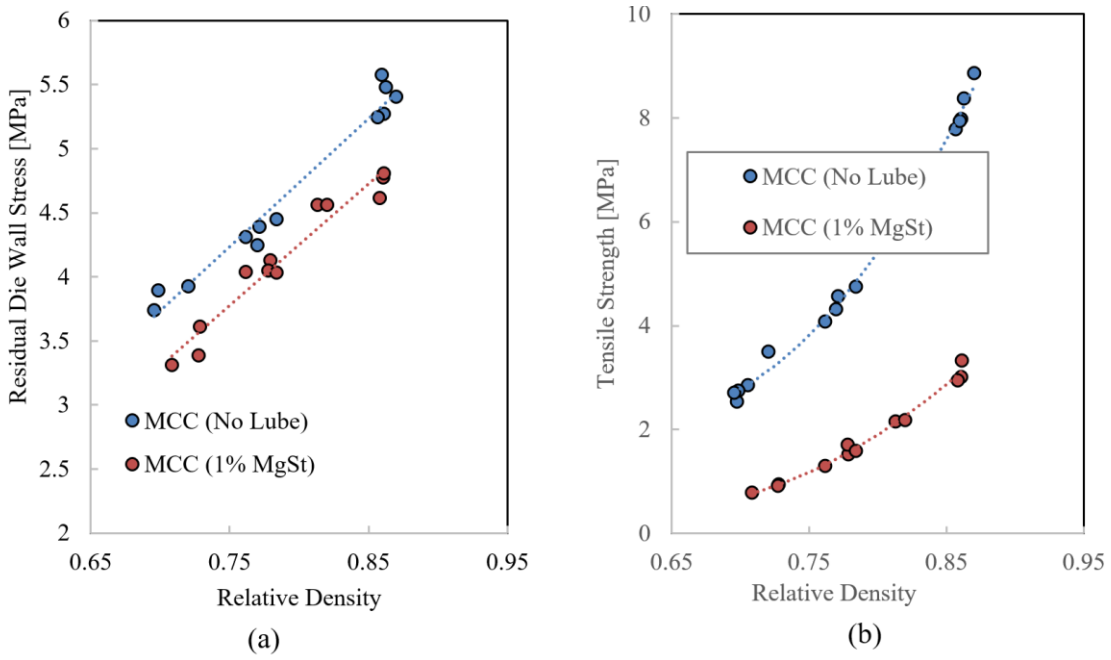

Figure 3.14 Comparison of (a) residual die wall stress and (b) tensile strength between MCC with and without 1% MgSt.

The lower tensile strength measurements for MCC-1% MgSt compacts compared to MCC compacts containing no lubricant were consistent with the findings of Zuurman et al. [158]. In their work, they suggested that the cause for the lower tensile strength of MCC-1% MgSt compacts was due to the increase in relaxation (also referred to as spring back) due to the reduction of interparticle bonding from the lower cohesive properties. A parameter sensitivity study Figure 3.15 of the effect of the cohesive parameter on tensile strength and percent spring back tends to confirm this idea, where percent spring back is defined by change in the thickness of the compact from the end of loading to the end of complete unloading:

$$\%SB = \frac{\Delta H}{H_0} \times 100\% \tag{3.25}$$

where ΔH is the change in the thickness of the compact, and H_0 is the thickness of the compact at the end of loading. Figure 3.15(a) shows predicted DEM results of normalized radial wall stress and percent spring back for different levels of the cohesive parameter λ. There is noticeable effect of decreasing interparticle cohesion on the level of residual wall stress and the cooresponding percent spring back in which it can be seen that as the interparticle cohesion is decreased, the level of the residual wall stress is decreased and the percent spring back is increased. The connection between residual wall stress and interparticle cohesion can be seen in Figure 3.15(b), which shows that decreasing interparticle cohesion results in a weaker compact. This result is in line with some of the findings presented in the work on the mechanisms of microcrack formation discussed in Chapter 2. While the work in Chapter 2 did not consider the effect of interparticle cohesion, it was found that the connection to radial wall stress and the degree of microcracking was related to a decrease in microcracking when the level of residual wall stress was gradually released in tapered die ejections. This result indicates that as the interparticle cohesion is reduced, there is a greater degree of contact opening, which tends to relieve some of the residual wall stress.

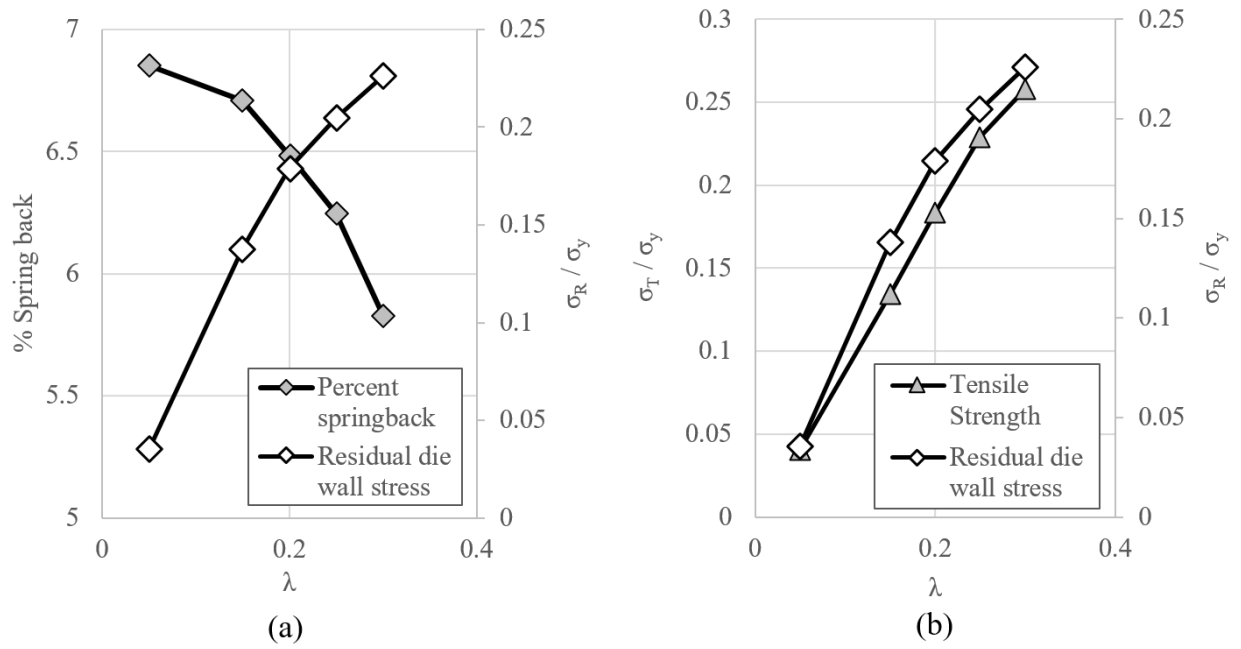

Figure 3.15 DEM predictions of (a) normalized residual wall stress and percent spring back and (b) normalized residual wall stress and normalized tensile strength for varying levels of the cohesive parameter λ. With the exception of λ, the DEM normal contact model parameters for these results are given in Table 3.5.

3.6.2 Effect of Particle Packing on Tensile Strength

It has been commonly known for quite some time that cohesion between contacting particles is strongly influenced by inpterparticle contact area [65, 100, 159]. For powder materials, not only does the cohesive properties defining the level of cohesion at individual contacts influence the strength of compacted powders, but also the total number of contacts and the corresponding contact areas that exist to form the complex network of bonds capable of transmitting tensile stresses. A study that considered DEM simulations and compaction of MCC

(Avicel PH102) for the compaction of *loose* and *close* packings was conducted to understand how the initial die fill configuration affects strength. It was hypothesized that the maximum achievable close packing of particles would result in a larger evolution of particle contacts in compaction compared to initially loose packings, and consequently higher tensile strength due to the larger number of expected contacts (i.e., higher coordination number *Z*).

Many factors can affect the evolution of coordination number in the compaction of powders in a die. Interparticle friction is one such factor that has been extensively studied in simulations of powder compaction [45, 53, 110, 157, 160]. It was first found by Rendanz and Fleck [45], and later confirmed by many researchers, that increasing interparticle friction significantly affects rearrangement of particles—predominantly in the beginning stages of compaction and less so in the later stages. Procopio and Zavaliangos, in their work of the compaction of particles using the MPFEM (see Chapter 1, section 1.1), found that the effect of interparticle friction on macroscopic stress results diminishes as densification is increased. Thus, it was expected that loose packings of frictional particles would result in an overall reduced evolution of *Z* as opposed to close packings, but would become less apparent at higher densities. Figure 3.16 shows the effect of friction on the ratio of maximum radial stresses to maximum axial stresses, $K = \sigma_{rr}^{\max} / \sigma_{zz}^{\max}$ and normalized tensile strength for a compaction to 98% in-die RD. The stress ratio *K* can be considered a predictor of anisotropy in the compact. As such, lower values of *K* corresponds to a larger number of contacts oriented in the axial direction than in the radial direction. The effect of friction on *K* signifies less rearrangement of particles with increasing friction, which translates into less lateral movement of particles in the beginning stages of compaction. The result of this hindrance of lateral movement means that the larger number of contacts oriented in the axial direction can transmit higher tensile stresses before

failure. The result shown in Figure 3.16 is a verification of the idea that producing a larger number of contacts should results in a larger strength.

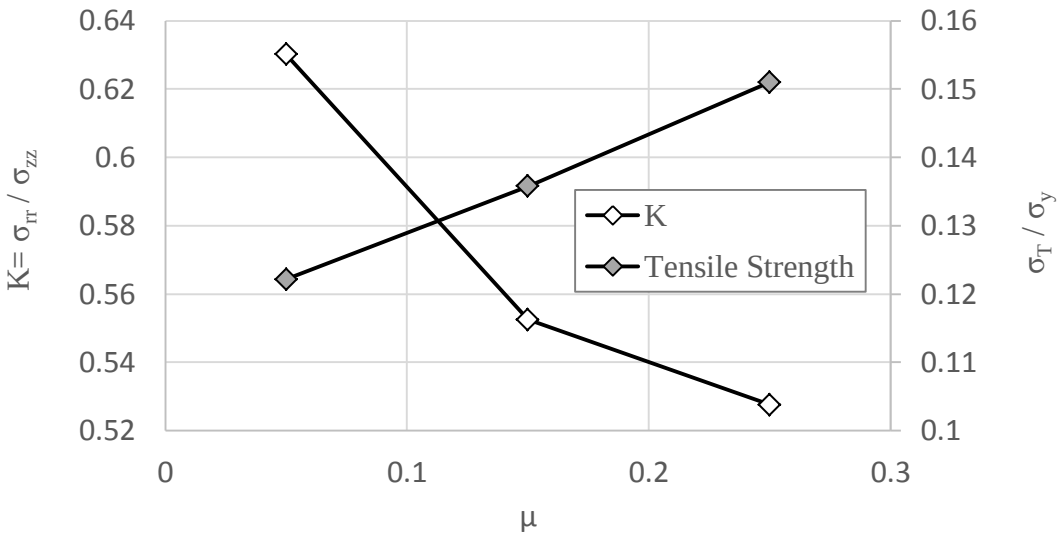

Figure 3.16 Effect of friction on the K-ratio and tensile strength. With the exception of interparticle friction, input parameters used to generate this result were given by the values listed in Table 3.1

To study the effect of initial die fill conditions and their relationship to tensile strength compactions of close and loose packings of MCC were conducted. By *loose packing*, it is meant that powder was simply poured into the die and any excess material above the die was scraped off to produce a maximum height equivalent to the height of the die. *Close packing* was achieved by first pouring the powder into the die and then subsequently placing the assembly shown in Figure 3.17(a) on Vortex mixer (VWR, Randor PA) shown in Figure 3.17(b) at maximum vibration speed until the powder bed no longer decreased in final height—typically less than ~ 10 seconds). The result of the procedure used to obtain the close packed configuration was an increase in the initial relative density of approximately 0.21 to

approximately 0.32. The powder bed height decreased by approximately 5 mm from an initial die fill height of 17 mm (see Figure 3.17(a))

Tensile strength measurements for compacts compacted to 70%, 80% and 90% RD were conducted for loose and close packings. Figure 3.18(a) shows the results for tensile strength measures between initially loose and close packing of MCC compacts. From this figure it is seen that as the relative density is decreased, the difference between the tensile strength becomes larger. For the 90% RD compaction, the tensile strengths are nearly equivalent, which suggests that the influence from the initial configuration diminishes. At higher densities, it is assumed that the particles experience significant plastic deformation that resulted in plastic flow of the material into the available void spaces of both the initially loose and close packed die fills. Thus, the difference between the particle morphologies as high densities are approached should become less apparent. At lower densities, the particle morphologies should exhibit some of the initial characteristics of their respective initial configurations.

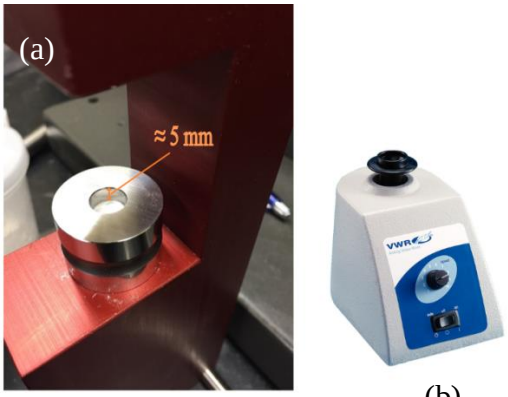

Figure 3.17 (a) Punch and die assembly, which shows a decrease in the powder bed height after placing assembly on (b) vortex mixer at maximum vibration speed until powder no longer decreased in final height

DEM simulations for the compaction of initially loose and close packed configurations were conducted to both verify the hypothesis that the maximum achievable close packing of particles would result in a larger evolution of particle contacts in compaction compared to initially loose packings, and consequently higher tensile strength due to the larger number of expected contacts, and the ability of the DEM to predict the behavior of tensile strength as a function of the initial configuration shown in Figure 3.18(a). The loose initial configuration was defined as being the initial configuration generated in the particle number convergence study discussed in section 3.4 of this chapter. A close packing was obtained by first pre-compacting the loose packed configuration to compacting pressure of approximately $\sigma_{zz} / \sigma_y = 0.22$ and then allowing the particle system to equilibrate until the kinetic energy of the system was significantly lower than the potential energy by at least 5 orders of magnitude. The particle assembly was then unloaded and allowed to equilibrate in a similar manner to the initial pre-compaction step. At this point, the coordination number *Z* increased from approximately 4.5 in the loose packed initial configuration to approximately 5.2 in the close packed configuration. The initial relative density increased from approximately 60% RD to approximately 62% RD. It is important to note that a true close packed configuration for a monosized assembly of spherical particles should be equal to 0.64. However, as Onoda et al. [161] has concluded, wall effects for particles systems for which the container radius is less than 200 times the particle radius results in a less-than-perfect particle packing.

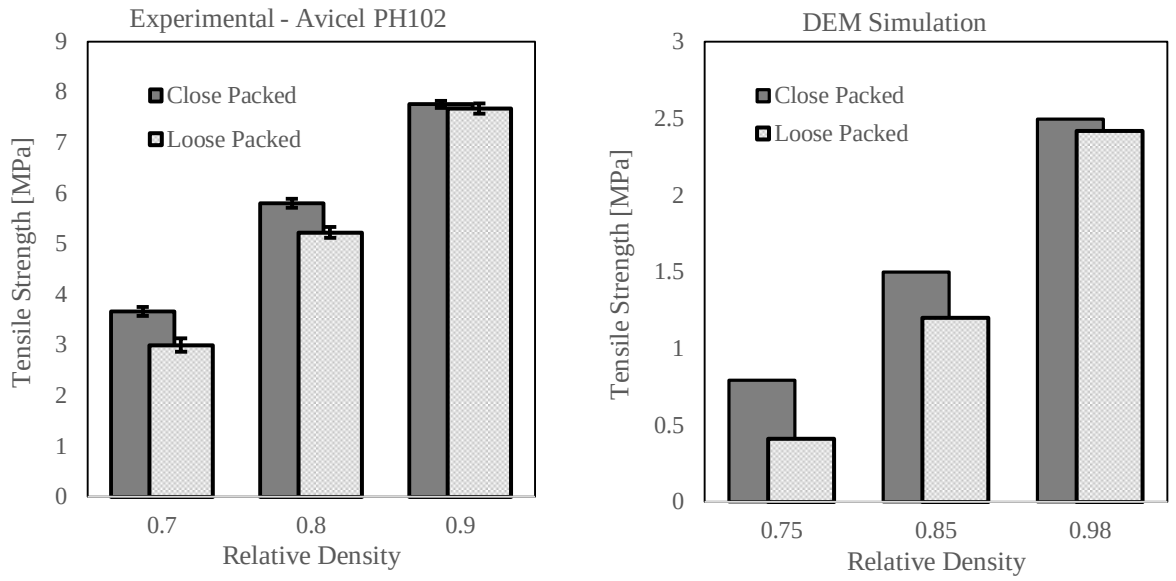

(a)

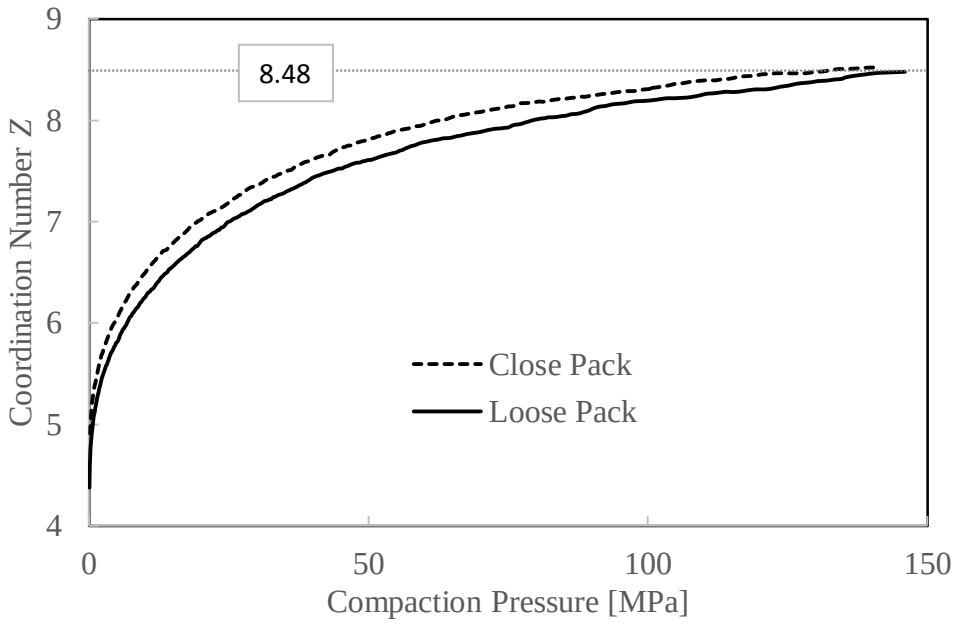

(c)

Figure 3.18 Comparison of tensile strength for (a) loose and close packings of MCC and (b) DEM predictions of tensile strength for initially loose and close packings configurations. A comparison of (c) the coordination number *Z* for the initially loose and close packings was also assessed. For the initially loose and close packings of MCC compactions, tensile strength for ten tablets per relative density were measured. The error bars represent the error based on a 95% confidence interval.

Figure 3.18(b) shows the comparison of tensile strength between initially loose and close packed initial configurations for relative density compaction of 75%, 85%, and 98%. From Figure 3.18(b), it can be seen that behavior of the evolution of tensile strength with density produced a nearly identical behavior as experiment. The idea that a close packing of particles would result in a larger evolution of coordination number *Z*—the result of which would correspond to an increase in tensile strength compared to tensile strengths of an initially loose packed compacts—can be seen Figure 3.18(c). This figure shows the evolution of *Z* for initially loose and close packed configurations. It can be seen that at almost all compactions pressures the coordination number is larger for the close packed initial configuration case. It is only when higher compaction pressures are reached that the coordination numbers become nearly equivalent. This near equivalence at higher compaction pressures explains the nearly equal tensile strengths that are obtained for higher compaction pressures pertaining to the 98% in-die relative density.

3.7 Conclusion

The work presented has shown the potential of DEM in simulating the compaction of powder materials. A contact model that can approximate the behavior of powder particles subjected to compressive and tensile forces in high relative density simulations of die compaction was introduced. The formulation of the proposed contact model took a heuristic approach to modeling the pressing of powders to high density. Although the approach was an approximation to the real behavior of contacting particles, results from this work have shown the ability of this model to predict and capture the behavior of powders in the compaction process.

The present work dealt with procedures related to the calibration of DEM contact models where it was shown that fairly good agreement between experiment and DEM simulation results were obtained. One of the key advantages of the calibration procedure is the need for only two experimental techniques: die-compaction, and axial tension tests. The calibration procedure incorporated the central composite design (CCD) of experiments. From the CCD analyses, it was found that the use of the optimized parameters in the proposed contact model resulted in a reasonable approximation of the residual wall stresses for each of the relative density compactions considered. The connection of the residual wall stress to the level of interparticle cohesion was explored. It was found that residual wall stress is connected to tensile strength and may possibly represent a good predictor of strength in compacts. Further studies should be conducted to assess whether or not this assertion is correct. The effect of the initial configuration on tensile strength was also explored. It was found that the DEM prediction using the proposed contact model resulted in excellent prediction of the tensile strength behavior as a function of relative density shown in the experimental evaluation of initially loose and close packed configurations.

It should be noted that DEM work only considered the compaction, unloading, ejection, and tensile strength of monosized assemblies of particle systems. As such, the matching of DEM results using the calibration procedure discussed above for the real powder system (HME copovidone powder), which certainly is not a monosized assembly of spherical particles, was meant to show the power of the calibrating procedure as a method for the extraction of DEM contact model parameters. It is felt that further studies should be conducted that include both a particle size distribution and particles possessing different properties. Perhaps, one negative attribute of the calibration procedure was the large number of runs necessary to properly obtain

the parameters of the proposed contact model used in this work. Ideally, a contact model that takes as its inputs intensive material properties (e.g., yield strength, modulus of elasticity, surface energy, etc...) is more desirable than the use of extensive properties such as stiffness. However, it is this author's opinion that until the issue of particle shape can be handled properly (i.e., DEM uses spherical particle, which practically do not exist), the best approach to obtaining the parameters of contact models is by statistical approaches for the matching of real powder systems.

Chapter 4: On the Damage and Strength in Powder Compacts: A Discrete Element Method Assessment of Damage

4.1 Introduction

Many studies have confirmed the ability of DEM model implementations to capture the inherent fundamental features of granular materials (e.g., strain localization, path dependence, and anisotropy). However, the majority of DEM work has been relegated to powder flow, shearing of granular media, and compaction of granular media related to geomechanics problems. Only a few works have considered the use of the DEM as a tool to study the mechanical behavior as it pertains to damage and the effect this damage has on strength of pressed powders in the compaction process. The DEM work by Martin et al. [48-50, 80, 81] was pioneering with respect to strength of compacted powders (see Chapter 1, section 1.3) subjected to various loading conditions for powders compacted using periodic boundary conditions. Building on the work of Martin et al., this work considers the DEM analysis of damage and strength of ejected die compacted powders from rigid dies. While periodic boundaries have been used extensively in DEM simulations involving flow, shearing, and compaction of powders, predictions of damage and the effect this damage has on strength using periodic boundaries produces a *global* or isotropic prediction. In general, the microstructural evolution of powder particles in the compaction process produces a heterogeneous solid compact at the end of loading. The effect of this heterogeneity results in complex failure modes under various local loading conditions. As such, it is felt that simulations of compaction using die walls is more representative of real problem.

The goal of this study is to assess the mechanical behavior of powder compacts in terms of damage and the effect this damage has on the evolution of strength in the compaction process by

utilizing the discrete element method. From Chapters 2 and 3, it was found that connection between the level of residual wall stress and the properties that characterize the cohesive properties at the contact existed. Damage as it pertains to residual wall stress was also considered in this study. Finally, simulations involving the compaction of powder particles in straight and tapered dies were considered for the purpose of assessing the ability of the adhesive, elastoplastic normal contact model introduced in Chapter 3 to adequately predict the behavior observed in Chapter 2 regarding the experimental evaluation of these two cases.

4.2 Damage Mechanics: a Discrete Perspective

From the point of view of the physical nature of defects, damage is always related to plastic or irreversible strains on the mesoscale, or on the microscale—the scale of discontinuities such as microcracks. In describing damage of particulate media using the DEM, perhaps one of the simplest methods to assess the degree of damage is by counting the number of debonded particle contacts that have occurred from an initial undamaged state of a material to some later state of the material that has been subjected to some externally applied forces. By counting the number of contact surface separations and dividing by the initial number of contacting particles in the undamaged state, the damage variable, referred to as D_1 in this text, is given by

$$D_1 = \frac{N_L}{N_I} \tag{4.1}$$

where N_L is the number of contacts that have separated from state 1 to state 2, and N_I the initial number of contacts. In this work, a debonded contact was considered to have occurred when the

normal deformation $\delta_n < \delta_b$ (see Chapter 3, Figure 3.3). From this definition of damage, it can be understood that a value of $D_1 = 0$ corresponds to the undamaged state, whereas, $D_1 = 1$ corresponds to a state where every initial contact has separated. Although the damage variable given by equation (4.1) provides a meaningful description of damage as it relates to generation of discrete cracks, it does not provide any information regarding the nature or severity of these cracks, or the level of damage related to the available contacts that are able to transmit tensile forces.

For crack distributions in isotropic, brittle or quasi-brittle materials where microcavities or microcracks exist, a damage variable that is physically defined by the surface density of microcracks lying on a cutting-plane of material body has been used extensively in the field of continuous damage mechanics [86, 162-164]:

$$D = \frac{A - \tilde{A}}{A} \tag{4.2}$$

In equation (4.2), A and $\tilde{A}$ are the overall cross section of a material body containing microvoids or microcracks and the effective area resisting the application of stress respectively. The resisting area is given by $\tilde{A} = A - A_D$, where A_D is the cross sectional area of microvoids and microcracks existing on the same cross section of a material body. The damage variable D given by equation (4.2) is referred to as the isotropic scalar damage variable that characterizes the level of damage in terms of cracks and voids being equally distributed in all directions.

In this work, the scalar damage variable given by equation (4.2) was modified to taken into account the discrete nature of contact separation and the effective area of contact for

particles in DEM simulations of pressed powder materials. If it is assumed that a unit of damage per particle contact is given by

$$d_i = \frac{A_i - \tilde{A}_i}{A_i} \tag{4.3}$$

where d_i is the unit of damage, A_i the contact in the undamaged state, and $\tilde{A}_i$ the contact area in the damaged state, then the average damage can be defined by

$$\bar{d} = \frac{1}{N_I} \sum_{i=1}^{N_I} \frac{A_i - \tilde{A}_i}{A_i} \tag{4.4}$$

The variable N_I in equation (4.4) refers to the total number of contacts in the undamaged state. Note that the use of equation (4.3) as a means to characterize the level of damage in compacts requires a definition of the undamaged state. In this work, the undamaged state was assumed to be the end point of compaction where contacting areas are largest. This assumption specifies that different relative density compactions, as well as particle properties defined differently from simulation to simulation means that the initial undamaged state will have a different starting point for these compacts. As such, damage cannot be considered a material property, rather it is characterizing parameter for the given compact of interest. If it is assumed that the evolution of contact area between spherical particles during unloading is $A \propto \delta_n$ (see Chapter 1, section 1.2), equation (4.3) can be given by

$$\bar{d} = \begin{cases} \dfrac{1}{N_I} \displaystyle\sum_{i=1}^{N_I} \dfrac{\delta_i - \tilde{\delta}_i}{\delta_i} & \tilde{\delta}_i < \delta_b \\ 0 & \tilde{\delta}_i \geq \delta_b \end{cases} \tag{4.5}$$

where δ_i is the initial normal contact deformation in the undamaged state, and $\tilde{\delta}_i$ the current normal contact deformation in the damaged state. From equation (4.5), it is realized that a level of damage $D_2 = 0$ corresponds to the undamaged state, whereas $D_2 = 1$ corresponds to complete separation of initially contacting particles. The difference between this damage variable and the damage variable given by equation (4.1) is the ability of D_2 to characterize the level of damage based on the level of deformation from the undamaged state to the damaged state.

In this work, the total damage the compacted granular assembly experienced was defined in terms of the total sum of contacting surfaces in the damaged and undamaged state by

$$D_2 = 1 - \frac{\sum_{\text{State 2}} \tilde{\delta}_i}{\sum_{\text{State 1}} \delta_i} \tag{4.6}$$

where *state 1* and *state2* refers to the undamaged and damaged state respectively. The damage variable, referred to as D_2 in this work, is defined in a similar manner to the continuum damage mechanics definition of damage given by equation (4.2).

While the characterizing parameters given by $D_1, \bar{d}$, and D_2 can provide details regarding the state of damage, they offer no insight into the orientation of this damage. To determine the orientation of damage, a fabric tensor approach is utilized in this work. One of the many advantages of the DEM is the ability to obtain information pertaining to the location and

orientation of each individual contact that exists throughout the simulation. Fabric tensors can be used to determine contact orientations and the magnitude of the anisotropy that exists in particulate media [88]. A second order fabric tensor $\boldsymbol{F}$ that defines the orientation and anisotropy for the distribution of contacts is given by

$$\boldsymbol{F} = \frac{1}{N_c} \sum_{i=1}^{N_L} n_j n_k \tag{4.7}$$

where N_c and $n_{j,k}$ are the number of contacts the unit normal vector in the direction of the center-to-center distance between the particles. For an axisymmetric system, off-diagonal terms of the tensor are practically zero. Therefore, only the diagonal terms, F_{xx}, F_{yy}, and F_{zz} will exist. The terms F_{xx} and F_{yy} represent the fabric in the radial direction ($F_{xx} \approx F_{yy} = F_{rr}$) and the term F_{zz} represents the fabric in the axial direction. Therefore, a larger value in any of one of these terms means that a larger density of contacts will exist with an orientation corresponding to that term. As an example, a larger value F_{zz} compared to F_{rr} would imply that a larger number contacts exist in the axial direction than in the radial direction. Likewise, if value of F_{zz} decreases overtime while F_{rr} increases, then this implies that either contacts have separated in the axial direction, or more contacts were created in the radial direction.

The damage variables and orientation of damage using a fabric tensor approach discussed above were used to assess the generation of damage for a number of different compaction conditions. In this work, the analysis of damage and the effect this damage has on strength was relegated to unloading, ejection, and tensile test DEM results for particle assemblies compacted in rigid dies. The proposed adhesive, elastoplastic normal contact model was used to describe the force-displacement behavior of contacts. The details of this model, along with details related

to the DEM implementation for this study, are discussed in Chapter 3. The cohesive parameter and maximum asymptotic stiffness are varied in this study to evaluate their effect on strength and damage. For the remaining input parameters to the proposed contact model introduced in Chapter 3, the values listed in Table 4.1 were used. The isolated particle contact stiffness k_1 was defined in terms of yield strength by the similarity solution $k_1 = 3\pi c^2 \sigma_y R$. Assemblies consisting of both 3000 and 5000 particles were examined.

Table 4.1 Model input parmeters

Input Parameters	k_1 [kN/m]	q	n	C	F
Value	35.06	0.323	0.21	0.895	0.18

4.3 Results and Discussion

4.3.1 Effect of Particle Contact Unloading on Tensile Strength and Corresponding Damage

In Chapter 2 and Chapter 3, it was suggested that a connection between residual wall stress and interparticle cohesion existed. It was shown that a decrease in interparticle cohesion resulted in a decrease of residual wall stress. The effect of the elastic properties on tensile strength was analyzed to complete the hypothesis that the strength of compacts is ultimately dictated by not only the interparticle cohesion and the maximum wall stress at the end point of compaction, but also the amount of stored energy, where the stored energy in compressed powders is controlled by the elastic properties. The elastic properties of particles in DEM studies performed in this work were defined by the maximum asymptotic stiffness $\hat{k}_2$. Figure 4.1 shows predicted normalized tensile strength results as a function of both the cohesive parameter and the

normalized asymptotic stiffness for compacts compacted to an in-die relative density equal to 98%. Each of the predicted tensile strength measures shown in Figure 4.1 is a measure from particle assemblies having different properties. Thus, each measure can be considered to have arisen from different materials. Also important to note is that each of predicted tensile strength measures was for materials whose maximum compaction pressure at the end of loading differed due to the high coupling of the loading and unloading force-displacement behavior at contacts. For higher stiffness measures, the maximum compaction pressure was higher. Therefore, for the strength measures shown in Figure 4.1, low stiffness measures arose from materials that were more compliant (i.e., softer materials); whereas high stiffness measures arose from materials that were less compliant (i.e., brittle materials).

For the more brittle materials shown in Figure 4.1, it can be seen that the tensile strength tends to decrease for lower levels of cohesion at the contacts and increases only when the interparticle cohesion becomes significant. This result indicates that not only does the interparticle cohesion affect the tensile strength of compacted materials, but also the elastic properties.

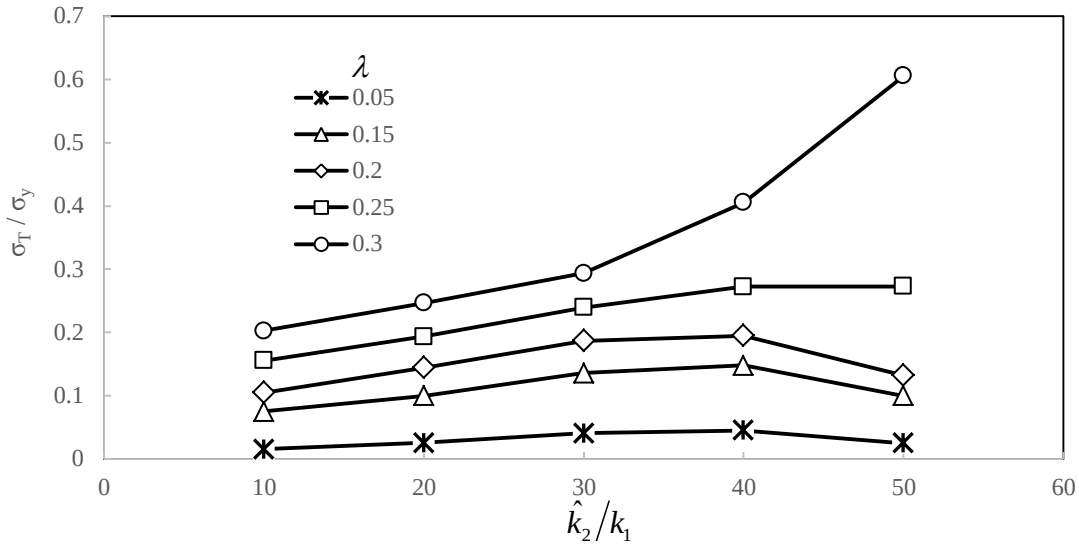

Figure 4.1 DEM prediction of normalized tensile strength as a function of both the cohesive parameter λ and the ratio of the maximum asymptotic stiffness to the isolated particle contact stiffness $\hat{k}_2 / k_1$.

To explain the differences between tensile strength observed in Figure 4.1, an analysis of damage was conducted using the damage variables discussed in section 4.2. Figure 4.2 shows the evolution of damage and fabric for the compactions corresponding to cohesion at contacts equal to λ = 0.15 from Figure 4.1. In Figure 4.2(a-c), evolution of damage was assessed from the end point of compaction to full unloading. Figure 4.2(d) shows the evolution of the ratio of fabric components F_{zz} to F_{rr} from the end point of compaction to full unloading, and Figure 4.2(e) shows the evolution of damage during ejection for the different compaction cases.

It can be seen that damage defined in terms of the number of separated surfaces (cracks) to the total number of contacts results in similar damage for each of the compacted assemblies (Figure 4.1(a)) with the $\hat{k}_2 / k_1 = 50$ compaction case experiencing the greatest number of contact

surface separations and $\hat{k}_2/k_1 = 40$ experiencing the least. An important observation made in Figure 4.2(a) is the rate of damage D_1 with respect to the different stiffness. As can be seen, the rate of contact separation increases with increasing stiffness of the material. It has been found that the rate of defect generation is directly proportional to the density of defects [165].

The results shown in Figure 4.2(a) indicates that there is an interplay between contact unloading stiffness, level of cohesion between contacts, and the density of defects that exists. The density of defects alone does not ultimately determine the strength of compacted materials. Figure 4.2(b) shows the evolution of damage described by the damage variable D_2, which is used to describe the level of damage with respect to the level of deformation (i.e., crack opening). Similar to the observation of the increased rate of damage for the higher stiffness materials in terms of D_1, an increased rate of damage is also observed for damage described in terms of D_2. The increased rate of damage with increasing stiffness is an indication of an increase in the rate of released stored energy. With increasing asymptotic stiffness, unloading of the particle assemblies gives rise to higher initial unloading slopes in the beginning stage of unloading. These initially higher unloading slopes correspond to a greater degree of stored elastic strain energy in the compact. As discussed in Chapters 2 and 3, if this stored energy is enough to overcome the cohesion between particle contacts, the result is the formation of microcracks. From Figure 4.1 and Figure 4.2(b), it is seen that there is point at which the cohesion between particle contacts is overcome by the degree of stored energy released as defined by the unloading stiffness k_2.

Figure 4.2(c), shows the average damage based on the unit of damage per contact d between the $\hat{k}_2/k_1 = 50$ and the $\hat{k}_2/k_1 = 40$ compaction cases. From Figure 4.2(c), it is seen that the average damage follows the same evolution behavior of total damage D_2. The average damage

of the $\hat{k}_2/k_1 = 40$ compaction case differs by approximately 40% compared to the total damage D_2; whereas, the $\hat{k}_2/k_1 = 50$ compaction case differs by approximately 50%. The larger difference between the total and average damage in the $\hat{k}_2/k_1 = 50$ compaction case is an indication of a wider distribution of damage per particle than in the $\hat{k}_2/k_1 = 40$ compaction case. Figure 4.3 shows the distribution of damage per contact for the two compaction cases. From this figure, it can be seen that indeed the distribution of damage is wider for the higher stiffness material compared to the lower stiffness material. It is seen that there is a shift in both an increased percentage of contacts that experienced damage and an increase in the percentage of contacts that have fully separated (d = 1).

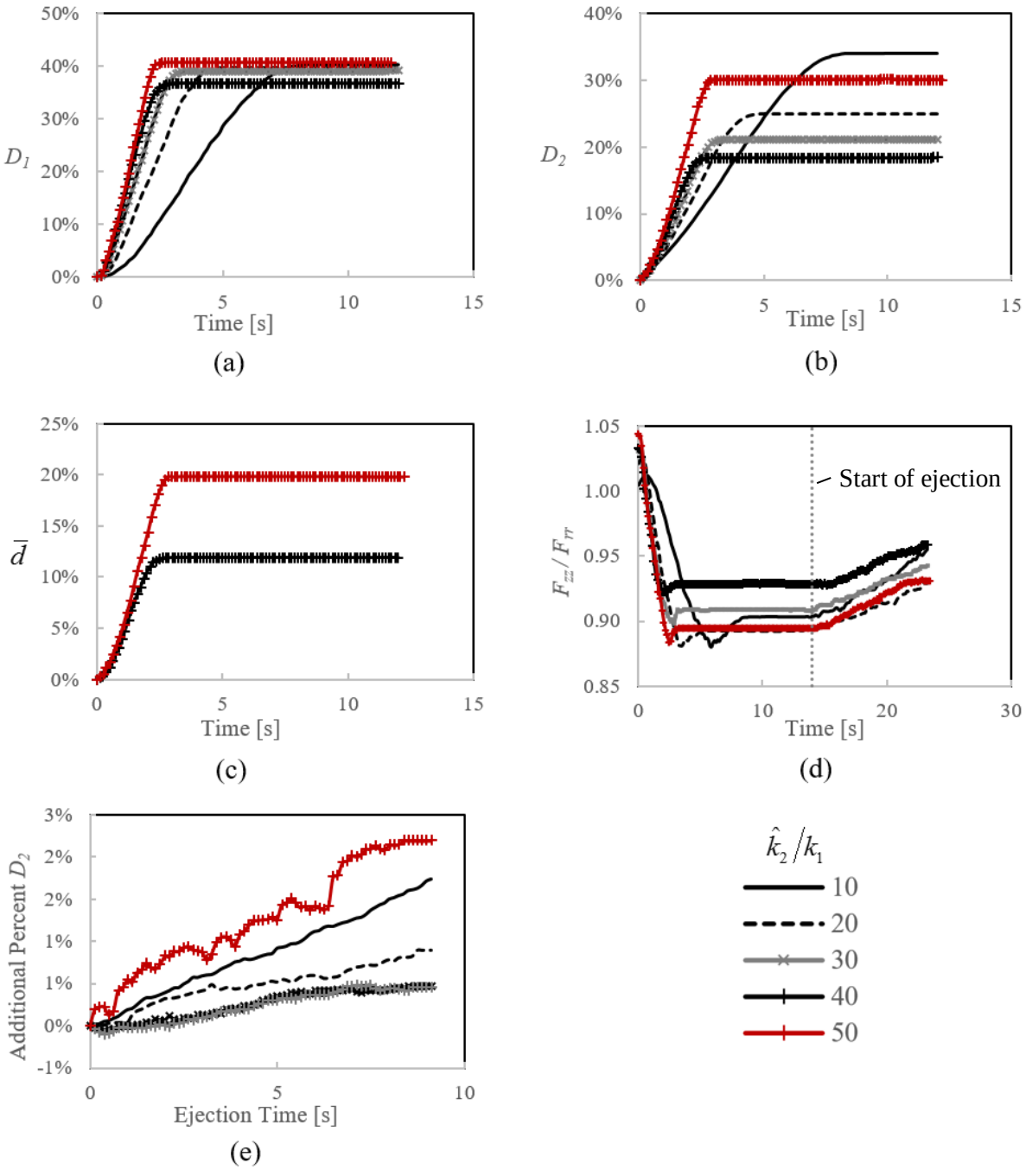

Figure 4.2 Evolution of (a) D_1, (b) D_2, (c) $\bar{d}$, (d) ratio of fabric components F_{zz} to F_{rr}, and (e) additional percentage of damage D_2 during ejection.

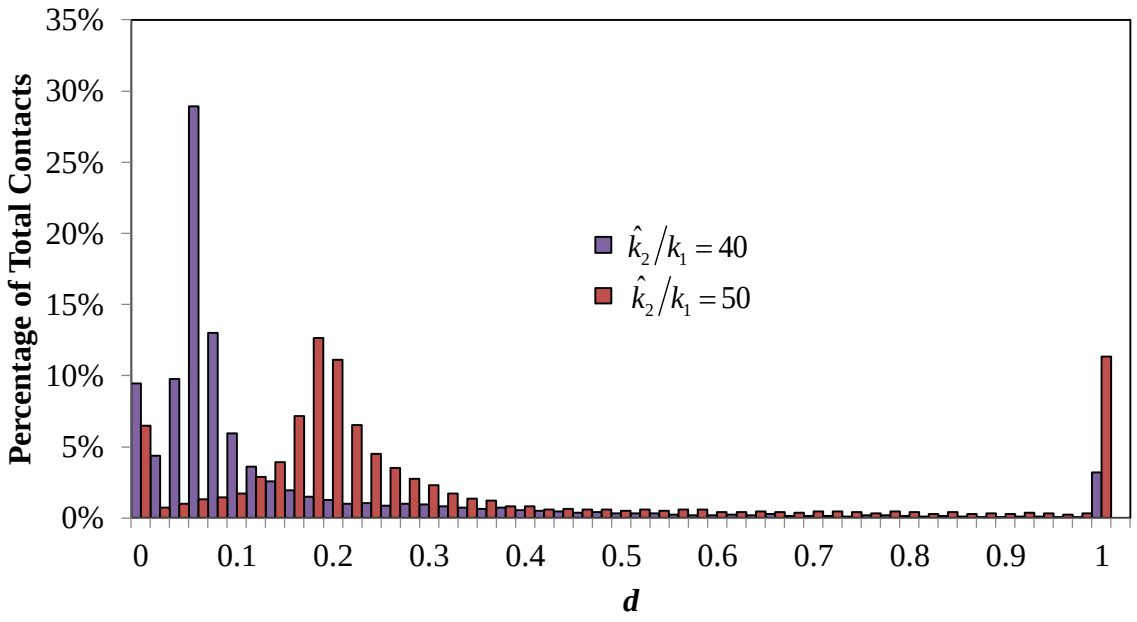

Figure 4.3 Distribution of damage per particle between $\hat{k}_2/k_1 = 40$ and $\hat{k}_2/k_1 = 50$ compaction cases

Figure 4.2(d) shows the ratio of the fabric tensor components F_{zz} and F_{rr}. Observation of Figure 4.2(d) shows that at time t = 0, which corresponds to the end of loading for the particles assemblies, the ratio $F_{zz} / F_{rr} > 1$. This implies that at the end of loading there are a greater number of contacts that exist in the prior compaction direction. As unloading ensues, this ratio begins to decrease below a value of one, which indicates that more contacts exist in the radial direction. From Chapter 2, it was experimentally observed that microcracks extended in the direction perpendicular to the prior compaction direction. An experimental observation of surface microcracking for microcrystalline powder compacted in a straight die can be seen in Figure 4.4. The result of the ratio of fabric tensor components suggests that the reason for a decrease of this value below one is due to the separation of contacts that were oriented

perpendicular to the prior compaction direction. The simulation results given by Figure 4.2(d) confirms this the experimental observation shown in Figure 4.4. Figure 4.2(d) also reveals an increase in the F_{zz} / F_{rr} ratio during unloading of compacts from the die. This suggests that as compacts emerge from the die, further damage occurs and can be attributed to the loss of contacts in the radial direction. During ejection, this ratio never exceeds on, which implies only a small degree of contact loss in the radial direction. Nevertheless, the increase in the F_{zz} / F_{rr} ratio suggests further damage takes place during ejection—an idea thoroughly discussed in Chapter 2. This increase in damage is confirmed by observation of Figure 4.2(e), which shows the evolution of the total damage D_2 as the compacts emerge from the die. Again, the $\hat{k}_2 / k_1 = 50$ compaction case shows the most damage during ejection, as well as the greatest rate of damage. The greater rate and larger damage experienced by this compact can be attributed to the larger degree of elastic stored energy being released as the emerging compact becomes free of radial stresses for the given cohesion of $\lambda = 0.15$ at the contacts. Thus, another aspect to consider—and discussed in detail in Chapter 2—is the effect of the die exit on the degree of damage experienced by compacts.

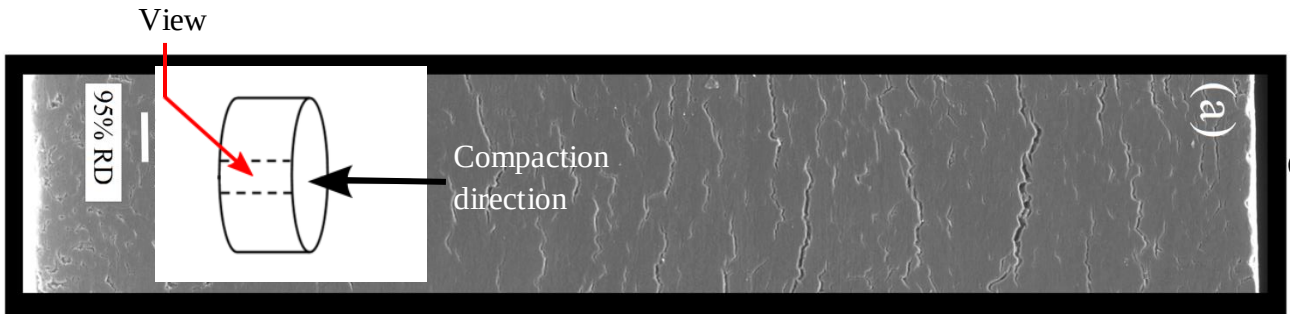

Figure 4.4 Experimental observation of surface microcracking extending in the direction perpendicular to the prior compaction direction for MCC powder compacted in a straight die. This figure appears in Chapter 2, but is displayed here for easy reference.

4.3.2 Prediction of Tensile Stress using Damage Mechanics

Figure 4.5 shows predicted normalized tensile stress as a function of strain for compacts during tensile strength measurements performed using the DEM. The results shown in this figure were generated using the proposed adhesive, elastoplastic contact model introduced in Chapter 3. For each of the results shown in Figure 4.5, the input parameters defining the normal contact model are given in Table 4.1. The asymptotic stiffness was given by $\hat{k}_2 = 30k_1$ for each of the tensile test simulations. It is seen in Figure 4.5 that as the cohesion between contacts is increased, not only does the tensile strength increase as expected, but also the modulus of elasticity. Thus, even though the asymptotic stiffness that defines the force-displacement behavior for unloading contacts was identical for each of the compacts tested, the resulting elastic modulus was shown to increase with increasing cohesion during tensile testing. This

result suggests that cohesion plays a significant role in the elastic properties of powder compacted materials subjected to tensile stresses.

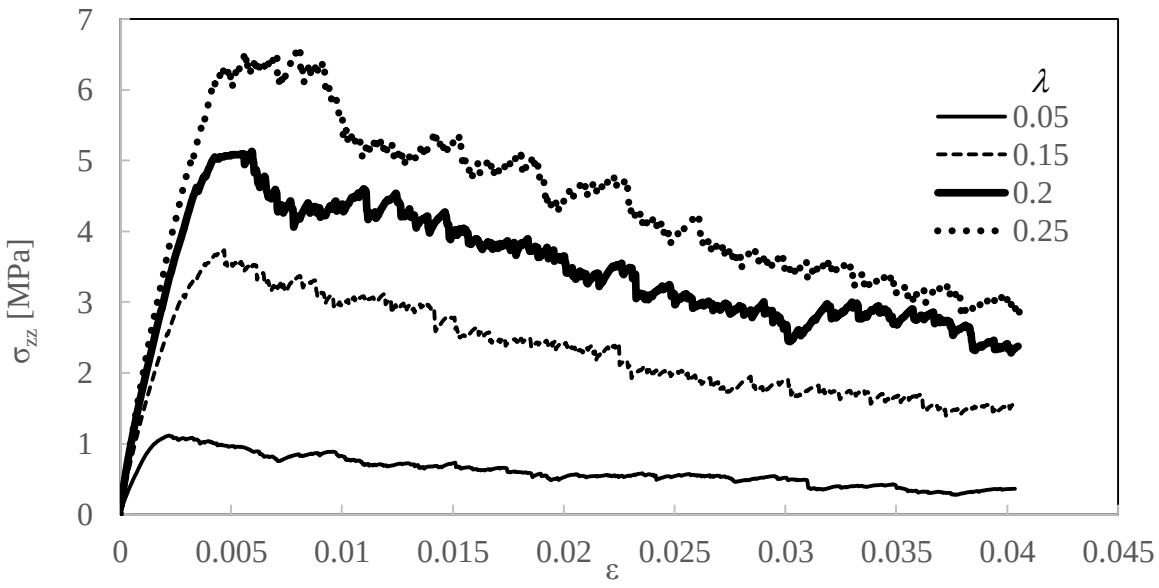

Figure 4.5 Predicted normalized tensile strength as a function of strain for varying levels of the cohesive parameter λ

For each of the compacts tested in Figure 4.5, damage of ejected compacts was assessed using the total damage variable D_2, and an analysis of damage during tensile testing was conducted for the purpose of showing the ability of the damage variable D_2 to predict stress-strain behavior during this test. Prediction of stress-strain behavior was conducted for two cases—specifically, for compacts with cohesion at contacts $\lambda = 0.15$ and 0.2. The predicted stress-strain behavior for the two compacts considered were achieved by using theories from continuum damage mechanics. The specific theory from continuum damage mechanics used to make predictions of the stress-strain behavior of the two compacts was the *Hypothesis of Elastic*

Strain Equivalence (HESE) [166]. In this theory, it is assumed that the elastic strain for a hypothetical material experiencing damage will have an effective strain equal to the measured strain:

$$\bar{\varepsilon} = \varepsilon \tag{4.8}$$

where $\bar{\varepsilon}$ and ε are the effective and measured strain respectively. Using this strain equivalence, the stress versus strain behavior for a material subjected to damage is given by

$$\sigma = E\varepsilon \tag{4.9}$$

$$\bar{\sigma} = \bar{E}\bar{\varepsilon} \tag{4.10}$$

where σ and $\bar{\sigma}$ are the measured and effective stresses respectively, and E and $\bar{E}$ the measured and effective moduli respectively. By "effective", it is meant that the value of effective measure is the measure in an undamaged state; whereas the actual measure is from the damaged state. It is mathematically shown that the effective modulus can be given in terms of the measured modulus and damage variable D_2 by

$$\bar{E} = \frac{E}{(1-D_2)} \tag{4.11}.$$

Using equation (4.11), a prediction of the stress strain behavior is made for the two compacts considered by (1) first obtaining the evolution of damage during tensile testing simulations, then

(2) estimate the effective modulus from tensile test simulation results, and (3) finally make predictions of the stress-strain behavior by $\sigma = \bar{E}(1-D_2)\varepsilon$.

Figure 4.6 shows the total damage for each of the compacts tested in the uniaxial tensile test simulations shown in Figure 4.5. The damage D_2 is shown to increase for decreasing levels of cohesion at the contacts. From Figure 4.6, it can be seen that there is a nonlinear decrease in damage with increasing cohesion, which suggests that the effect of lower cohesion becomes increasing more influential on the response in tension of compressed powder materials. The total damage experienced by the compacts in unloading represent the initial damage for compacts in subjected to tensile stress conditions.

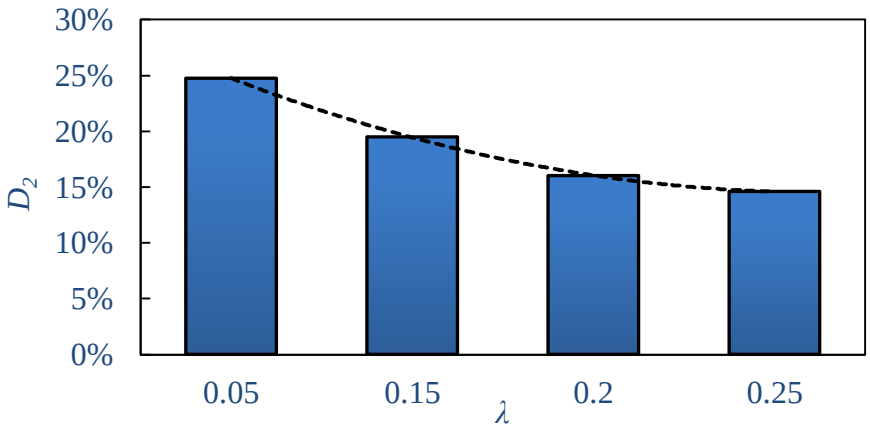

Figure 4.6 Total damage D_2 at end of unloading versus λ

For predictions of the stress-strain behavior of the compacts with cohesion at the contacts defined by λ = 0.15 and 0.2, it was realized that the method used to assess damage during the unloading stage of the compaction process could not be performed in the same way. The reason for this discrepancy was due to the fact that during tensile testing of materials, strain localization may be possible or likely. Strain localization is the phenomena that occurs for materials close to

failure [167]. It was observed that assessing damage on the compact as a whole resulted in very minor additional damage during tensile testing (not shown in this work). Thus it was important to relegate the analysis to the region where both rupturing of the compact occurs and strain localization is expected. It is important to note that the analysis of damage during unloading by considering the entire compact as a whole was justified on the basis of prior experimental observation of the internal structure of compacts in Chapter 2 (see Figure 2.10) where it was observed that damage was essentially equally distributed and ubiquitous throughout the compact. Figure 4.7 shows a schematic of the region of the compact where damage was assessed. This region was made equal to three particle radii in height. It should be noted that although the region height was only three particle diameters, the number of radii in the *z*-direction was actually greater due to the fact that the assembly was significantly compressed.

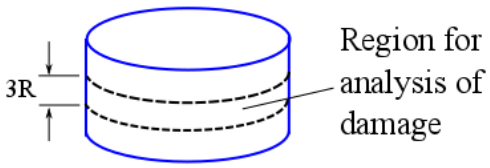

Figure 4.7 Damage analysis region for predicting stress-strain behavior in compacts

Figure 4.8 shows the evolution of damage during tensile testing for the two compacts considered in the prediction of the stress-strain behavior using damage mechanics. As can be seen in this figure, both compacts experience an approximately linear increase in damage initially. This initial increase in damage was related to contacts that could effectively resist the increase in force with deformation. A change in slopes of the evolution of damage is shown to occur at approximate strains of 5×10^{-3} for the $\lambda = 0.15$ case and approximately 6×10^{-3} for the

λ = 0.2 case. Observation of Figure 4.5 reveals that these two strains correspond to the strains where failure of the compacts starts to occur. While it is expected that damage should become worse once failure is met within compacts, the lower slopes indicate that some strain localization, even within the region considered, was still taking place. In other words, once the compacts showed exhibited failure, contacts that were beside the contacts that failed experienced little or no further deformation. Thus, it may be wiser to consider only those contacts and the plane where these contacts exist in the analysis of damage during tensile testing. Nevertheless, predictions are made up to the point where the slope of damage decreases.

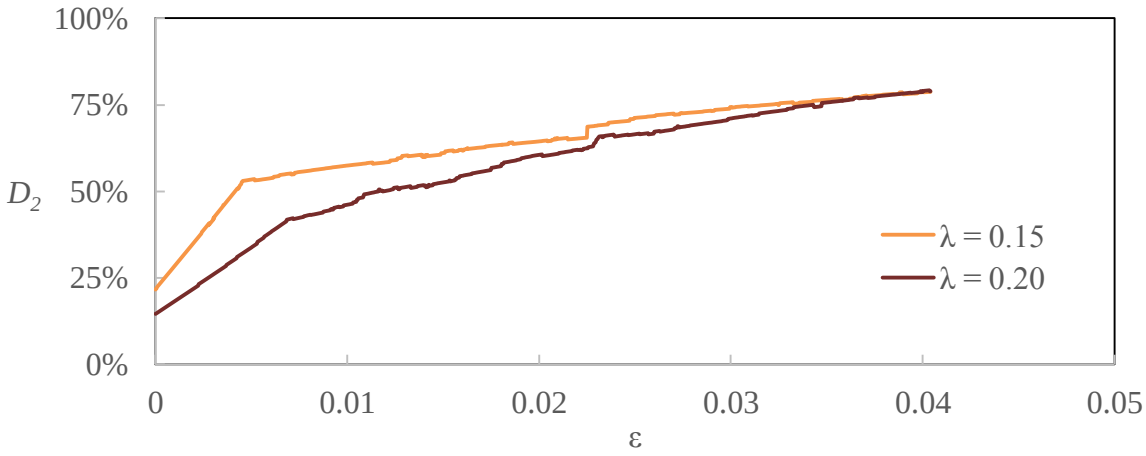

Figure 4.8 Evolution of damage D_2 during tensile testing for compacts with cohesion at the contacts defined by the cohesive parameter λ = 0.15 and 0.2

Figure 4.9 shows predicted stress-strain behavior for the two compacts considered up to strains where tensile strength is determined. From Figure 4.9(a-b), it can be seen that the prediction of the stress-strain behavior using the HESE provides a fairly good prediction of the simulated stress-strain behavior. Figure 4.9(a) shows a both a greater nonlinearity in the

simulated and predicted modulus, which is an indication of greater damage when compared to the predicted and simulated stress-strain behavior shown in Figure 4.9(b). It can be seen that as the failure point is approached, the prediction of the stress-strain behavior begins to deviate from the simulated results. As previously discussed, it was felt that the deviation in the results was due to the effect of strain localization within the region where damage was assessed. Further studies should be conducted to refine the region compact failure occurs.

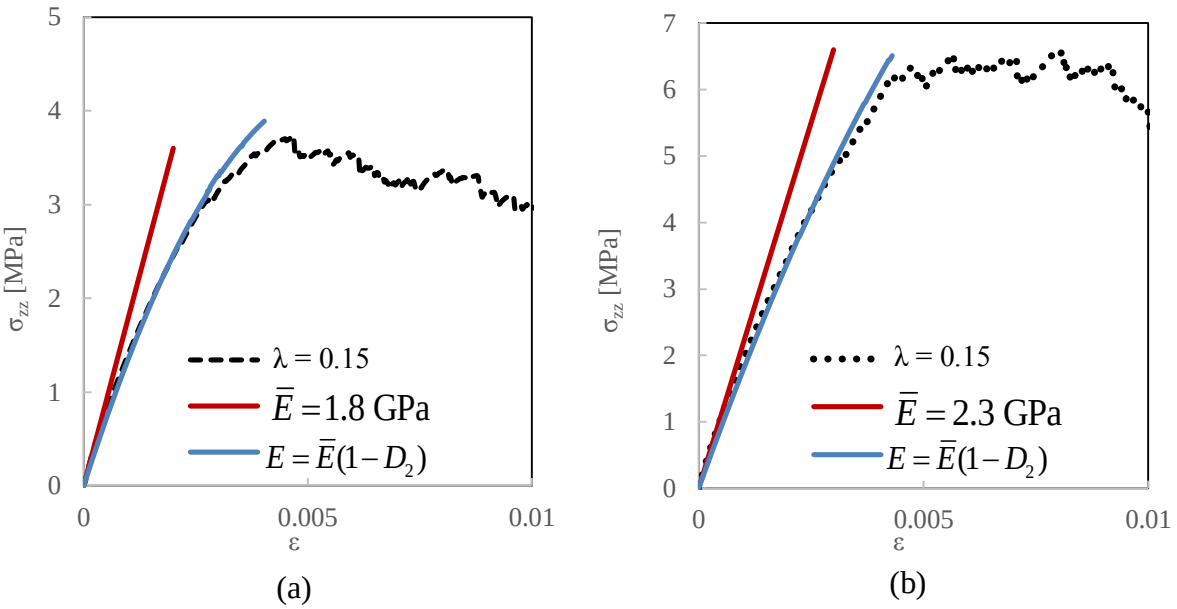

Figure 4.9 Prediction of stress-strain behavior for (a) the compact with cohesion at the contact defined by $\lambda = 0.15$, and (b) the compact with cohesion at the contact defined by $\lambda = 0.2$ using theories from damage mechanics.

4.3.3 Damage as a Function of Relative Density

A common observation made for powders compacted to varying densities is the increase in surface microcracking that occurs with an increase in relative density. The idea of an increase

in observed surface microcracking with an increase in relative density for ejected compacts is, again, related to the amount of elastic stored energy, the interparticle cohesion, maximum wall stress at the end of loading, and the interaction of compacts with the die exit. For powders that have been compacted in the compaction process, the amount of work that is supplied to the powder assembly is either stored as elastic energy or released during unloading and ejection. There are number of mechanisms that permit the release of some of this stored energy, but the primary mechanisms are heat and microcrack formation or propagation. For powders that have been compacted to high density, the expansion from the die size tends to be larger than compacts that have been compacted to lower densities. This expansion from generates high local stresses in the vicinity of the die exit. The result of these high local stresses may produce microcracks or may propagate these microcracks. Therefore, it is claimed that higher density compacts should exhibit a higher degree of surface microcracking. A confirmation of this claim can be seen in Figure 4.10.

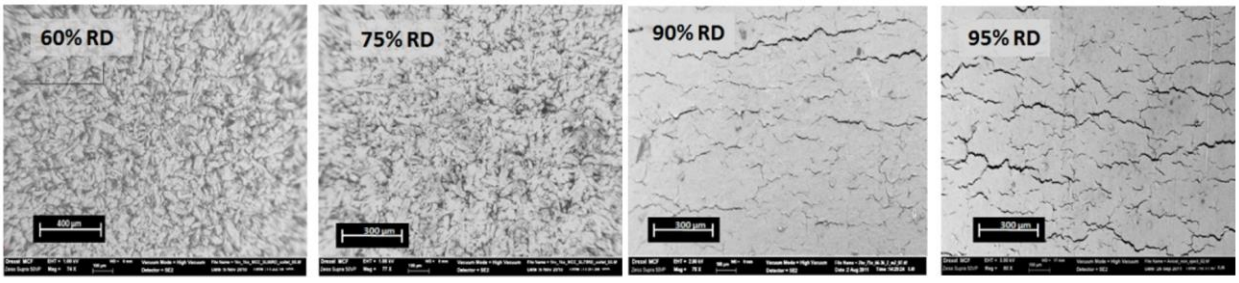

Figure 4.10 Increase in surface microcracking with an increase in RD for microcrystalline cellulose compacts

To assess the DEM's ability to predict the observed phenomenon of greater damage with increasing RD, a damage assessment using the damage variable D_2 was used DEM simulations of particle assemblies compacted to 75%, 85%, and 98% in-die RD. Figure 4.11 shows results for the generation of damage at the end of loading and after ejection for the three compaction cases. It can be seen that the prediction of DEM is in-line with the experimental observation shown in Figure 4.10 While the experimental results shown in Figure 4.10 show only the difference in damage with respect to the surface, the DEM results shown in Figure 4.11 suggests that this damage first occurs during unloading and is further increased as the compacts exit the die—these results are in-line with the findings of Chapter 2.

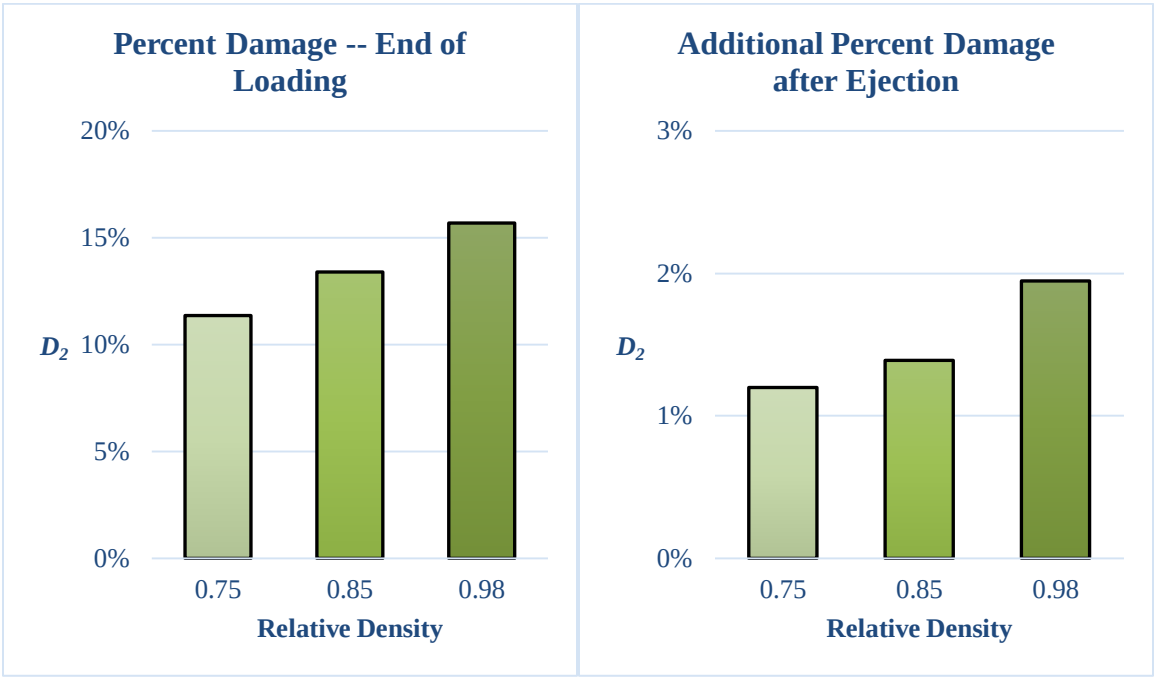

Figure 4.11 Damage D_2 as a function of relative density for both the end of unloading and ejected compacts compacted to in-die relative densities of 75%, 85%, and 98%.

4.3.4 Effect of Boundary Conditions on the Generation of Damage: Straight and Tapered Die Compaction

It was shown in Chapter 2 by a combination of experimental and numerical methods that diffuse microcracking developed in MCC compacts upon removal of the axial load within the die. Some of these diffuse microcracks grew to larger sizes under the action of stresses that develop when the compact was about to exit from a straight die. It was shown that the stresses that develop as the compact exited the die could be significantly reduced by including a taper to the die geometry. The result of this taper was a reduced number and reduced openings of cracks that appeared on the surface of compacts compressed in tapered dies. Thus, the two geometries represented two different boundary conditions that affected generation of damage differently in the two compaction cases.

In this section, DEM compaction simulations of 5000 monosized particle assemblies compacted in both straight and tapered cylindrical dies are considered. The angle of the taper was determined by calculating the radial expansion from the die for the straight die compact. From the radial expansion calculated, a taper angle that allowed full unloading in the radial direction was used in the DEM simulations of compaction of the particle assemblies in tapered die. The particle assemblies were compacted to an in-die relative density of 98%. Evaluation of damage was performed for the particle assemblies compacted in the two dies using the damage variable discussed in section 4.2—specifically D_1 and D_2. The input properties of the proposed adhesive, elastoplastic normal contact model where given by the optimized parameters listed in Table 3.5.

Figure 4.12 shows the evolution of additional percent total damage D_2 for compacts ejected from a straight and tapered die. From this figure it can be seen that both the rate and

level of damage was greater for the straight die compact. For the tapered die, the evolution of damage as the compact exits the start-of-tapered region is more gradual. This more gradual increase in damage and decreased level of damage compared to the straight die compact is consistent with the gradual decreases in stresses predicted from FEM simulations performed in Chapter 2. Furthermore, the reduced level of damage is consistent with the experimental observations of damaged surfaces shown in Figure 2.14.

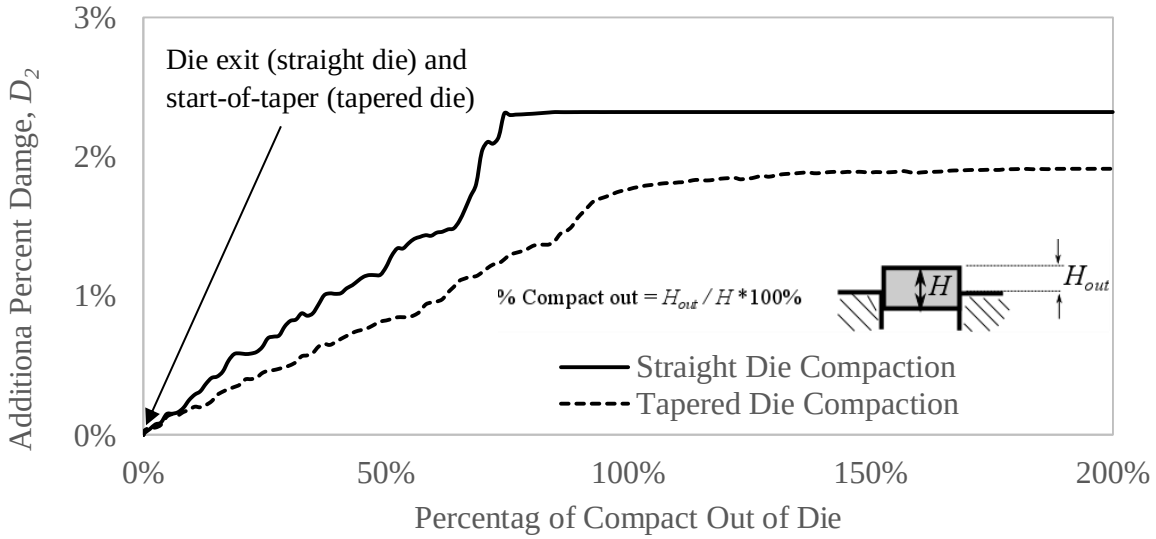

Figure 4.12 Evolution of the additional damage during ejection from straight and tapered dies

In the experimental study presented in Chapter 2, the distribution of crack opening sizes on the surfaces of the straight and tapered die compacts were analyzed (Figure 2.16) and it was found that the overall distribution was nearly identical for the two compacts with the exception of a few larger in crack opening sizes on the straight die compact. It was suggested that the few large crack openings on the surface of the straight die compacts led to the lower observed axial strength relative to the tapered die compact at higher densities. To assess how the die exit and

start-of-taper affected the generation of damage in the two compaction types, evaluation of damage as a function of the distance from the center to outer radii of the two compacts produced in the DEM simulations were conducted. This evaluation of damage was facilitated by dividing each compact into five regions of equal volume. The inset shown in Figure 4.13 depicts the division of the compacts in this analysis of damage. For each region of the compact, damage in terms of the number of contacts that have separated D_1, as well as the total damage D_2 was calculated. Figure 4.13 shows the results for damage using the damage variables D_1 and D_2 for ejected straight and tapered die compacts.

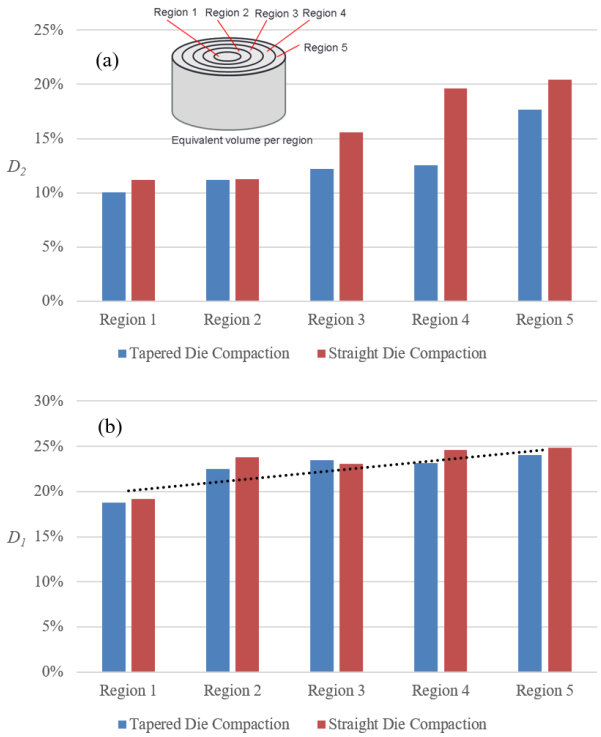

Figure 4.13 Damage evaluation for (a) the total damage D_2 within each region and (b) ratio of the number of separated contacts to the total number of contacts within each region of ejected straight and tapered die compacts.

Figure 4.13(a) shows the comparison of damage D_2 between ejected straight and tapered die compacts. From this figure it can be seen that both compacts show an increase in damage as the outer peripheries of the compacts are approached. However, there is a slightly larger increase in damage experienced by the straight die compact. The region representing the outer peripheries of the two compaction types (Region 5) shows only a small difference in the damage D_2 that was generated. However, nearly the same level of damage in Region 5 appears to continue into Region 4 of the straight die compact, which suggests that the die exit had a larger influence on the through-thickness in the radial direction of the straight die compact.

Figure 4.13(b) shows damage defined by D_1 for each of the regions of the straight and tapered die compacts. The loss of contacts in both compact types did not appear to differ significantly. Close observation of Figure 4.13(b) shows a slight increase in the ratio of lost contacts to the number of contacts per region as the outer peripheries of the compacts are approached. It was found that the damage D_1 for the compacts as whole only differed by approximately 1% with the straight die compact possessing only slightly more separated contacts than the tapered die compact. In Chapter 2, microtomography results of the internal structure of MCC compacts produced in straight and tapered dies were presented (see Figure 2.10 and Figure 2.11). The observation of the experimental results in Figure (2.10 and 2.11) qualitatively showed a similar distribution of microcracking internally between the two compact types. It was shown that differences in the degree of microcracking between the two compact types appeared only on the surfaces. Figure 4.14 shows the distribution of the number of cracks having measured crack opening sizes on the surfaces of MCC compacts produced in straight and tapered dies and compacted to 95% relative density. From this figure, it is seen that the distribution of crack opening sizes is similar for both compaction types with the exception of a few larger cracks that

appear on the surface of the straight die compact. The result shown in Figure 4.13(b) for damage D_1 reflects the similar distribution of microcracking between the straight and tapered die compacts.

The minor differences in microcracking that appears on the surface between the two compact types is negligible in comparison to the total number of cracks throughout both compacts when assessing damage D_1. Instead, Figure 4.15 shows predicted surface crack opening sizes for the straight and tapered die compacts. Results shown in this figure were obtained by considering only the particles representing the outer radial surfaces of the two compact types. A crack was considered to occur if the normal contact deformation δ_n was less than the separation deformation δ_b for any given contact. The crack size opening was calculated by

$$l = \delta_b - \delta \tag{4.12}.$$

The distribution of crack size openings shown in Figure 4.15 produced a similar result to the distribution shown in Figure 4.14. From Figure 4.15, it can be seen that the distribution of crack sizes between the straight and tapered die compacts is nearly identical with the straight die compact containing a few larger in size crack openings than the tapered die compact. The results shown in Figure 4.15 and Figure 4.13(a) present predicted results that agree with the experimental finding in Chapter 2 that the generation of damage is largely influenced by the die exit of the straight die compact, and this damage is reduced if the die is tapered. To assess the effect of the damage between the two compact types, DEM tensile test simulations were

conducted. Figure 4.16(a) shows predicted tensile stress as a function of strain for particle assemblies compacted in straight and tapered dies. It can be seen that the tapered die compact produces a predicted higher strength than the straight die compact in the DEM tensile test simulations. The result in Figure 4.16(a) is consistent with the axial strength experimental findings for MCC compacts produced in straight and tapered dies shown in Figure 4.16(b).

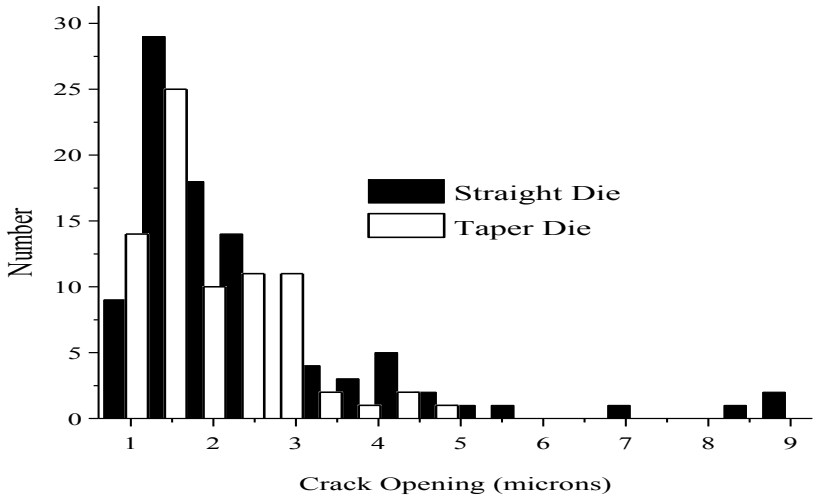

Figure 4.14 Distribution of crack opening lengths on surfaces of MCC compacts compacted to 95% RD in straight and tapered dies. This figure appears in Chapter 2, section 2.4.2 but is shown here for easy reference.

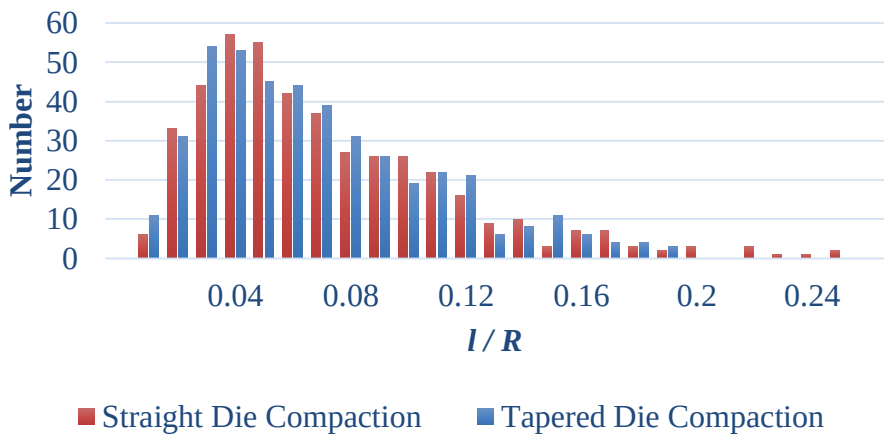

Figure 4.15 Predicted DEM distribution of crack opening lengths on surfaces of 5000 monosized particle assemblies compacted to 98% in-die RD in straight and tapered dies.

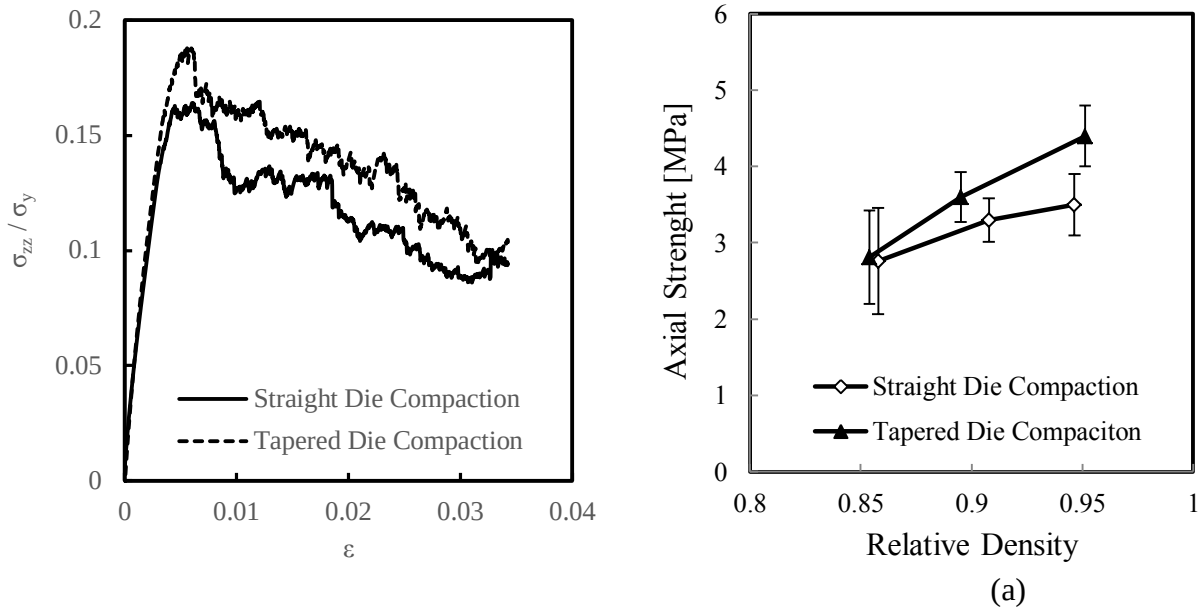

Figure 4.16 Tensile test results for (a) predicted DEM tensile stress as a function of strain for particle assemblies compacted in straight and tapered dies, and (b) tensile strength for MCC compacts as a function of relative density for compacts produced in straight and tapered dies.

4.4 Conclusion

Damage as it pertains to discrete particle systems was considered in this work. Different variables were proposed for assessing damage, which included: damage with respect to the number of contacts that have separated to the total initial number of contacts; total damage based on a modification for discrete particle systems of the traditional isotropic scalar damage variable used in continuum damage mechanics; a unit of damage per particle contact; and orientation of damage using a fabric tensor approach. Using these damage variables, several particle systems were analyzed to assess how damage influenced tensile strength of powder compacted materials for varying factors, such as: the effect of the unloading stiffness on the generation of damage and the effect this damage has strength; damage as a function of relative density; and the effect of boundary conditions.

It was shown that the damage variables proposed in this work provided a satisfactory means of assessing damage and the effect this damage has on strength of powder compacts. The various analysis of damage methods used in this work produced results that are highly agreeable with observation of real powder materials systems—specifically for particles that densify through plastic deformation. It was shown in the damage analysis of particle systems that damage, and ultimately strength of powder materials is dependent on a number of factors. These factors included the level of interparticle cohesion, the elastic properties of the material, and the boundary conditions applied to the system. It was found that a material with high elastic modulus may experience more degradation of strength than a material with lower elastic modulus for a given intperarticle cohesion. It was also found that damage in these higher elastic materials (i.e. brittle materials) were subject to greater damage and rate of damage during unloading and ejection. This type of behavior is consistent with brittle materials.

The analysis of damage showed the proper predictive trend in terms of greater damage with increasing relative density of compacts. Also, the difference between straight and tapered dies in terms of both strength and damage confirmed the experimental evaluation of damage and strength presented in Chapter 2, where it was shown that more damage was present in the straight die compact when compared to the tapered die compact. The damage was assessed using damage variables D_1 and D_2. It was shown damage calculated using D_2 showed an increase in damage as the outer radial surface of the straight and tapered die compacts were approached. There was an increase in damage D_2 for the straight die compact—especially as the outer radial surface is approached compared to the tapered die compacts. When damage was calculated using the damage variable D_1, the straight and tapered die compacts showed nearly the same damage. This result was consistent with experimental findings presented in Chapter 2, where it was shown that the only significant difference in damage D_1 between straight and tapered die compacts was the damage on the surfaces of the two compact types. This difference was predicted using DEM by calculating crack size opening of the particles and their associated contacts that represented the outer radial surface of the compacts.

Chapter 5: Conclusions and Future Work

5.1 Conclusions

The major objectives of this research were concerned with the investigating and analyzing crack formation and the generation of defects in the powder compacted materials. Analysis using both experimental and numerical methods have given substantial insight into the behavior of powders in the die compaction process and a greater understanding of defect formation and damage. Results obtained *via* experimental evaluation have provided exceptional

insight into the mechanical behavior of compacted powders in terms of describing correlations between the multiple parameters and interactions that take place during the process that effect strength and the occurance of internal and surface microcracking of powder compacts. The experimental study presented in Chapter 2 revealed that cracks form in-die and are not created solely by the expansion from die size as the compact exits the die. It was shown that the effect of the interaction of the compact with the edge of the die as it exits should also be localized on the surface—as supported by the FEM results conducted in the straight and tapered die study. On the straight die compacts it was experimentally observed that more intense cracks formed on the surface than on the surface of tapered die compacts.

In terms of computation approaches used to study the behavior of compacted powder, it is believed that the DEM offered a much-improved method for understanding the mechanisms defect formation and the associated strength due to its ability to capture major aspects of the problem by explicitly considering individual particles in the powder material and their interactions at the contact level. For the purpose of acquiring deeper understanding of damage and its effect on strength, one of the goals of this work was to take the first steps towards a contact model that could approximate the behavior of powder particles subjected to compressive and tensile forces in high relative density simulations of die compaction, as well as the ability to easily calibrate the parameters of the proposed contact model from macroscale experiments performed on a real powder system. The formulation of the proposed contact model took a heuristic approach to modeling the pressing of powders to high density. Although the approach was an approximation to the real behavior of contacting particles, results from this work have shown the ability of this model to predict and capture the behavior of powders in the compaction process. The present work dealt with procedures related to the calibration of DEM contact

models where it was shown that fairly good agreement between experiment and DEM simulation results were obtained. One of the key advantages of the calibration procedure is the need for only two experimental techniques: die-compaction, and axial tension tests. The calibration procedure incorporated the central composite design (CCD) of experiments. From the CCD analyses, it was found that the use of the optimized parameters in the proposed contact model resulted in a reasonable approximation of the residual wall stresses for each of the relative density compactions considered. The connection of the residual wall stress to the level of interparticle cohesion was explored. It was found that residual wall stress is connected to tensile strength and may possibly represent a good predictor of strength in compacts.

Finally, analysis of damage for various particle systems was conducted using damage variables introduced in Chapter 4. It was shown that the damage variables provided a satisfactory means of assessing damage and the effect this damage has on strength of powder compacts. The damage analysis gave insight into the factors that effected the strength of compacted materials (i.e., level of interparticle cohesion, the elastic properties of the material, and the boundary conditions applied to the system). It was found that a material with high elastic modulus may experience more degradation of strength than a material with lower elastic modulus for a given intperarticle cohesion. It was also found that damage in these higher elastic materials (i.e. brittle materials) were subject to greater damage and rate of damage during unloading. Furthermore, the damage analysis using the proposed damage variables was able to predict the behavior of damage that have been experimentally observed—specifically, the increase in damage with increasing density and the observed differences in damage as a result of compaction in straight and tapered dies. Finally, it was shown that it was possible to predict the

stress-strain behavior by using the modified damage variable D_2 by estimating the effective modulus.

The significance of this research is of practical interest because it entails both fundamental research relevant to academic settings and addresses a real-world application relevant to industry. If successful, this research will provide a better understanding of the role of cohesion at the interparticle level and can possibly provide a means to better predict the post-compaction mechanical behavior of compacts. In addition, this research will result in a better understanding of the relevant physics necessary for predictive approaches to become possible, which allows for optimization of compaction procedures without the need for considerable experimentation. The significance of predictive capabilities in the compaction of powders allows for a quality-by-design approach (QbD) for purposes satisfying customer requirements and expectations by minimizing the potential impact of variations in a product's manufacturing operation. Furthermore, this research will permit proactive and preventative approaches to possible failures in compacts, which will allow for improvement in the quality of compacted powder products with corresponding reductions in cost. This research will also contribute to the already extensive body of knowledge that exists for powder materials and may also offer a scientific backbone to build upon.

5.2 Future Work

While the work in this thesis was able to provide a deeper understanding of strength and damage in pressed powders, it is important to note that this work only considered powder materials that densify primarily through plastic deformation (i.e., ductile materials). There is still a need to understand the mechanisms of microcrack formation for powder materials that densify

primarily through fragmentation (i.e. brittle materials whose particles fragment during loading). Although many of the findings in this work may also apply to these types of materials, there is still a need to either verify the findings in this work, or to show how some of the proposed mechanisms do not apply.

In terms of the proposed DEM model, further work related polydisperse systems should be conducted. All DEM simulations performed in this work only considered monosized spherical assemblies. To further embolden the use of the proposed adhesive, elastoplastic model introduced in this work, it will be necessary to perform compactions on polydisperse systems to assess how the proposed contact model predicts real powder behavior. Further work should also be conducted to assess the ability of the proposed contact model to predict the path dependence in terms of strength of compacts. It was found in the work presented in Chapter 4 more contacts were lost in the prior compaction direction—also confirmed in the experimental work presented in Chapter 2. It was shown by Galen et al. [20] that path dependence in terms of strength for powder materials that deform by plastic deformation existed. In their work, the strength of these types of powder compacts was observed to be greater in the direction perpendicular to the prior compaction direction and weaker in the direction parallel to the prior compaction direction. Further DEM simulations using the proposed contact model should be conducted to assess whether or not this model can predict the behavior observed by Galen et al.

References

1. James, B.W., *High performance ferrous PM materials for automotive applications.* Metal Powder Report, 1991. **46**(9): p. 26-32.
2. Cooper, A.R. and L.E. Eaton, *Compaction Behavior of Several Ceramic Powders.* Journal of the American Ceramic Society, 1962. **45**(3): p. 97-101.
3. Shima, S. and K. Mimura, *Densification behaviour of ceramic powder.* International Journal of Mechanical Sciences, 1986. **28**(1): p. 53-59.
4. Ollet, A.-L., et al., *A comparative study of the effects of water content on the compaction behaviour of some food materials.* Powder technology, 1993. **75**(1): p. 59-65.
5. Kadiri, M.S., a. Michrafy, and J.a. Dodds, *Pharmaceutical powders compaction: Experimental and numerical analysis of the density distribution.* Powder Technology, 2005. **157**(1-3): p. 176-182.
6. Hiestand, E.N., *Principles, tenets and notions of tablet bonding and measurements of strength.* European Journal of Pharmaceutics and Biopharmaceutics, 1997. **44**: p. 229-242.
7. Klinzing, G. and A. Zavaliangos, *Understanding the Effect of Environmental History on Bilayer Tablet Interfacial Shear Strength.* Pharmaceutical research, 2013. **30**(5): p. 1300-1310.
8. Karehill, P.G., M. Glazer, and C. Nyström, *Studies on direct compression of tablets. XXIII. The importance of surface roughness for the compactability of some directly compressible materials with different bonding and volume reduction properties.* International Journal of Pharmaceutics, 1990. **64**(1): p. 35-43.
9. Wu, C., et al., *Numerical and experimental investigation of capping mechanisms during pharmaceutical tablet compaction.* Powder Technology, 2008. **181**: p. 121-129.
10. Wu, C., et al., *Modelling the mechanical behaviour of pharmaceutical powders during compaction.* Powder Technology, 2005. **152**(1-3): p. 107-117.
11. Anuar, M.S. and B.J. Briscoe, *Detrimental consequences of the paracetamol tablet elastic relaxation during ejection.* Drug Development and Industrial Pharmacy, 2010. **36**(8): p. 972-9.
12. Wu, C.Y., A. Bentham, and A. Mills. *Analysis of failure mechanisms during powder compaction*. in *Materials science forum*. 2007. Trans Tech Publ.
13. Train, D., *An Investigation Into the Compaction of Powders.* Journal of Pharmacy and Pharmacology, 1956. **8**: p. 745-761.
14. Long, W.M., *Radial Pressures in Powder Compaction.* Powder Metallurgy, 1960: p. 73-86.
15. Zhou, J. and Y. Chi. *Shear-band of sand simulated by Particle Flow Code (PFC)*. in *Numerical modeling in micromechanics via particle methods: proceedings of the 1st International PFC Symposium, Gelsenkirchen, Germany*. 2002.
16. Mullarney, M.P. and B.C. Hancock, *Mechanical property anisotropy of pharmaceutical excipient compacts.* International Journal of Pharmaceutics, 2006. **314**(December 2005): p. 9-14.
17. Koerner, R.M. *Combined stress-state (triaxial) compaction for improved green properties*. in *Powder Metallurgy Conference Proceeding*. 1971. New York: MPIF.
18. Vaid, Y.P., et al., *Laboratory characterization of stress-strain behavior of soils by stress and/or strain path loading.* Geotechnical Testing Journal, 2001. **24**(2): p. 200-208.

19. Cheng, Y.P., M.D. Bolton, and Y. Nakat, *Crushing and plastic deformation of soils simulated using DEM.* Geotechnique, 2004. **54**(2): p. 131-141.
20. Galen, S. and A. Zavaliangos, *Strength anisotropy in cold compacted ductile and brittle powders.* Acta Materialia, 2005. **53**: p. 4801-4815.
21. Long, W. and J. Alderton, *THE DISPLACEMENT OF GAS FROM POWDERS DURING COMPACTION*.* Powder Metallurgy, 1960. **3**(6): p. 52-72.
22. Mann, S.C., *Investigation of the Effect of Individual Segments of the Tabletting Cycle on the Capping and Lamination of Pharmaceutical Tablets.* Acta Pharmaceutica Suecica, 1987. **24**(2): p. 54-55.
23. Ritter, A. and H.B. Sucker, *Studies of variables that affect tablet capping.* Pharm. Tech. Int, 1980: p. 56-65.
24. Resende, L. and J.B. Martin, *Formulation of Drucker-Prager Cap Model.* Journal of Engineering Mechanics, 1985. **111**(7): p. 855-881.
25. Michrafy, A., D. Ringenbacher, and P. Tchoreloff, *Modelling the compaction behaviour of powders: application to pharmaceutical powders.* Powder Technology, 2002. **127**(3): p. 257-266.
26. Sinka, I.C., J.C. Cunningham, and A. Zavaliangos, *The effect of wall friction in the compaction of pharmaceutical tablets with curved faces: a validation study of the Drucker-Prager Cap model.* Powder Technology, 2003. **133**(1-3): p. 33-43.
27. Cunningham, J.C., I.C. Sinka, and A. Zavaliangos, *Analysis of tablet compaction. I. Characterization of mechanical behavior of powder and powder/tooling friction.* Journal of Pharmaceutical Sciences, 2004. **93**(8): p. 2022-2039.
28. Han, L.H., et al., *A modified Drucker-Prager Cap model for die compaction simulation of pharmaceutical powders.* International Journal of Solids and Structures, 2008. **45**(10): p. 3088-3106.
29. Garner, S., J. Strong, and A. Zavaliangos, *The extrapolation of the Drucker–Prager/Cap material parameters to low and high relative densities.* Powder Technology, 2015. **283**: p. 210-226.
30. Sinka, I.C., J.C. Cunningham, and A. Zavaliangos, *Analysis of Tablet Compaction . II . Finite Element Analysis of Density Distributions in Convex Tablets.* Analysis, 2004. **93**(8): p. 2040-2053.
31. Michrafy, A., J.A. Dodds, and M.S. Kadiri, *Wall friction in the compaction of pharmaceutical powders: measurement and effect on the density distribution.* Powder Technology, 2004. **148**(1): p. 53-55.
32. Dec, R.T., A. Zavaliangos, and J.C. Cunningham, *Comparison of various modeling methods for analysis of powder compaction in roller press.* Powder Technology, 2003. **130**(1-3): p. 265-271.
33. Michrafy, A., et al., *Analysis of strain stress state in roller compaction process.* Powder Technology, 2011. **208**(2): p. 417-422.
34. Muliadi, A.R., J.D. Litster, and C.R. Wassgren, *Modeling the powder roll compaction process: Comparison of 2-D finite element method and the rolling theory for granular solids (Johanson's model).* Powder Technology, 2012. **221**: p. 90-100.
35. Drucker, D.C. and W. Prager, *Soil mechanics and plastic analysis for limit design.* Quarterly of Applied Mathematics, 1952. **10**(2): p. 157-165.
36. DiMaggio, F.L. and I.S. Sandler, *Material Models for Granular Soils.* Journal for Engineering Mechanics, ASCE, 1971. **97**: p. 935-950.

37. Arzt, E., *The Influence of an Increasing Particle Coordination on the Densification of Spherical Powders.* Acta Metallugica, 1982. **30**: p. 1883-1890.
38. Fleck, N.A., *On the Cold Compaction of Powders.* Journal of the Mechanics and Physics of Solids, 1995. **43**(9): p. 1409-1431.
39. Larsson, P.-L.B.S.S.B., *Analysis of Cold and Hot Isostatic Compaction of Spherical Particles.* Acta Metallurgica, 1996. **44**(9): p. 3655-3666.
40. Storakers, B., N.A. Fleck, and R.M. McMeeking, *The viscoplastic compaction of composite powders.* Journal of the Mechanics and Physics of Solids, 1999. **47**: p. 785-815.
41. Wang, W., *Towards an improved understanding of strength and anisotropy of cold compacted powder*. 2007. p. 1-145.
42. Koerner, R.M. and W. McCabe. *Combined stress-state (triaxial) compaction for improved green properties*. in *pp 267-279 of 1971 Fall Powder Metallurgy Conference Proceedings. Mocarski, S.(ed.). New York Metal Powder Industries Federation, 1972.* 1973. Drexel Univ., Philadelphia.
43. Cundall, P.A. and O.D.L. Strack, *A discrete numerical model for granular assemblies*. 1979. p. 47-65.
44. Heyliger, P.R. and R.M. McMeeking, *Cold plastic compaction of powders by a network model.* Journal of the Mechanics and Physics of Solids, 2001. **49**(9): p. 2031-2054.
45. Redanz, P. and N.A. Fleck, *The compaction of a random distribution of metal cylinders by the discrete element method.* Acta Materialia, 2001. **49**: p. 4325-4335.
46. Thornton, C. and S.J. Antony, *Quasi-static deformation of particle media.* Philosophical Transactions of the Royal Scociety, 1998. **356**: p. 2763-2782.
47. Iwashita, K. and M. Oda, *Rolling Resistance at Contact in Simulation of Shear Band Development by DEM.* Journal of Engineering Mechanics, 1998. **124**(3): p. 285-292.
48. Martin, C.L. and D. Bouvard, *Study of the cold compaction of composite powders by the discrete element method.* Acta Materialia, 2003. **51**: p. 373-386.
49. Martin, C.L., D. Bouvard, and S. Shima, *Study of particle rearrangement during powder compaction by the Discrete Element Method.* Journal of the Mechanics and Physics of Solids, 2003. **51**(4): p. 667-693.
50. Martin, C.L. and D. Bouvard, *Isostatic compaction of bimodal powder mixtures and composites.* International Journal of Mechanical Sciences, 2004. **46**(6): p. 907-927.
51. Gethin, D.T., et al., *Numerical comparison of a deformable discrete element model and an equivalent continuum analysis for the compaction of ductile porous material.* Computers & Structures, 2001. **79**(13): p. 1287-1294.
52. Gethin, D.T., R.W. Lewis, and R.S. Ransing, *A discrete deformable element approach for the compaction of powder systems.* Modelling and Simulation in Materials Science and Engineering, 2003. **11**(1): p. 101-114.
53. Procopio, A.T. and A. Zavaliangos, *On the Compaction of Granular Media Using a Multi-Particle Finite Element Model.* Philosophy, 2005. **53**(7): p. 1523-1551.
54. Ransing, R.S.U., et al., *Powder compaction modelling via the discrete and finite element method.* Materials and Design, 2000. **21**: p. 263-269.
55. Harthong, B., et al., *Modeling of high-density compaction of granular materials by the Discrete Element Method.* International Journal of Solids and Structures, 2009. **46**(18-19): p. 3357-3364.

56. Harthong, B. and D. Imbault, *The study of relations between loading history and yield surfaces in powder materials using discrete finite element simulations.* Journal of the Mechanics and Physics, 2011.
57. Duran, J., *Sands, powders, and grains: An introduction to the physics of granular materials*. 2000, New York: Springer.
58. Zhu, H.P., et al., *Discrete particle simulation of particulate systems: Theoretical developments.* Chemical Engineering Science, 2007. **62**(13): p. 3378-3396.
59. Sneddon, I.N., *The relation between load and penetration in the axisymmetric Boussinesq problem for a punch of arbitrary profile.* International journal of engineering science, 1965. **3**(1): p. 47-57.
60. Storåkers, B., S. Biwa, and P.-L. Larsson, *Similarity Analysis of Inelastic Contact.* International Journal of Solids and Structures, 1997. **34**(24): p. 3061-3083.
61. Spence, D. *Self similar solutions to adhesive contact problems with incremental loading*. in *Proceedings of the Royal Society of London A: Mathematical, Physical and Engineering Sciences*. 1968. The Royal Society.
62. Tsigginos, C., J. Strong, and A. Zavaliangos, *On the force–displacement law of contacts between spheres pressed to high relative densities.* International Journal of Solids and Structures, 2015. **60-61**: p. 17-27.
63. Frenning, G., *Towards a mechanistic model for the interaction between plastically deforming particles under confined conditions: A numerical and analytical analysis.* Materials Letters, 2013. **92**: p. 365-368.
64. Frenning, G., *Towards a mechanistic contact model for elastoplastic particles at high relative densities.* Finite Elements in Analysis and Design, 2015. **104**: p. 56-60.
65. Derjaguin, B.V., V.M. Muller, and Y.P. Toporov, *Effect of contact deformations on the adhesion of particles.* Journal of Colloid and interface science, 1975. **53**(2): p. 314-326.
66. Johnson, K., K. Kendall, and A. Roberts. *Surface energy and the contact of elastic solids*. in *Proceedings of the Royal Society of London A: Mathematical, Physical and Engineering Sciences*. 1971. The Royal Society.
67. Tabor, D., *Surface Forces and Surface Interactions.* Journal of Colloid and Interface Science, 1977. **58**(1): p. 1-13.
68. Maugis, D., *Adhesion of Spheres - the Jkr-Dmt Transition Using a Dugdale Model.* Journal of Colloid and Interface Science, 1992. **150**(1): p. 243-269.
69. Mesarovic, S.D. and K.L. Johnson, *Adhesive contact of elastic-plastic spheres.* Journal of the Mechanics and Physics of Solids, 2000. **48**(10): p. 2009-2033.
70. Iwashita, K. and M. Oda, *Mechanics of granular materials: an introduction*. 1999: CRC Press.
71. Di Renzo, A. and F.P. Di Maio, *Comparison of contact-force models for the simulation of collisions in DEM-based granular flow codes.* Chemical Engineering Science, 2004. **59**(3): p. 525-541.
72. Capece, M., E. Bilgili, and R.N. Dave, *Formulation of a physically motivated specific breakage rate parameter for ball milling via the discrete element method.* Aiche Journal, 2014. **60**(7): p. 2404-2415.
73. Langston, P.A., U. Tüzün, and D.M. Heyes, *Discrete element simulation of granular flow in 2D and 3D hoppers: Dependence of discharge rate and wall stress on particle interactions.* Chemical Engineering Science, 1995. **50**(6): p. 967-987.

74. Cleary, P.W., G. Metcalfe, and K. Liffman, *How well do discrete element granular flow models capture the essentials of mixing processes?* Applied Mathematical Modelling, 1998. **22**(12): p. 995-1008.
75. Thornton, C. and L. Zhang, *Numerical Simulations of the Direct Shear Test.* Chemical Engineering & Technology, 2003. **26**(2): p. 153-156.
76. Tzaferopoulos, M.A., *On a quasi-static discrete element model of granular materials.* Computers and Geotechnics, 1996. **18**(2): p. 145-165.
77. Singh, A., et al., *Effect of cohesion on shear banding in quasi-static granular material.* arXiv, 2013: p. 12-12.
78. Riedel, H., et al., *Numerical simulation of die pressing and sintering—development of constitutive equations.* International Journal of Refractory Metals and Hard Materials, 1994. **12**(2): p. 55-60.
79. Fleck, N.a., L.T. Kuhn, and R.M. McMeeking, *Yielding of metal powder bonded by isolated contacts.* Journal of the Mechanics and Physics of Solids, 1992. **40**(5): p. 1139-1162.
80. Martin, C.L., *Unloading of powder compacts and their resulting tensile strength.* Acta Materialia, 2003. **51**(15): p. 4589-4602.
81. Martin, C.L., D. Bouvard, and G. Delette, *Discrete element simulations of the compaction of aggregated ceramic powders.* Journal of the American Ceramic Society, 2006. **89**(11): p. 3379-3387.
82. Zavaliangos, A., et al., *Temperature evolution during compaction of pharmaceutical powders.* Journal of Pharmaceutical Sciences, 2008. **97**(8): p. 3291-3304.
83. Heckel, R.W., *Density-pressure relationships in pwder compaction.* Trans Metall Soc AIME, 1961. **221**(4): p. 671-675.
84. Gurson, A.L., *Continuum theory of ductile rupture by void nucleation and growth: part I, yield criteria and flow rules for porous ductile media.* ASME J. Engr. Mat. Tech. , 1977. **99**: p. 2-15.
85. Tvergaard, V. and A. Needleman, *Effects of nonlocal damage in porous plastic solids.* International Journal of Solids and Structures, 1995. **32**(8-9): p. 1063-1077.
86. Allix, O. and F. Hild, *Continnum Damage Mechanics of Materials and Structures*. 2002, Oxford: Elsevier.
87. Voyiadjis, G.Z. and P.I. Kattan, *Advances in Damage Mechanics*. 2nd ed. 2006, London: Elsevier. 708-708.
88. O, S., C., *Particulate Discrete Element Modelling: A Geomechanics Perspective*. 2011, London: Spon Press/Taylor & Francis.
89. Zhu, H.P., et al., *Discrete particle simulation of particulate systems: A review of major applications and findings.* Chemical Engineering Science, 2008. **63**(23): p. 5728-5770.
90. Verlet, L., *Computer" experiments" on classical fluids. I. Thermodynamical properties of Lennard-Jones molecules.* Physical review, 1967. **159**(1): p. 98.
91. O'Sullivan, C. and J.D. Bray, *Selecting a suitable time step for discrete element simulations that use the central difference time integration scheme.* Engineering Computations, 2004. **21**(2-4): p. 278-303.
92. Luding, S., K. Manetsberger, and J. Müllers, *A discrete model for long time sintering.* Journal of the Mechanics and Physics of Solids, 2005. **53**(2): p. 455-491.
93. Thornton, C. and C. Randall, *Applications of theoretical contact mechanics to solid particle system simulation.* 1988.

94. Itasca, *PFC 3D user manual*. 2003, Itasca consulting group Inc.: Minneapolis.
95. Kremmer, M. and J.F. Favier, *A method for representing boundaries in discrete element modelling—part II: Kinematics.* International Journal for Numerical Methods in Engineering, 2001. **51**(12): p. 1423-1436.
96. Tardos, G.I., S. McNamara, and I. Talu, *Slow and intermediate flow of a frictional bulk powder in the Couette geometry.* Powder Technology, 2003. **131**: p. 23-39.
97. Cundall, P., *Distinct element models of rock and soil structure.* Analytical and computational methods in engineering rock mechanics, 1987. **4**: p. 129-163.
98. Schubert, H., W. Herrmann, and H. Rumpf, *Deformation behaviour of agglomerates under tensile stress.* Powder Technology, 1975. **11**: p. 121-131.
99. Maugis, D. and H.M. Pollock, *Surface forces, deformation and adherence at metal microcontacts.* Acta metall., 1984. **32**(9): p. 1323-1334.
100. Johnson, K.L., *Contact Mechanics*. 1985, Cambridge: Cambridge University Press.
101. Thornton, C. and Z. Ning, *A theoretical model for the stick/bounce behaviour of adhesive, elastic-plastic spheres.* Powder Technology, 1998. **99**(2): p. 154-162.
102. Tomas, J., *Particle Adhesion Fundamentals and Bulk Powder Consolidation.* Kona, 2000. **18**(18): p. 157-169.
103. Luding, S., *Anisotropy in cohesive, frictional granular media.* Journal of Physics-Condensed Matter, 2005. **17**(24): p. S2623-S2640.
104. Luding, S., *Shear flow modeling of cohesive and frictional fine powder.* Powder Technology, 2005. **158**(1-3): p. 45-50.
105. Luding, S., *Cohesive, frictional powders: contact models for tension.* Granular Matter, 2008. **10**(4): p. 235-246.
106. Walton, O.R. and S.M. Johnson. *Simulating the Effects of Interparticle Cohesion in Micron- Scale Powders*. 2009.
107. Mindlin, R. and H. Deresiewicz, *Elastic spheres in contact under varying oblique forces.* ASME Journal of Applied Mechanics, 1953. **20**: p. 327-344.
108. Thornton, C. and K.K. Yin, *Impact of Elastic Spheres with and without Adhesion.* Powder Technology, 1991. **65**(1-3): p. 153-166.
109. Vu-Quoc, L., L. Lesburg, and X. Zhang, *An accurate tangential force-displacement model for granular-flow simulations: Contacting spheres with plastic deformation, force-driven formulation.* Journal of Computational Physics, 2004. **196**(1): p. 298-326.
110. Olsson, E. and P.-L. Larsson, *On the Effect of Particle Size Distribution in Cold Powder Compaction.* Journal of Applied Mechanics, 2012. **79**(5): p. 051017-051017.
111. Sugimori, K., S. Mori, and Y. Kawashima, *Characterization of die wall pressure to predict capping of flat- or convex-faced drug tablets of various sizes.* Powder Technology, 1989. **58**(4): p. 259-264.
112. McKenna, A. and D.F. McCafferty, *Effect of particle size on the compaction mechanism and tensile strength of tablets.* Journal of Pharmacy and Pharmacology, 1982. **34**(6): p. 347-351.
113. Bozic, D.Z., R. Dreu, and F. Vrecer, *Influence of dry granulation on compactibility and capping tendency of macrolide antibiotic formulation.* International Journal of Pharmaceutics, 2008. **357**(1-2): p. 44-54.
114. Garr, J.S.M. and M.H. Rubinstein, *An Investigation into the Capping of Paracetamol at Increasing Speeds of Compression.* International Journal of Pharmaceutics, 1991. **72**(2): p. 117-122.

115. Ruegger, C.E. and M. Celik, *The effect of compression and decompression speed on the mechanical strength of compacts.* Pharmaceutical Development and Technology, 2000. **5**(4): p. 485-494.
116. Mann, S.C., et al., *The effect of high speed of compression at sub-atmospheric pressures on the capping tendency of pharmaceutical tablets.* Journal of Pharmacy and Pharmacology, 1983. **35**.
117. Hoblitzell, J.R. and C.T. Rhodes, *Determination of a Relationship between Force-Displacement and Force-Time Compression Curves.* Drug Development and Industrial Pharmacy, 1990. **16**(2): p. 201-229.
118. Schmidt, P.C. and U. Tenter, *Displacement Measurements of Rotary Presses.* Pharmazeutische Industrie, 1985. **47**(4): p. 426-430.
119. Ashby, M.F. and C.G. Sammis, *The Damage Mechanics of Brittle Solids in Compression.* Pure and Applied Geophysics, 1990. **133**(3): p. 489-521.
120. Ashby, M.F. and S.D. Hallam, *The Failure of Brittle Solids Containing Small Cracks under Compressive Stress States.* Acta Metallurgica, 1986. **34**(3): p. 497-510.
121. Roberts, R.J. and R.C. Rowe, *Brittle Ductile Behavior in Pharmaceutical Materials Used in Tabletting.* International Journal of Pharmaceutics, 1987. **36**(2-3): p. 205-209.
122. Griffith, A.A., *The Phenomena of Rupture and Flow in Solids.* Philosophical Transactions of the Royal Society of London. Series A, Containing Papers of a Mathematical or Physical Character, 1921. **221**: p. 163-198.
123. Irwin, G.R., *Analysis of Stresses and Strains Near the End of a Crack Traversing a Plate.* J. Appl. Mech., 1957.
124. Robinson, B., A.T. Procopio, and A. Zavaliangos. *Nonlinear elastic behavior and its implications on unloading, ejection and dimensional changes of powder compacts*. in *The MPIF/APMI international conference on powder metallurgy and particulate materials*. 2009. Las Vegas, NV.
125. Gamble, J.F., W.-S. Chiu, and M. Tobyn, *Investigation into the impact of sub-populations of agglomerates on the particle size distribution and flow properties of conventional microcrystalline cellulose grades.* Pharmaceutical Development and Technology, 2011. **16**(5): p. 542-8.
126. Fell, J.T. and J.M. Newton, *Effect of particle size and speed of compaction on density changes in tablets of crystalline and spray-dried lactose.* Journal of Pharmaceutical Sciences, 1971. **60**(12): p. 1866-1869.
127. Roberts, R.J. and R.C. Rowe, *The effect of the relationship between punch velocity and particle size on the compaction behaviour of materials with varying deformation mechanisms.* Journal of Pharmacy and Pharmacology, 1986. **38**(8): p. 567-571.
128. Garr, J.S.M. and M.H. Rubinstein, *The effect of rate of force application on the properties of microcrystalline cellulose and dibasic calcium phosphate mixtures.* International Journal of Pharmaceutics, 1991. **73**: p. 75-80.
129. Mann, S.C., et al., *Influence on Punch Tolerance on Capping.* Journal of Pharmacy and Pharmacology, 1981. **33**(s1): p. 25P-25P.
130. Sinka, I.C., et al., *Measurement of density variations in tablets using X-ray computed tomography.* International Journal of Pharmaceutics, 2004. **271**(1-2): p. 215-224.
131. Phillips, D.H. and J.J. Lannutti, *Measuring physical density with X-ray computed tomography.* Ndt & E International, 1997. **30**(6): p. 339-350.

132. Busignies, V., et al., *Quantitative measurements of localized density variations in cylindrical tablets using X-ray microtomography.* European journal of pharmaceutics and biopharmaceutics : official journal of Arbeitsgemeinschaft für Pharmazeutische Verfahrenstechnik e.V, 2006. **64**(1): p. 38-50.
133. McDonald, S.a., et al., *Shear cracking in an Al powder compact studied by X-ray microtomography.* Materials Science and Engineering: A, 2009. **508**(1-2): p. 64-70.
134. Fell, J.T. and J.M. Newton, *Determination of tablet strength by the diametral-compression test.* Journal of Pharmaceutical Sciences, 1970. **59**(5): p. 688-691.
135. Newton, J.M., et al., *The compressive to tensile strength ratio of pharmaceutical compacts.* International Journal of Pharmaceutics, 1993. **93**(1–3): p. 249-251.
136. Nystrom, C., W. Alex, and K. Malmqvist, *A new approach to tensile strength measurements of tablets.* Acta Pharmaceutica Suecica, 1977. **14**(3): p. 317.
137. Akseli, I., et al., *Mechanistic characterization of bilayer tablet formulations.* Powder Technology, 2013. **236**: p. 30-36.
138. ABAQUS, *ABAQUS Theory Manual V6.8*. 2008, Dassault Simulia.
139. Heyn, E., *The Metallographist*. Vol. 5. 1903, Boston, Mass.: Sauveur and Whiting.
140. Liu, H. and Y. Lin, *Effect of exit shape of compaction mold on coal log quality.* Powder Technology, 1997. **90**(3): p. 267-271.
141. Luding, S., *Introduction to discrete element methods: basic of contact force models and how to perform the micro-macro transition to continuum theory.* European Journal of Environmental and Civil Engineering, 2008. **12.7**(8): p. 785-826.
142. Repka, M.A., N. Langley, and J. DiNunzio, *Melt Extrusion: Materials, Technology and Drug Product Design*, ed. M.A. Repka, N. Langley, and J. DiNunzio. 2013, New York: Springer.
143. Wang, Q.Z., et al., *The flattened Brazilian disc specimen used for testing elastic modulus, tensile strength and fracture toughness of brittle rocks: analytical and numerical results.* International Journal of Rock Mechanics and Mining Sciences, 2004. **41**(2): p. 245-253.
144. Kloss, C., et al., *Models, algorithms and validation for opensource DEM and CFD-DEM.* Progress in Computational Fluid Dynamics, 2012. **12**(2-3): p. 140-152.
145. Scott, G. and D. Kilgour, *The density of random close packing of spheres.* Journal of Physics D: Applied Physics, 1969. **2**(6): p. 863.
146. Oda, M., J. Konishi, and S. Namet-Nasser, *Experimental micromechanical evaluation of the strength of granular materials: Effect of particle rolling, In Mechanis of Granular Materials: New Models and Constitutive Relations*, ed. J.T. Jenkins and M. Satake Amsterdam. 1983: Elsevier.
147. Oda, M. and K. Iwashita, *Study on couple stress and shear band development in granular media based on numerical simulation analyses.* International journal of engineering science, 2000. **38**(15): p. 1713-1740.
148. Afferrante, L., M. Ciavarella, and E. Valenza, *Is Weibull's modulus really a material constant? Example case with interacting collinear cracks.* International Journal of Solids and Structures, 2006. **43**(17): p. 5147-5157.
149. Domike, R.D., *Pharmaceutical Powders in Experiment and Simulation: Towards a Fundemental Understanding*, in *Chemical Engineering*. 2000, Massachusetts Institute of Technology: Georgia Institute of Technology. p. 178.

150. Yoon, J., *Application of experimental design and optimization to PFC model calibration in uniaxial compression simulation.* International Journal of Rock Mechanics and Mining Sciences, 2007. **44**(6): p. 871-889.
151. Favier, J.F., D. Curry, and R. LaRoche, *Calibration of DEM material models to approximate bulk particle characteristics,* in *6th Worl Congress on Particle Technology*. 2010: Nurember, Germany.
152. Johnstone, M.W., *Calibration of DEM models for granular materials using bulk physical tests*. 2010, The University of Edinbugh: Edinburgh.
153. Hanley, K.J., et al., *Application of Taguchi methods to DEM calibration of bonded agglomerates.* Powder Technology, 2011. **210**(3): p. 230-240.
154. Montgomery, D.C., *Design and Analysis of Experiments*. 8th ed. 2012, Hoboken, NJ: John Wiley & Sons, Inc.
155. NIST/SEMATECH. *e-Handbook of Statistical Methods,* *http://www.itl.nist.gov/div898/handbook/*. 2016.
156. Derringer, G., *Simultaneous optimization of several response variables.* Journal of quality technology, 1980. **12**: p. 214-219.
157. Pizette, P., et al., *Compaction of aggregated ceramic powders: From contact laws to fracture and yield surfaces.* Powder Technology, 2010. **198**(2): p. 240-250.
158. Zuurman, K., K. Van Der Voort Maarschalk, and G.K. Bolhuis, *Effect of magnesium stearate on bonding and porosity expansion of tablets produced from materials with different consolidation properties.* International Journal of Pharmaceutics, 1999. **179**(1): p. 107-115.
159. Israelachivili, J.N., *Intermolecular and Surface Forces*. 3rd ed. 2011, Waltham, MA: Elsevier.
160. Procopio, A.T., *On the Compaction of Granular Media Using a Multi-Particle Finite Element Model*, in *Materials Science and Engineering*. 2006, Drexel University: Philadelphia. p. 172-172.
161. Onoda, G.Y. and E.G. Liniger, *Random loose packings of uniform spheres and the dilatancy onset.* Physical Review Letters, 1990. **64**(22): p. 2727-2730.
162. Krajcinovic, D. and M.A.G. Silva, *Statistical Aspects of the Continous Damage Theory.* International Journal of Solids and Structures, 1981. **18**(7): p. 551-562.
163. Lemaitre, J., *A Continuous Damage Mechanics Model for Ductile Fracture.* Journal of Engineering Materials and Technology, 1985. **107**(January 1985): p. 83-89.
164. Lubarda, V.A. and D. Krajcinovic, *Damage tensors and the crack density distribution.* International Journal of Solids and Structures, 1993. **30**(20): p. 2859-2877.
165. Krajcinovic, D., *Damage mechanics*. Vol. 41. 1996: Elsevier.
166. Voyiadjis, G. and P. Kattan, *A Comparative Study of Damage Variables in Continuum Damage Mechanics.* Internantional Journal of Damage Mechanics, 2008. **0**(1): p. 1-26.
167. Couples, G., I. Main, and P. Meredith, *Relationships between Damage and Localization: A Euroconference on Rock Mechanics and Rock Physics.* Newsletter Physical Properties of Earth Materials, 2000: p. 3-8.

Appendix A: The DPC Constitutive Model

The DPC model provides an inelastic hardening mechanism that accounts for plastic deformation during compaction and volume dilatancy when the material yields in shear. Central to this model is the yield surface shown in Figure A.1, which is divided into two principal segments: a shear failure surface F_s that describes the behavior of the powder under low hydrostatic pressure, and a cap surface F_c that describes hardening behavior and densification of the powder. In the p-q plane, the shear failure surface is represented simply as a straight line and is defined by

$$F_s = q - d - p\tan(\beta) = 0 \qquad (1),$$

where p is the hydrostatic stress, q is the von-Mises effective stress, β is the failure line angle, and d is the cohesion. The cap yield surface describing the densification of the powder is an ellipse given by

$$F_c = \sqrt{\left(p - p_a\right)^2 + \left(Rq\right)^2} - R\left(d + p_a \tan\beta\right) = 0 \quad (2),$$

where R is a measure of the eccentricity or shape of the ellipse, and p_a is the point along the p-axis that represents the intersection of the shear and cap surfaces and is termed the evolution parameter. As the material densifies the yield surface shown in Figure A.1 expands and the

evolution of this expanding yield surface is described by the hardening law p_b as a function of the volumetric plastic strain $\varepsilon_V^p = \ln(RD/RD_0)$, where p_b is the hydrostatic yield stress. The four material parameters d, β, R and p_b are considered to be functions of the out of die relative density.

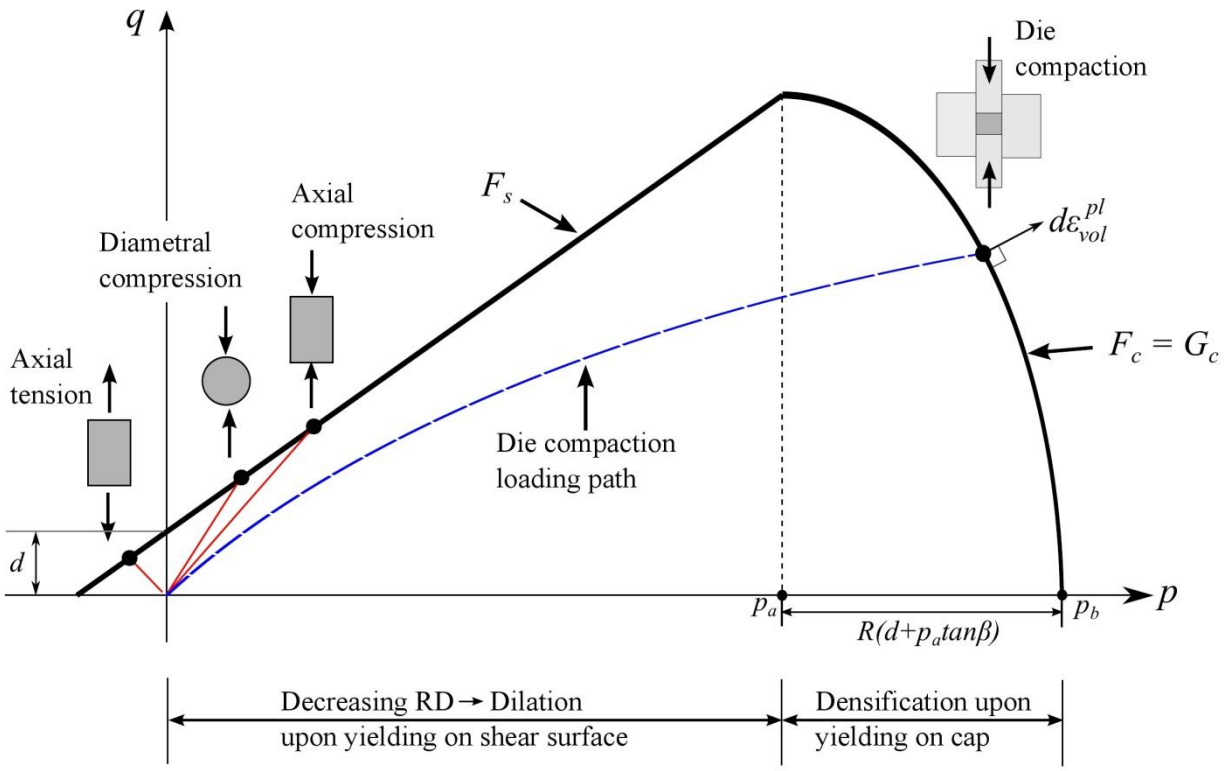

Figure A.1 Modified Drucker-Prager/Cap model: yield surface in p-q plane with experimental procedures for determining the shear failure surface F_S and the cap surface F_C.

Since the shear failure surface is defined by a straight line, two points on this line are all that is needed to obtain the cohesion d and internal friction angle β for a particular level of

relative density. These two points are obtained *via* diametral and axial compression strength tests of cylindrical compacts. The stress state in *p*-*q* space is given by $p = 2\sigma_T / 3$ and $q = \sqrt{13}\sigma_T$ for diametral compression. Similarly, the stress state in *p*-*q* space for axial compression is given by $p = \sigma_C / 3$ and $q = \sigma_C$. From diametral and axial compression strength tests, cohesion *d* and internal friction angle β as functions of relative density are obtained from the two points along the shear failure surface for any given level of achievable relative density. The cohesion and internal friction are defined in terms of diametral and axial compressive strength by

$$d = \frac{\sigma_C \sigma_T \left(\sqrt{13} - 2\right)}{\sigma_C - 2\sigma_T} \tag{5}$$

$$\beta = \tan^{-1}\left(\frac{3\left(\sigma_C - d\right)}{\sigma_C}\right) \tag{6}.$$

The parameters R and p_b used to define the cap surface are determined from a sequence of hydrostatic pressure and equivalent Mises stress measurements (die compaction loading path in Figure (A.1). For die compaction, the hydrostatic stress measure is given by $p = 1/3\left(\sigma_{zz} + 2\sigma_{rr}\right)$ and the equivalent Mises stress measure is given by $q = \left|\sigma_{zz} - \sigma_{rr}\right|$, where σ_{zz} and σ_{rr} are the axial and radial stresses required to produce a compact of out of die relative density, RD. Assuming a perfectly rigid die and low friction at the powder-tooling interfaces, these stress measurements, along with cohesion and friction angle, are used to define the hydrostatic yield stress p_b and cap eccentricity R as a function of the out of die relative density, RD by the following equations:

$$p_b = p_a + R[d + p_a \tan(\beta)] \qquad (10)$$

$$R = \sqrt{\frac{2}{3q}\left(p - p_a\right)} \qquad (11)$$

The parameter p_a representing the intersection of the shear and cap surfaces is given by

$$p_a = \frac{-3q - 4d\tan(\beta) + \sqrt{9q^2 + 24dq\tan(\beta) + 8(3pq + 2q^2)\tan^2(\beta)}}{4\tan^2(\beta)} \qquad (12).$$

Appendix B: Minitab Output for CCDs

Loading-unloading CCD Analysis

In the following output from the CCD analysis, the variables A, B, C, and D are equal to $k_1, \hat{k}_2/k_1, \theta$, and μ respectively.

Response Surface Regression: $\min\left\|U_p - U_p^*\right\|$ Axial Direction versus A, B, C, D

Analysis of Variance

Source	DF	Adj SS	Adj MS	F-Value	P-Value
Model	14	338.274	24.162	266.48	0.000
Linear	4	323.292	80.823	891.36	0.000
A	1	53.193	53.193	586.64	0.000
B	1	0.911	0.911	10.05	0.010
C	1	151.588	151.588	1671.80	0.000
D	1	117.600	117.600	1296.96	0.000
Square	4	9.910	2.477	27.32	0.000
A*A	1	0.001	0.001	0.01	0.935
B*B	1	0.011	0.011	0.13	0.729
C*C	1	3.983	3.983	43.92	0.000
D*D	1	0.083	0.083	0.92	0.360
2-Way Interaction	6	5.073	0.845	9.32	0.001
A*B	1	0.001	0.001	0.01	0.932
A*C	1	0.184	0.184	2.02	0.185
A*D	1	0.484	0.484	5.34	0.043
B*C	1	0.166	0.166	1.84	0.205
B*D	1	0.026	0.026	0.29	0.601
C*D	1	4.212	4.212	46.45	0.000
Error	10	0.907	0.091		
Total	24	339.181			

Model Summary

S	R-sq	R-sq(adj)	R-sq(pred)
0.301120	99.73%	99.36%	*

Coded Coefficients

Term	Effect	Coef	SE Coef	T-Value	P-Value	VIF
Constant		22.967	0.301	76.27	0.000	
A	2.9775	1.4887	0.0615	24.22	0.000	1.00
B	0.3897	0.1949	0.0615	3.17	0.010	1.00
C	-5.0264	-2.5132	0.0615	-40.89	0.000	1.00
D	4.4272	2.2136	0.0615	36.01	0.000	1.00
A*A	0.0150	0.0075	0.0896	0.08	0.935	2.21
B*B	-0.0638	-0.0319	0.0896	-0.36	0.729	2.21
C*C	1.1877	0.5938	0.0896	6.63	0.000	2.21
D*D	-0.1719	-0.0859	0.0896	-0.96	0.360	2.21
A*B	0.0131	0.0066	0.0753	0.09	0.932	1.00

A*C	-0.2142	-0.1071	0.0753	-1.42	0.185	1.00
A*D	0.3479	0.1739	0.0753	2.31	0.043	1.00
B*C	-0.2040	-0.1020	0.0753	-1.35	0.205	1.00
B*D	0.0813	0.0407	0.0753	0.54	0.601	1.00
C*D	-1.0261	-0.5131	0.0753	-6.82	0.000	1.00

Regression Equation in Uncoded Units

$\min|U_p-U_p^*|$ = 22.967 + 1.4887 A + 0.1949 B - 2.5132 C + 2.2136 D + 0.0075 A*A - 0.0319 B*B + 0.5938 C*C - 0.0859 D*D + 0.0066 A*B - 0.1071 A*C + 0.1739 A*D - 0.1020 B*C + 0.0407 B*D - 0.5131 C*D

Response Surface Regression: $\min\left\|U_E - U_E^*\right\|$ Axial Direction versus A, B, C, D

Analysis of Variance

Source	DF	Adj SS	Adj MS	F-Value	P-Value
Model	14	75.7785	5.4128	95.09	0.000
Linear	4	70.3405	17.5851	308.94	0.000
A	1	15.6614	15.6614	275.14	0.000
B	1	0.1693	0.1693	2.97	0.115
C	1	51.3837	51.3837	902.72	0.000
D	1	3.1262	3.1262	54.92	0.000
Square	4	4.1421	1.0355	18.19	0.000
A*A	1	0.0000	0.0000	0.00	0.993
B*B	1	0.0014	0.0014	0.03	0.877
C*C	1	1.8246	1.8246	32.05	0.000
D*D	1	0.0005	0.0005	0.01	0.924
2-Way Interaction	6	1.2959	0.2160	3.79	0.031
A*B	1	0.0021	0.0021	0.04	0.851
A*C	1	0.0392	0.0392	0.69	0.426
A*D	1	0.0079	0.0079	0.14	0.718
B*C	1	0.0435	0.0435	0.76	0.402
B*D	1	0.0298	0.0298	0.52	0.486
C*D	1	1.1734	1.1734	20.61	0.001
Error	10	0.5692	0.0569		
Total	24	76.3477			

Model Summary

S	R-sq	R-sq(adj)	R-sq(pred)
0.238581	99.25%	98.21%	*

Coded Coefficients

Term	Effect	Coef	SE Coef	T-Value	P-Value	VIF
Constant		1.265	0.239	5.30	0.000	
A	1.6156	0.8078	0.0487	16.59	0.000	1.00
B	0.1680	0.0840	0.0487	1.72	0.115	1.00
C	-2.9264	-1.4632	0.0487	-30.05	0.000	1.00
D	0.7218	0.3609	0.0487	7.41	0.000	1.00
A*A	-0.0013	-0.0006	0.0710	-0.01	0.993	2.21
B*B	-0.0225	-0.0113	0.0710	-0.16	0.877	2.21
C*C	0.8039	0.4019	0.0710	5.66	0.000	2.21
D*D	-0.0139	-0.0070	0.0710	-0.10	0.924	2.21
A*B	-0.0229	-0.0115	0.0596	-0.19	0.851	1.00

A*C	-0.0990	-0.0495	0.0596	-0.83	0.426	1.00
A*D	0.0444	0.0222	0.0596	0.37	0.718	1.00
B*C	-0.1043	-0.0522	0.0596	-0.87	0.402	1.00
B*D	0.0864	0.0432	0.0596	0.72	0.486	1.00
C*D	-0.5416	-0.2708	0.0596	-4.54	0.001	1.00

Regression Equation in Uncoded Units

$\min|U_E - U_E^*| = 1.265 + 0.8078\ A + 0.0840\ B - 1.4632\ C + 0.3609\ D - 0.0006\ A*A - 0.0113\ B*B + 0.4019\ C*C - 0.0070\ D*D - 0.0115\ A*B - 0.0495\ A*C + 0.0222\ A*D - 0.0522\ B*C + 0.0432\ B*D - 0.2708\ C*D$

Response Surface Regression: $\min\left\|U_p - U_p^*\right\|$ Radial Direction versus A, B, C, D

Analysis of Variance

Source	DF	Adj SS	Adj MS	F-Value	P-Value
Model	14	22.4463	1.6033	44.42	0.000
Linear	4	19.6626	4.9157	136.18	0.000
A	1	0.2425	0.2425	6.72	0.027
B	1	0.7785	0.7785	21.57	0.001
C	1	13.4052	13.4052	371.36	0.000
D	1	5.2364	5.2364	145.06	0.000
Square	4	1.9430	0.4858	13.46	0.000
A*A	1	0.0005	0.0005	0.01	0.909
B*B	1	0.0039	0.0039	0.11	0.749
C*C	1	0.9295	0.9295	25.75	0.000
D*D	1	0.0045	0.0045	0.13	0.730
2-Way Interaction	6	0.8407	0.1401	3.88	0.029
A*B	1	0.0051	0.0051	0.14	0.715
A*C	1	0.0053	0.0053	0.15	0.709
A*D	1	0.0064	0.0064	0.18	0.682
B*C	1	0.0021	0.0021	0.06	0.814
B*D	1	0.0049	0.0049	0.14	0.719
C*D	1	0.8168	0.8168	22.63	0.001
Error	10	0.3610	0.0361		
Total	24	22.8073			

Model Summary

S	R-sq	R-sq(adj)	R-sq(pred)
0.189993	98.42%	96.20%	*

Coded Coefficients

Term	Effect	Coef	SE Coef	T-Value	P-Value	VIF
Constant		-0.039	0.190	-0.21	0.840	
A	0.2011	0.1005	0.0388	2.59	0.027	1.00
B	-0.3602	-0.1801	0.0388	-4.64	0.001	1.00
C	-1.4947	-0.7474	0.0388	-19.27	0.000	1.00
D	0.9342	0.4671	0.0388	12.04	0.000	1.00
A*A	-0.0133	-0.0066	0.0565	-0.12	0.909	2.21
B*B	0.0373	0.0186	0.0565	0.33	0.749	2.21
C*C	0.5738	0.2869	0.0565	5.07	0.000	2.21
D*D	0.0401	0.0200	0.0565	0.35	0.730	2.21
A*B	-0.0357	-0.0179	0.0475	-0.38	0.715	1.00

A*C	-0.0365	-0.0182	0.0475	-0.38	0.709	1.00
A*D	0.0400	0.0200	0.0475	0.42	0.682	1.00
B*C	0.0229	0.0115	0.0475	0.24	0.814	1.00
B*D	-0.0352	-0.0176	0.0475	-0.37	0.719	1.00
C*D	-0.4519	-0.2259	0.0475	-4.76	0.001	1.00

Regression Equation in Uncoded Units

$\min|U_p-U_p^*|$ = -0.039 + 0.1005 A - 0.1801 B - 0.7474 C + 0.4671 D - 0.0066 A*A + 0.0186 B*B + 0.2869 C*C + 0.0200 D*D - 0.0179 A*B - 0.0182 A*C + 0.0200 A*D + 0.0115 B*C - 0.0176 B*D - 0.2259 C*D

Response Surface Regression: $\min\left\|U_E - U_E^*\right\|$ Radial Direction versus A, B, C, D

Analysis of Variance

Source	DF	Adj SS	Adj MS	F-Value	P-Value
Model	14	30.6069	2.1862	23.29	0.000
Linear	4	25.3841	6.3460	67.62	0.000
A	1	0.2126	0.2126	2.26	0.163
B	1	1.1348	1.1348	12.09	0.006
C	1	20.3469	20.3469	216.80	0.000
D	1	3.6898	3.6898	39.31	0.000
Square	4	4.0541	1.0135	10.80	0.001
A*A	1	0.0019	0.0019	0.02	0.888
B*B	1	0.0026	0.0026	0.03	0.870
C*C	1	1.8537	1.8537	19.75	0.001
D*D	1	0.0007	0.0007	0.01	0.934
2-Way Interaction	6	1.1687	0.1948	2.08	0.147
A*B	1	0.0030	0.0030	0.03	0.861
A*C	1	0.0044	0.0044	0.05	0.833
A*D	1	0.0001	0.0001	0.00	0.982
B*C	1	0.0351	0.0351	0.37	0.554
B*D	1	0.0137	0.0137	0.15	0.710
C*D	1	1.1124	1.1124	11.85	0.006
Error	10	0.9385	0.0939		
Total	24	31.5454			

Model Summary

S	R-sq	R-sq(adj)	R-sq(pred)
0.306352	97.02%	92.86%	*

Coded Coefficients

Term	Effect	Coef	SE Coef	T-Value	P-Value	VIF
Constant		-0.001	0.306	-0.00	0.998	
A	0.1882	0.0941	0.0625	1.50	0.163	1.00
B	-0.4349	-0.2175	0.0625	-3.48	0.006	1.00
C	-1.8415	-0.9208	0.0625	-14.72	0.000	1.00
D	0.7842	0.3921	0.0625	6.27	0.000	1.00
A*A	-0.0262	-0.0131	0.0912	-0.14	0.888	2.21
B*B	0.0306	0.0153	0.0912	0.17	0.870	2.21
C*C	0.8102	0.4051	0.0912	4.44	0.001	2.21
D*D	0.0156	0.0078	0.0912	0.09	0.934	2.21
A*B	-0.0275	-0.0137	0.0766	-0.18	0.861	1.00

A*C	-0.0332	-0.0166	0.0766	-0.22	0.833	1.00
A*D	-0.0036	-0.0018	0.0766	-0.02	0.982	1.00
B*C	0.0937	0.0468	0.0766	0.61	0.554	1.00
B*D	-0.0585	-0.0293	0.0766	-0.38	0.710	1.00
C*D	-0.5274	-0.2637	0.0766	-3.44	0.006	1.00

Regression Equation in Uncoded Units

$\min|U_E-U_E^*|$ = -0.001 + 0.0941 A - 0.2175 B - 0.9208 C + 0.3921 D - 0.0131 A*A + 0.0153 B*B + 0.4051 C*C + 0.0078 D*D - 0.0137 A*B - 0.0166 A*C - 0.0018 A*D + 0.0468 B*C - 0.0293 B*D - 0.2637 C*D

Tensile Strength CCD Analysis

In the following analysis, the variables A and B represent λ and C respectively.

Response Surface Regression: $\min\left\|\sigma_T-\sigma_T^*\right\|$ (75% RD) versus A, B

Analysis of Variance

Source	DF	Adj SS	Adj MS	F-Value	P-Value
Model	5	1.26760	0.253520	283.89	0.000
Linear	2	1.23185	0.615925	689.71	0.000
A	1	0.93826	0.938262	1050.66	0.000
B	1	0.29359	0.293588	328.76	0.000
Square	2	0.00024	0.000122	0.14	0.877
A*A	1	0.00006	0.000063	0.07	0.808
B*B	1	0.00024	0.000238	0.27	0.641
2-Way Interaction	1	0.03551	0.035505	39.76	0.008
A*B	1	0.03551	0.035505	39.76	0.008
Error	3	0.00268	0.000893		
Total	8	1.27028			

Model Summary

S	R-sq	R-sq(adj)	R-sq(pred)
0.0298834	99.79%	99.44%	*

Coded Coefficients

Term	Effect	Coef	SE Coef	T-Value	P-Value	VIF
Constant		0.5919	0.0299	19.81	0.000	
A	0.6849	0.3425	0.0106	32.41	0.000	1.00
B	-0.3831	-0.1916	0.0106	-18.13	0.000	1.00
A*A	-0.0093	-0.0046	0.0175	-0.26	0.808	1.68
B*B	-0.0181	-0.0090	0.0175	-0.52	0.641	1.68
A*B	-0.1884	-0.0942	0.0149	-6.31	0.008	1.00

Regression Equation in Uncoded Units

$\min|\sigma_T - \sigma_T^*| = 0.0882 + 0.3425\ A - 0.1916\ B - 0.0046\ A*A - 0.0090\ B*B - 0.0942\ A*B$

Response Surface Regression: $\min\left\|\sigma_T - \sigma_T^*\right\|$ (85% RD) versus A, B

Analysis of Variance

Source	DF	Adj SS	Adj MS	F-Value	P-Value
Model	5	7.32753	1.46551	159.96	0.001
Linear	2	7.10871	3.55435	387.95	0.000
A	1	4.56974	4.56974	498.78	0.000
B	1	2.53896	2.53896	277.12	0.000
Square	2	0.01409	0.00704	0.77	0.538
A*A	1	0.01402	0.01402	1.53	0.304
B*B	1	0.00667	0.00667	0.73	0.456
2-Way Interaction	1	0.20474	0.20474	22.35	0.018
A*B	1	0.20474	0.20474	22.35	0.018
Error	3	0.02749	0.00916		
Total	8	7.35502			

Model Summary

S	R-sq	R-sq(adj)	R-sq(pred)
0.0957174	99.63%	99.00%	*

Coded Coefficients

Term	Effect	Coef	SE Coef	T-Value	P-Value	VIF
Constant		1.6175	0.0957	16.90	0.000	
A	1.5116	0.7558	0.0338	22.33	0.000	1.00
B	-1.1267	-0.5634	0.0338	-16.65	0.000	1.00
A*A	-0.1388	-0.0694	0.0561	-1.24	0.304	1.68
B*B	-0.0958	-0.0479	0.0561	-0.85	0.456	1.68
A*B	-0.4525	-0.2262	0.0479	-4.73	0.018	1.00

Regression Equation in Uncoded Units

$\min|\sigma_T - \sigma_T^*| = 0.5142 + 0.7558\ A - 0.5634\ B - 0.0694\ A*A - 0.0479\ B*B - 0.2262\ A*B$

Response Surface Regression: $\min\left\|\sigma_T - \sigma_T^*\right\|$ (98% RD) versus A, B

Analysis of Variance

Source	DF	Adj SS	Adj MS	F-Value	P-Value
Model	5	30.2241	6.0448	169.61	0.001
Linear	2	29.3173	14.6586	411.31	0.000
A	1	20.6957	20.6957	580.70	0.000
B	1	8.6216	8.6216	241.91	0.001
Square	2	0.0454	0.0227	0.64	0.588

A*A	1	0.0001	0.0001	0.00	0.969
B*B	1	0.0287	0.0287	0.80	0.436
2-Way Interaction	1	0.8614	0.8614	24.17	0.016
A*B	1	0.8614	0.8614	24.17	0.016
Error	3	0.1069	0.0356		
Total	8	30.3310			

Model Summary

S	R-sq	R-sq(adj)	R-sq(pred)
0.188784	99.65%	99.06%	*

Coded Coefficients

Term	Effect	Coef	SE Coef	T-Value	P-Value	VIF
Constant		3.223	0.189	17.07	0.000	
A	3.2168	1.6084	0.0667	24.10	0.000	1.00
B	-2.0762	-1.0381	0.0667	-15.55	0.001	1.00
A*A	-0.009	-0.005	0.111	-0.04	0.969	1.68
B*B	-0.199	-0.099	0.111	-0.90	0.436	1.68
A*B	-0.9281	-0.4641	0.0944	-4.92	0.016	1.00

Regression Equation in Uncoded Units

$\min|\sigma_T - \sigma_T^*| = 0.8281 + 1.6084\ A - 1.0381\ B - 0.005\ A*A - 0.099\ B*B - 0.4641\ A*B$

Vita

Sean Garner

Education
PhD, Materials Science & Engineering, Drexel University, Philadelphia, PA, USA
October 2015

BS, Materials Science & Engineering, Drexel University, Philadelphia, PA, USA
June 2010

Experience
Senior Scientist I, Abbvie Inc., 2016-present
Research/Teaching Assistant, Drexel University, 2010-2015
Valero Energy Corporation, Paulsboro Refinery, 2008

Honors/Awards
The Department of Education Graduate Assistance in Areas of National Need Drexel Research and Education in Advanced Materials Fellowship (GAANN-DREAM)
A.J. Drexel Dean's Transfer Scholarship for Academic Excellence
Joseph and Shirley Carleone Endowed Fellowship
Best Poster Award—Compaction Simulator Forum, Philadelphia, PA—2014
Best Poster Award—International Fine Particle Research Institute (IFPRI) Annual General Meeting—Edinburgh, Scotland—2014

Publications

Garner, S., et al., *Mechanisms of crack formation in die compacted powders during unloading and ejection: An experimental and modeling comparison between standard straight and tapered dies.* Powder Technology, 2014. **264**: p. 114-127.

Garner, S., J. Strong, and A. Zavaliangos, *The extrapolation of the Drucker–Prager/Cap material parameters to low and high relative densities.* Powder Technology, 2015. **283**: p. 210-226.